RADIATION DAMAGE STUDIED BY PULSED ION BEAMS

A Dissertation

by

JOSEPH BENJAMIN WALLACE

Submitted to the Office of Graduate and Professional Studies of
Texas A&M University
in partial fulfillment of the requirements for the degree of

DOCTOR OF PHILOSOPHY

Chair of Committee,	Lin Shao
Committee Members,	Sean McDeavitt
	Haiyan Wang
	Xinghang Zhang
Head of Department,	Yassin Hassan

August 2017

Major Subject: Nuclear Engineering

Copyright 2017 Joseph Benjamin Wallace

ABSTRACT

Energetic particles propagating through crystalline materials can transfer their kinetic energy to target atoms in the form of knock-on collisions. These target atoms can then cause subsequent collisions with other target atoms, ultimately leading to the formation of a ballistic cascade of point defects. The formation and thermalization of ion cascades, which occurs at time scales up to ∼ps, is thought to be reasonably well understood. However, the understanding of defect interaction after cascade thermalization, known as dynamic annealing, is quite limited, despite nearly five decades of research. Dynamic annealing often plays the dominant role in the formation of stable radiation disorder in crystalline solids. However, current models of radiation damage are essentially empirical fits to experimental data, incapable of capturing the full physics of the problem. Understanding dynamic annealing is crucial to describing radiation damage in crystalline solids of interest to electronics and nuclear materials applications. The purpose of this dissertation is to improve the understanding of dynamic annealing and radiation damage in crystalline materials.

To achieve this, a novel pulsed ion beam method was developed. A major difficulty in previous attempts to describe dynamic annealing was separating the spatial and temporal variables, which are convoluted in dose rate experiments. Such experiments often required overarching assumptions to isolate the defect lifetime and diffusion length. In contrast, the pulse beam method allows separation of the temporal and spatial aspects of dynamic annealing at the experimental level.

Using the pulsed beam method, a defect lifetime of $\sim 0.1 - 100$ ms and a characteristic diffusion length of $\sim 5 - 50$ nm are measured in Si, Ge, and SiC. In addition, the dynamic annealing rate shows an Arrhenius dependence in Si and Ge

with activation energies in the range from $\sim 0.1 - 1.3$ eV. Rate theory modeling, bench-marked against this data, suggests a crucial role of both vacancy and interstitial diffusion, with the dynamic annealing rate limited by the migration and interaction of vacancies. The defect lifetime, diffusion length, and dominant defect interaction mechanisms are sensitively affected by the bombarding ion mass, energy, target temperature, and pre-existing lattice defects.

These studies represent a significant advancement in the understanding of radiation defect dynamics in materials. Moreover, this dissertation lays the groundwork for future studies of radiation defect dynamics in other technologically relevant materials.

DEDICATION

To my family and friends, thank you for always supporting me.

ACKNOWLEDGEMENTS

The work presented in this manuscript was done under Prof. Lin Shao (Texas A&M, Department of Nuclear Engineering) and Dr. Sergei Kucheyev (Lawrence Livermore National Laboratory). I would like to express my gratitude to Dr. Lin Shao for taking me on as an undergraduate research assistant and later as a graduate research assistant. His guidance was essential to my growth and development as a scientist. I would also like to thank my technical supervisor, Dr. Sergei Kucheyev, for introducing me to the topic of pulsed ion beams, which has been an amazing experience. Sergei's guidance in planning and running experiments, writing manuscripts, answering reviewer questions has been absolutely essential to both the success of this project and to my overall growth into a mature scientist. I would also like to sincerely thank Dr. Leonardus Bimo Bayu Aji for innumerable hours of fruitful discussions on pulsed ion beam and for help running and planning experiments. Finally, I would also like to thank my group members, colleagues, and collaborators, Dr. Di Chen, Mark Hollander, Dr. Chao Chen Wei, Dr. Eda Aydogan, Michael Justinn General, Dr. Michael Bagge-Hansen, and Dr. Supakit Charnvanichborikarn for their help throughout this dissertation.

CONTRIBUTORS AND FUNDING SOURCES

Contributors

This work was supported by a thesis committee consisting of Professors Lin Shao and Sean McDeavitt of the Department of Nuclear Engineering, Professor Haiyan Wang of the Department of Electrical Engineering, and Professor Xinghang Zhang of the Department of Mechanical Engineering.

The work in Section 6 was conducted in part by Dr. Leonardus Bimo Bayu Aji of Lawrence Livermore National Laboratory.

All other work conducted for this dissertation was completed by the student independently.

Funding Sources

This work was funded by the Nuclear Energy Enabling Technology (NEET) Program of the U.S. DOE, Office of Nuclear Energy and performed under the auspices of the U.S. DOE under Contract DE-AC52-07NA27344. This graduate study was also supported by the Lawrence Scholar Program at the Lawrence Livermore National Laboratory.

NOMENCLATURE

DA	Dynamic Annealing
DLTS	Deep Level Transient Spectroscopy
DPA	Displacement Per Atom
eV	Electron Volt
FZ	Float Zone
keV	Kilo Electron Volt
L_d	Diffusion Length
LLNL	Lawrence Livermore National Laboratory
MeV	Mega Electron Volt
MD	Molecular Dynamics
NEC	National Electrostatics Corporation
nm	Nanometer
RBS/C	Rutherford Backscattering and Channeling Spectrometry
RT	Room Temperature
Si	Silicon
SiC	Silicon Carbide
Si_3N_4	Silicon Nitride
SRIM	Stopping and Range of Ions in Matter
Tau (τ)	Defect Lifetime
TEM	Transmission Electron Microscopy
TRIM	Transport and Range of Ions in Matter

TABLE OF CONTENTS

Page

ABSTRACT . . . ii

DEDICATION . . . iv

ACKNOWLEDGEMENTS . . . v

CONTRIBUTORS AND FUNDING SOURCES . . . vi

NOMENCLATURE . . . vii

TABLE OF CONTENTS . . . viii

LIST OF FIGURES . . . xi

LIST OF TABLES . . . xx

1. INTRODUCTION . . . 1

1.1 Motivation . . . 1
1.2 Pulsed ion beam technique . . . 3
1.3 Dissertation structure . . . 4

2. METHODOLOGY . . . 5

2.1 Pulsed ion beam method . . . 5
2.1.1 Pulsing parameters . . . 5
2.1.2 Diffusion length . . . 5
2.1.3 Characteristic defect lifetime . . . 6
2.2 Samples . . . 6
2.2.1 Silicon . . . 7
2.2.2 Silicon carbide . . . 7
2.2.3 Germanium . . . 7
2.3 Characterization . . . 7
2.3.1 Rutherford backscattering spectroscopy . . . 7
2.3.2 Nuclear reaction analysis . . . 8
2.3.3 Transmission electron microscopy . . . 8
2.4 Facility . . . 8

3. RADIATION DEFECT DYNAMICS IN SI AT ROOM TEMPERATURE . . . 10

3.1 Introduction . . . 10
3.2 Experiment . . . 11
3.2.1 Targets . . . 11
3.2.2 Ion bombardment and ion channeling analysis . . . 12
3.3 Results and discussion . . . 14
3.3.1 Damage buildup . . . 14
3.3.2 Dynamic annealing time constant . . . 17
3.3.3 Defect diffusion length . . . 23
3.3.3.1 Pulsed ion beam measurement of L_d . . . 23
3.3.3.2 Variable-beam-tilt measurement of L_d . . . 27
3.3.4 Choice of pulsing parameters . . . 30
3.3.4.1 Choice of pulsing parameters in τ measurements . . . 30
3.3.4.2 Choice of pulsing parameters in L_d measurements . . . 33
3.4 Conclusions . . . 35

4. THE ROLE OF FRENKEL DEFECT DIFFUSION IN DYNAMIC ANNEALING IN ION-IRRADIATED SI . . . 37

4.1 Experimental . . . 38
4.2 Results and discussion . . . 40
4.3 Modeling . . . 47
4.4 Conclusion . . . 49

5. CASCADE DENSITY EFFECTS ON DEFECT DYNAMICS . . . 51

5.1 Defect diffusion in pulsed ion irradiated solids – a fractal approach . . . 51
5.1.1 Introduction . . . 51
5.1.2 Experimental . . . 53
5.1.3 Modeling . . . 54
5.1.4 Results and discussion . . . 55
5.1.5 Conclusion . . . 64
5.2 Influence of cascade density on radiation defect dynamics in Si studied by pulsed ion beam . . . 65
5.2.1 Introduction . . . 65
5.2.2 Experimental . . . 67
5.2.3 Results and discussion . . . 68
5.2.4 Conclusion . . . 77
5.3 The effect of super-cascade density on dynamic annealing in Si . . . 78
5.3.1 Introduction . . . 78
5.3.2 Experimental . . . 80

5.3.3 Results and discussion 81
5.3.4 Conclusion 87

6. RADIATION DEFECT DYNAMICS IN SIC 90

6.1 Time constant of defect relaxation in ion-irradiated 3C-SiC 91
6.1.1 Experimental 92
6.1.2 Results and discussion 94
6.1.3 Conclusion 100
6.2 Temperature dependence of radiation defect dynamics in 4$H-$SiC . . 100
6.2.1 Experimental 101
6.2.2 Results and discussion 102
6.2.3 Conclusion 111

7. DYNAMIC ANNEALING IN GE STUDIED BY PULSED ION BEAMS . 112

7.1 Introduction 112
7.2 Experimental 113
7.3 Results and discussion 114
7.3.1 Diffusion length 114
7.3.2 Time constant 116
7.3.3 Activation energy 121
7.4 Conclusion 122

8. INFLUENCE OF MICROSTRUCTURE ON RADIATION DEFECT DYNAMICS IN SI 123

8.1 Experimental 125
8.2 Results and discussion 126
8.3 Conclusion 135

9. SUMMARY 136

REFERENCES 139

LIST OF FIGURES

FIGURE Page

2.1 Schematic of the pulsed ion beam arrangement showing the ion beam passing through the set of electrostatic beam steering plates and the beam defining aperture into the final chamber where ions bombard the sample. The inset is a schematic of the time dependence of the instantaneous dose rate for pulsed beam irradiation, defining t_{on}, t_{off}, and F_{on}. 6

2.2 Schematic of the 4 MV ion accelerator (National Electrostatics Corporation, model 4UH) at Lawrence Livermore National Laboratory showing both the analysis and implantation beam lines. 9

3.1 (Color online) (a) Normalized depth profiles of the concentration of lattice vacancies ballistically generated in Si by irradiation with 500 keV ^{20}Ne, ^{40}Ar, ^{84}Kr, or ^{129}Xe ions. Results of TRIM-code simulations. Positions of the vacancy distribution maxima (R_{pd}) are indicated by vertical dashed lines (at 795, 445, 210, and 150 nm). (b) Selected depth profiles of relative disorder for FZ-Si irradiated with Ne, Ar, Kr, and Xe ions to doses of 8, 2, 0.69, and 0.35×10^{14} cm^{-2} (or 0.77, 0.43, 0.37, and 0.30 DPA at R_{pd}), respectively. The legend in (a), relating symbols to ion masses, also applies to panel (b). Selected depth profiles of relative disorder in FZ-Si bombarded with a pulsed Ne ion beam (c) with different values of t_{off} (indicated in the legend in ms) and $t_{\mathrm{on}} = 1$ ms and (d) with different values of t_{on} (indicated in the legend in ms) and $t_{\mathrm{off}} = 100$ ms and all the other parameters fixed (a total dose of $\Phi = 8 \times 10^{14}$ cm^{-2} and $F_{\mathrm{on}} = 2.9 \times 10^{13}$ cm^{-2}s^{-1}). 15

3.2 (Color online) Dose dependencies of relative disorder at the maximum of the bulk defect peak for FZ-Si bombarded at room temperature with 500 keV Ne, Ar, Kr, or Xe ions with a constant displacement generation rate of $\sim 2.5 \times 10^{-2}$ DPA/s at R_{pd}. 16

3.3 (Color online) Dependencies of relative disorder at the maximum of the bulk defect peak in FZ- and CZ-Si bombarded at room temperature with a pulsed beam of 500 keV ^{40}Ar ions with $t_{on} = 1$ ms and different F_{on} and Φ (given in the legend in units of cm^{-2} s^{-1} and cm^{-2}, respectively) on the duration of the passive part of the cycle, t_{off}, and all the other parameters fixed. Dashed lines are fitting curves of the second order rate equation (Eq. 3.1), with τ values shown in the legend in ms. 18

3.4 (Color online) Dependencies of relative disorder at the maximum of the bulk defect peak in FZ-Si bombarded at room temperature with pulsed beams of 500 keV ^{20}Ne, ^{40}Ar, ^{84}Kr, or ^{129}Xe ions on the duration of the passive part of the cycle, t_{off}, and all the other parameters fixed, as listed in Table 3.1. Solid lines are fitting curves with the second order rate equation (Eq. 3.1). 20

3.5 (Color online) Dependence of [(a), left axis] the DA time constant (τ), [(a), right axis] the DA efficiency (ξ), and (b) defect diffusion length (L_d) on ion mass for FZ-Si bombarded at room temperature with pulsed beams of 500 keV Ne, Ar, Kr and Xe ions with $t_{on} = 1$ ms and F_{on} values of 2.9, 1.2, 0.5, and 0.3×10^{13} cm^{-2} s^{-1}, respectively. 22

3.6 (Color online) Dependence of relative disorder at the maximum of the bulk defect peak in FZ-Si bombarded at room temperature with a pulsed beam of 500 keV ^{40}Ar ions with $t_{off} = 100$ ms and different F_{on} (as indicated in the legend) to a total dose of 2.2×10^{14} cm^{-2} on the duration of the active part of the cycle, t_{on}. 25

3.7 (Color online) Dependence of relative disorder at the maximum of the bulk defect peak in FZ-Si bombarded at room temperature with pulsed beams of 500 keV ^{20}Ne, ^{40}Ar, or ^{129}Xe ions with $t_{off} = 100$ ms (and different F_{on} of Ar ions) on the half of the average lateral distance between collision cascades in each pulse ($L_{overlap}$). Dashed lines are to guide the reader's eye. Arrows mark L_d values. 26

3.8 (Color online) (a) Normalized depth profiles of lattice vacancies ballistically generated in Si by irradiation with 500 keV Xe ions with different incident beam angles relative to the sample surface normal. Positions of the maxima, R_{pd}, of such profiles are indicated by vertical dash lines (at 30, 60, and 152 nm). (b) and (c) Depth profiles of relative disorder for Si irradiated at room temperature at various angles to ion doses of 0.15 and 0.33 DPA, respectively. 28

3.9 (Color online) Ion dose dependencies of (a) the effective thickness of surface amorphous layers, (b) the bulk damage peak maximum, and (c) the damage production efficiency for Si bombarded at room temperature with 500 keV Xe ions for three beam tilt angles. 29

3.10 (Color online) Schematic of time dependencies of (a) the instantaneous dose rate for pulsed beam irradiation and (b) – (d) the concentration of mobile defects at a given depth in a region of radius L_d for a constant t_{on} and different F_{on} or L_d values resulting in $\frac{t_{on}}{t_{on}^{L_d}}$ of 0.5, 1.0, and 2.0, respectively. 32

3.11 (Color online) (a) Dependence of the DA time constant (τ) on t_{on} for FZ-Si bombarded at room temperature with pulsed beams of 500 keV Ar ions with $t_{off} = 100$ ms and $F_{on} = 1.6 \times 10^{13}$ cm^{-2} s^{-1}. (b) The fraction of the sample area that has received 0, 1, 2, and 3 ion impacts for the total dose from two interacting pulses each of length t_{on}, with an ion impact area of $4L_d^2$ and $L_d = 28$ nm for Ar. 34

4.1 (Color online) Selected depth profiles of relative disorder in Si bombarded with a pulsed beam of 500 keV Ar ions with $F_{on} = 1.9 \times 10^{13}$ cm^{-2} s^{-1}, $t_{on} = 1$ ms, and different t_{off} values given in legends at temperatures and doses of (a) 40 °C and 2.7×10^{14} cm^{-2} and (b) 80 ° C and 5.0×10^{14} cm^{-2}. For clarity, only every 10th experimental point is depicted. The inset in (a) is a schematic of the time dependence of the instantaneous dose rate for pulsed beam irradiation, defining t_{on}, t_{off}, and F_{on}. 41

4.2 (Color online) Average relative bulk disorder in Si bombarded at different temperatures (given in legends in units of °C) with a pulsed beam of 500 keV Ar ions with $F_{on} = 1.9 \times 10^{13}$ cm^{-2} s^{-1} and $t_{on} = 1$ ms as a function of the passive portion of the beam duty cycle (t_{off}). Results of fitting the data with the first and second order decay equations are shown by solid and dashed lines, respectively. Results are separated into panels for clarity. 42

4.3 (Color online) Temperature dependencies of the effective time constant of DA (τ, the left axis) and the DA efficiency (ξ, the right axis) for fitting with the first (circles) and second (triangles) order decay equations. Solid symbols represent the best fit to the data. 44

4.4 (Color online) Arrhenius plot of the DA rate. Solid symbols are results of the best fit to experimental $n(t_{off})$ dependencies, which is the second order decay below 60 °C and the first order decay above 60 °C. Straight lines show results of linear fitting, revealing activation energies of 420 meV and 73 meV above and below 60 °C, respectively. Results of rate theory modeling, described in the text, are also shown. 45

5.1 (Color online) (a) Selected depth profiles (measured by ion channeling) of the relative disorder in the Si sublattice of SiC bombarded with 500 keV Ne, Ar, Kr, and Xe ions at 100 °C. (b) Normalized TRIM code predicted profiles of the concentration of vacancies and (c) implanted atoms for 500 keV Ne, Ar, Kr, and Xe ion irradiation of SiC. (d) Cascade density as a function of depth from TRIM simulated ion cascades in SiC evaluated with $R_c = 10$ nm. The inset in (a) shows the time dependence of the instantaneous flux for pulsed beam irradiation, defining F_{on}, t_{on}, and t_{off}. 57

5.2 (Color online) Averaged number of vacancies within R_c of a vacancy for TRIM simulated 500 keV Ne, Ar, Kr, and Xe ion cascades in SiC at the depth of the maximum nuclear energy loss (R_{pd}). Solid lines are linear fits used to determine fractal dimension and structure factor. 58

5.3 (Color online) Cascade density (a), fractal dimension (left axis (b)), and fractal structure factor $k_\circ$ (right axis, (b)) as a function of ion mass for TRIM simulated 500 keV ion cascades in SiC. Cascade density and fractal parameters were evaluated at the depth of the maximum nuclear energy loss (R_{pd}) and $R_c = 10$ nm. Dashed lines are to guide the eye. 60

5.4 (Color online) Dependence of relative disorder at the maximum of the bulk defect peak in (a) SiC bombarded at 100 °C and (b) Si bombarded at RT with pulsed beams of 500 keV Ne, Ar, Kr, and Xe ions on the dose per pulse. Solid lines depict fitting to the fractal diffusion length model derived herein. 62

5.5 (Color online) Dependence of fractal defect diffusion length ($L_d^{fractal}$, solid symbols) and previously reported diffusion length [46] (L_d, open triangle symbols) on ion mass for bombardment of SiC at 100 °C and Si at RT with a pulsed beam of 500 keV Ne, Ar, Kr, and Xe ions. . . 63

5.6 (Color online) Temperature dependence of the effective defect diffusion length (L_d) in 3*C*-SiC bombarded with 500 keV Ar ions. 64

5.7 (Color online) Selected depth profiles of relative disorder in Si bombarded with a pulsed beam of 500 keV Ar and Xe ions with $F_{on} = 1.9 \times 10^{13}$ and 0.5×10^{13} cm^{-2} s^{-1} respectively, $t_{on} = 1$ ms, and different t_{off} values given in legends at temperatures of (a) 100 °C and (b) 140 °C. For clarity, only every 10th experimental point is depicted. The inset in (b) is a schematic of the time dependence of the instantaneous dose rate for pulsed beam irradiation, defining t_{on}, t_{off}, and F_{on}. 70

5.8 (Color online) Relative bulk disorder in Si bombarded at different temperatures (given in the legend in units of °C) with a pulsed beam of 500 keV (a) Xe, (b) Kr, (c) Ar and, (d) Ne ions with $F_{on} \approx 0.45 \times 10^{13}$, 0.8×10^{13}, 1.9×10^{13}, and 2.7×10^{13} cm^{-2} s^{-1}, respectively, and $t_{on} = 1$ ms as a function of the passive portion of the beam duty cycle (t_{off}). Solid lines show the results of fitting the data with the first order decay equations. 71

5.9 (Color online) Temperature dependencies of (a) the effective time constant of DA (τ) and (b) the DA efficiency (ξ) for fitting of the bulk relative disorder with the first order decay equations in Si bombarded with a pulsed ion beam 500 keV Ne, Ar, Kr, and Xe ions. 73

5.10 (Color online) Arrhenius plot of the DA rate for Si bombarded with a pulsed ion beam 500 keV Ne, Ar, Kr, and Xe ions. Straight lines show results of linear fitting, revealing activation energies of ~ 0.4 eV and ~ 0.1 eV for Ne, Ar, and Kr and ~ 0.8 and ~ 0.1 eV for Xe at low and high T, respectively. The inset shows the critical temperature (T_c) of dynamic annealing at which E_a changes for each ion as a function of cascade density [82] (ρ) evaluated at $R_c = 20$ nm. For Kr, T_c in the inset is shown at depths between ~ 150 and 400 nm (open symbols) with ρ corresponding to the cascade density at each depth. 74

5.11 (Color online) Cascade density [82] as a function of depth from TRIM simulated Kr and Xe ion cascades in Si evaluated with $R_c = 20$ nm (left axis) and the activation energy at high T (right axis) as a function of depth in Kr and Xe. The dotted vertical line shows the depth at which the cascade density in Xe drops below the peak cascade density in Kr. Dashed lines over E_a values are to guide the eye. 76

5.12 (Color online) Selected depth profiles of relative disorder in Si bombarded at 100 °C with a pulsed beam of 500 keV Ar ions with $F_{on} = 1.8 \times 10^{13}$, fluence of 9.0×10^{14} cm^{-2}, and different t_{off} values given in legends at $t_{on} = 0.5$ (a) and 5 (b) ms. For clarity, only every 10th experimental point is depicted. The inset in (a) is a schematic of the time dependence of the instantaneous dose rate for pulsed beam irradiation, defining t_{on}, t_{off}, and F_{on}. 82

5.13 (Color online) Relative bulk disorder in Si bombarded at 100 °C with a pulsed beam of 500 keV Ar ions with $F_{on} = 1.8 \times 10^{13}$ cm^{-2} s^{-1} and t_{on} given in the legend in units of ms as a function of the passive portion of the beam duty cycle (t_{off}). Results of fitting the data with the first order decay equations are shown by solid lines. 83

5.14 (Color online) t_{on} dependencies of the effective time constant of DA (τ_{eff}) for first order fitting of Si bombarded with 500 keV Ne, Ar, and Xe at temperatures given in the legend. 85

5.15 (Color online) Arrhenius plot of the DA rate. Straight lines show results of linear fitting, revealing activation energies of ~ 0.4 eV and ~ 0.1 eV. The inset shows an Arrhenius plot of the cascade density [83] at $R_{cut} = 20$nm revealing an activation energy of 0.1 eV. 88

6.1 (Color online) Selected (a) depth profiles of relative disorder in the Si sublattice and (b) ion channeling spectra of the ^{12}C(α,α)^{12}C resonant scattering, reflecting damage in the C sublattice, for 3C-SiC bombarded at 100 °C with a pulsed beam of 500 keV Ar ions with different values of t_{off} (given in the legend) and all the other parameters fixed (the total dose = 3.5×10^{14} cm^{-2}, $t_{on} = 1$ ms, and $F_{on} = 1.9 \times 10^{13}$ cm^{-2} s^{-1}). For clarity, only every 10th experimental point is depicted. Also shown by a dashed line in (a) is the normalized TRIM-code predicted profile of lattice vacancies for 500 keV Ar ion irradiation of SiC. The projected range and straggling of Ar ions are 329 and 66 nm, respectively. The inset in (a) is a schematic of the time dependence of the instantaneous dose rate for pulsed beam irradiation, defining t_{on}, t_{off}, and F_{on}. 96

6.2 (Color online) Relative bulk disorder in Si and C sublattices (as indicated in the legend) of 3C-SiC bombarded at 100 °C with a pulsed beam of 500 keV Ar ions as a function of the passive portion of the beam cycle (t_{off}). Fitting curves of the data for the Si sublattice with the first and second order rate equations are shown by dashed and solid lines, respectively. 98

6.3 (Color online) Temperature dependence of the ion dose required to reach a damage level of 0.7 in $4H$-SiC bombarded with a continuous beam (i.e., $t_{off} = 0$) of 500 keV Ar ions with a dose rate of 1.7×10^{13} cm^{-2} s^{-1}. The solid line is an exponential fit to the data. The inset is a schematic of the time dependence of the instantaneous dose rate for pulsed beam irradiation, defining t_{on}, t_{off}, and F_{on}. 103

6.4 (Color online) Selected depth profiles of relative disorder in $4H$-SiC bombarded with a pulsed beam of 500 keV Ar ions with $F_{on} = 1.7 \times 10^{13}$ cm^{-2} s^{-1}, $t_{on} = 1$ ms, and different t_{off} values, given in legends (in units of ms), at different temperatures and total doses, also shown in the legends. For clarity, only every 5th experimental point is depicted. 105

6.5 (Color online) Level of relative bulk disorder in $4H$-SiC bombarded with 500 keV Ar ions with $F_{on} = 1.7 \times 10^{13}$ cm^{-2} s^{-1} and $t_{on} = 1$ ms as a function of the passive portion of the beam duty cycle (t_{off}) at different temperatures, given in the legend (in units of °C). Fitting curves of the data with the second order decay equation are shown by solid lines. 106

6.6 (Color online) Closed symbols: temperature dependencies of the effective time constant of DA (τ) and the DA efficiency (ξ) for $4H$-SiC bombarded with 500 keV Ar ions with $F_{on} = 1.7 \times 10^{13}$ cm^{-2} s^{-1} and $t_{on} = 1$ ms. Open symbols show data points for $3C$-SiC irradiated at 100 °C with 500 keV Ar ions with $F_{on} = 1.9 \times 10^{13}$ cm^{-2} s^{-1} and $t_{on} = 1$ ms, taken from Ref. [95]. 107

6.7 Arrhenius plot of the DA rate defined as $1/(\tau(n(0) - n_{inf}))$ for a second order decay process. The straight line shows results of linear fitting, revealing an activation energy of 0.25 ± 0.05 eV for the temperature range of $150 - 250$ °C. 109

7.1 (Color online) Selected depth profiles of relative disorder in Ge bombarded at 110 °C with a pulsed beam of 500 keV Ar ions with F_{on}, t_{on}, and t_{off} given in the legends at total fluences of (a) 4.9×10^{13} cm^{-2} and (b) 7.5×10^{13} cm^{-2}. For clarity, only every 10th experimental point is depicted. Panel (a) is a pulsed beam measurement of τ, whereas (b) is a measurement of L_d. The inset in (a) is a schematic of the time dependence of the instantaneous dose rate for pulsed beam irradiation, defining t_{on}, t_{off}, and F_{on}. 115

7.2 (Color online) Relative bulk disorder in Ge bombarded with a pulsed beam of 500 keV Ar ions with $F_{on} = 4.3 \times 10^{13}$ cm^{-2} s^{-1} and $t_{off} = 100$ ms as a function of the fluence per pulse ($F_{on}t_{on}$). Linear fitting, shown by the solid line, gives an effective diffusion length (L_d) of 38 ± 6 nm. 117

7.3 (Color online) Relative bulk disorder in Ge bombarded with a pulsed beam of 500 keV Ar ions with $F_{on} = 1.5 \times 10^{13}$ cm^{-2} s^{-1} and $t_{on} = 1$ ms as a function of the passive portion of the beam duty cycle (t_{off}) at different Ts given in the legend (in units of °C). Fitting curves with the second order decay equation are shown by solid lines. The inset shows the temperature dependence of the total ion fluence required to achieve a relative bulk disorder level of $\sim 0.5 - 0.8$ for continuous beam irradiation. 118

7.4 (Color online) Temperature dependencies of the effective time constant of DA (τ, left axis) and the DA efficiency (ξ, right axis) for Ge bombarded with 500 keV Ar ions. The inset shows an Arrhenius plot of the dynamic annealing rate. Straight lines are results of linear fitting, revealing activation energies of 1.28 ± 0.07 eV and 0.13 ± 0.03 eV, above and below 130 °C, respectively. 120

8.1 (Color online) Selected depth profiles of relative disorder in Si for 500 keV Ar irradiation of (a) pristine, (b) predamaged with defect clusters to a dose of 4.5×10^{14} cm^{-2}, and (c) the 500 °C clamshell defect with a continuous ($t_{off} = 0$) and pulsed ($t_{off} = 1, 3$ ms). The defect state prior to pulsed irradiation is shown by solid circles in (b) and (c). For clarity, only every 10th experimental point is depicted. The inset in (a) is a schematic of the time dependence of the instantaneous dose rate for pulsed beam irradiation, defining t_{on}, t_{off}, and F_{on}. 128

8.2 (Color online) Relative bulk disorder in Si bombarded with a pulsed beam of 500 keV Ar ions with $F_{on} = 1.9 \times 10^{13}$ cm^{-2} s^{-1} and $t_{on} = 1$ ms as a function of the passive portion of the beam duty cycle (t_{off}) for the 500 °C clamshell defect, a sample preimplanted with 500 keV Ar to a dose of 4.5×10^{14} cm^{-2}, and a pristine sample. Fitting curves with the first (second) order decay equation are shown by solid (dashed) lines. 129

8.3 (Color online) Dependence of τ on the total relative disorder with zero pre-damage (bottom axis) and as a function of pre-damage relative disorder (top axis). 130

8.4 (Color online) Plot of the dynamic annealing efficiency as a function of the total relative disorder with zero pre-damage (bottom axis) and as a function of the pre-damage relative disorder (top axis). 132

8.5 (Color online) Selected RBS channeling depth profiles of relative disorder of the pristine Si 0 ms irradiation and the 500 and 600 °C clamshell defects prior to pulsed irradiation by 500 keV Ar (top pane) and τ as a function of depth for the pristine and 500 and 600 °C clamshell defect. 134

LIST OF TABLES

TABLE — Page

3.1 Irradiation conditions of this study: the maximum instantaneous dose rate (F_{on}), total ion dose (Φ), the characteristic time constant of defect interaction processes (τ), and the efficiency of dynamic annealing (ξ). Ion energy was 500 keV for all four ion masses. Data for Ar ions for $F_{on} = 1.2 \times 10^{13}$ cm^{-2} s^{-1} is taken from Ref. [12]. 12

1. INTRODUCTION*

1.1 Motivation

An energetic particle propagating through a crystalline target transfers its kinetic energy via interaction with electrons and nuclei of target atoms. Such ballistic energy transfer could result in the displacement of atoms from their equilibrium lattice sites and the formation of defects. Frenkel pairs (i.e., vacancies and interstitials) are the simplest ballistically-generated defects. Since many material properties are influenced by lattice defects, radiation damage in solids has been studied extensively for many decades. [1] Despite this, our current understanding of the underlying physics is still not sufficient for *predicting* radiation damage even for Si, which is arguably the simplest and most extensively studied material. [1] Currently, experimental data is relied on to find out the type and concentration of stable lattice defects in any material for any given set of ion bombardment conditions (i.e., ion mass, energy, dose, dose rate, and target temperature).

The lack of predictability of radiation damage is caused by the overall complexity and our limited understanding of radiation defect physics. The complexity is related to the fact that, for most practically relevant irradiation conditions and materials, Frenkel pair components are mobile during irradiation and could interact with each other and with pre-existing defects, surfaces, and interfaces. This defect interaction process occurring during ion bombardment is often referred to as *dynamic annealing* (DA). [1] As a result of DA, in most practical cases, what is measured in solids after irradiation is not Frenkel pair components ballistically generated in ion-atom

* Portions of this work are reprinted from Journal of Applied Physics, Vol 118 / Issue 13, J. B. Wallace, S. Charnvanichborikarn, L. B. Bayu Aji, M. T. Myers, L. Shao, S. O. Kucheyev, "Radiation defect dynamics in Si at room temperature studied by pulsed ion beams," Pages No. 135709, Copyright (2015), with the permission of AIP Publishing.

collisions but more complex lattice defects (such as point defect clusters, extended defects, and voids) that are the product of dynamic defect interaction.

Radiation damage processes in solids are further complicated by the following three interrelated aspects of defect physics. First, ballistically-generated displacements evolve into a spectrum of stable lattice defects rather than into a single type of stable defects (e.g., divacancies). [1,2] Direct measurements of the types and concentrations of radiation defects in solids are not trivial. Second, defects often accumulate nonlinearly with ion dose. [1] The efficiency of the formation of stable defects (i.e., the fraction of ballistically generated Frenkel pairs that do not eventually annihilate but contribute to the formation of stable lattice defects) depends on the type and concentration of defects present in the lattice. Such pre-existing defects can either enhance or suppress the efficiency of the formation of stable disorder from primary atomic displacements. Third, the formation of stable defects is a dynamic process that depends on the generation *rate* of atomic displacements. This manifests as both the dependence of damage buildup on the volumetric density of displacements in collision (sub)cascades (defined by the target composition and the mass and energy of ions) and as a dose rate (or beam flux) effect. For the same total concentration of ballistically-generated atomic displacements, which is commonly expressed as displacements per atom (DPAs), the type and concentration of resultant stable lattice defects depend on the density of individual collision cascades and on the rate at which the cascades are produced. This dissertation focuses on the dynamic behavior of radiation damage accumulation, which derives from defect generation rate effects.

Measurements of the dose rate effect have traditionally been used to study the aspects of radiation defect dynamics related to the interaction of defects originating in different collision cascades created in close proximity of each other. [1,3–10] The dose rate effect manifests as the dependence of stable radiation disorder on the dose rate

when all the other irradiation parameters are kept constant. It involves a convolution of both spatial and temporal parameters of radiation defect dynamics. Indeed, the dose rate effect originates from a finite time scale of DA processes and finite sizes of defect diffusion regions around individual ballistic collision cascades. The main challenge of the dose rate effect approach is that experimental dependencies of the amount of radiation damage on the dose rate offer limited quantification of radiation dynamics without serious assumptions about explicit defect interaction processes. [5, 9–11]

1.2 Pulsed ion beam technique

In order to separate the spatial and temporal aspects of the radiation defect dynamics, a recently developed pulsed-ion-beam method is utilized. [12–14] In this approach, the total ion dose is delivered as a train of equal square pulses, each with the duration of the active part of the pulse t_{on} and the maximum instantaneous dose rate F_{on}, followed by a passive part of the pulse with duration t_{off} when the beam is steered off the target. A schematic of the pulsing arrangement is shown in Fig. 2.1. The dose per each pulse is $F_{\mathrm{on}} \times t_{\mathrm{on}}$. This method was recently applied to study DA in float-zone grown Si bombarded at room temperature (RT) with 500 keV ^{40}Ar ions. [12, 13] Results showed that, at least for these irradiation conditions, radiation defect dynamics after the thermalization of collision cascades (i.e., after $\sim$ 1 ps from the ballistic formation of the cascade) could be described by the following two parameters: the characteristic time constant τ of DA and the effective defect diffusion length L_d. In this scenario, [12–14] defect dynamics after cascade thermalization is viewed as the diffusion of some dominant point defects (whose origin remained unknown for over three decades) to a distance L_d over time τ.

1.3 Dissertation structure

This dissertation is organized into nine sections. Section 2 provides an in-depth description of the experimental methodology with a detailed discussion of the pulsed ion beam method and the characterization methods used in this study. Section 3 shows the effect of ion mass (and hence cascade density) on the dynamic annealing behavior in room temperature Si. Section 4 shows the behavior of the defect lifetime with changing temperature and reveals activation energies of the dominant dynamic annealing processes in Si. With the groundwork from Sections 3 and 4 in place, Section 5 makes use of a fractal model of collision cascades to describe effects of cascade density on the defect lifetime, diffusion length, and the dominant processes of dynamic annealing in Si. Section 6 demonstrates the pulsed beam method in $3C-$SiC and $4H-$SiC. Section 7 extends the pulsed beam method to Ge. Finally, Section 8 demonstrates the pulsed beam method for measuring the influence of lattice defects on the defect lifetime in Si. Finally, Section 9 summarizes the key findings of this dissertation.

2. METHODOLOGY

2.1 Pulsed ion beam method

The 4 MV ion accelerator (National Electrostatics Corporation, model 4UH) at Lawrence Livermore National Laboratory was used for both ion irradiation and ion channeling analysis. Bombardment was done with 500 keV $^{20}Ne^{+}$, $^{40}Ar^{+}$, $^{84}Kr^{+}$, or $^{129}Xe^{+}$ ions at 7° off the [100] direction to minimize channeling effects. In order to avoid complexity related to differences between instantaneous and average dose rates inherent to experiments with rastered ion beams, all irradiations were performed in a broad beam mode. Beam pulsing was performed by applying high voltage pulses to a pair of plates deflecting the beam in the vertical direction on and off the final beam defining aperture. A schematic of the pulsing arrangement is shown in Fig. 2.1.

2.1.1 Pulsing parameters

In the pulsed ion beam method, the total ion fluence is split into a train of pulses, each with an instantaneous dose rate (F_{on}), duration (t_{on}), and time between pulses (t_{off}). Each of these parameters are defined in Fig. 2.1.

2.1.2 Diffusion length

For L_d measurements, [15–17] the total fluence was delivered as a train of pulses with duration (t_{on}) varying between 0.2 and 100 ms, separated by a t_{off}, which, as will be shown below, is much greater than the defect lifetime (τ) values. The instantaneous flux F_{on} is chosen such that the longest $t_{on} < \tau$. The pulsing schematic for L_d measurements is shown in the inset of Fig. 2.1.

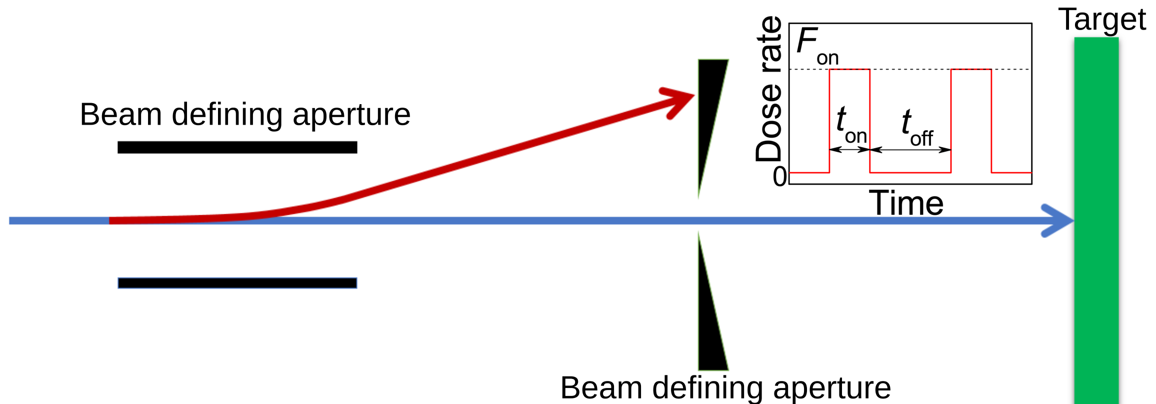

Figure 2.1: Schematic of the pulsed ion beam arrangement showing the ion beam passing through the set of electrostatic beam steering plates and the beam defining aperture into the final chamber where ions bombard the sample. The inset is a schematic of the time dependence of the instantaneous dose rate for pulsed beam irradiation, defining t_{on}, t_{off}, and F_{on}.

2.1.3 Characteristic defect lifetime

For τ measurements, the total fluence was delivered as a train of pulses with fixed duration (t_{on}), separated by a t_{off} which was varied between 0.2 and 100 ms. The dose per pulse, $\Phi_p = F_{on}t_{on}$ is chosen in order to maximize the dynamic annealing effect and allow sufficient spatial overlap between ion cascades. Additional discussion on the choice of Φ_p can be found in section 3. The pulsing schematics is shown in the inset of Fig. 2.1.

2.2 Samples

To improve thermal contact, the samples were attached to a Ni or Cu sample holder with silver paste. Temperature was measured by two thermocouples attached to the sample holder at the opposite ends of the sample matrix. The thermocouples were thermally anchored with silver paste. Ion-beam heating effects were negligible ($\lesssim 0.1$ °C) for the dose rate and ion energy used in this dissertation.

2.2.1 Silicon

Float-zone (FZ) grown (100) Si single crystals with a resistivity of $\sim 5\ \Omega$ cm were used in the majority of pulsed beam experiments in this dissertation. To study possible effects of dopants on radiation dynamics, in some experiments, heavily B-doped Czochralski (CZ) grown (100) Si crystals with a resistivity of $\sim 0.02\ \Omega$ cm were used.

2.2.2 Silicon carbide

SiC irradiations were done with single-crystal epilayers of (001) 3C-SiC epitaxially grown on 3-inch-diameter Si substrates at NOVASiC (thickness of $\gtrsim 2\ \mu$m) and high purity semi-insulating (0001) 4H-SiC single crystals (with a diameter of 100 mm, a resistivity of $\geq 109\ \Omega$cm, and a nominal micropipe density of < 60 cm$^{\text{âĹŠ2}}$), obtained from Cree, Inc.. The crystal quality of as-received films was verified by measuring a minimum 2 MeV He ion channeling yield of $\sim 1.5\%$, consistent across the wafer.

2.2.3 Germanium

Ge irradiations were performed using Czochralski grown (100) Ge single crystals doped with Ga (with a resistivity of $\sim 0.03\ \Omega$ cm).

2.3 Characterization

2.3.1 Rutherford backscattering spectroscopy

After ion irradiation, lattice disorder was measured *ex-situ* at RT by Rutherford backscattering/channeling (RBS/C) spectrometry with 2 MeV $^4He^+$ ions incident along the [100] direction and backscattered into a detector at 164° relative to the incident beam direction. Spectra were analyzed with one of the conventional algorithms [18] for extracting the effective number of scattering centers (referred to below as "relative disorder"). The level of bulk disorder was defined as an average and error

bars as the standard deviation over 20 channels ($\sim$ 40 nm) around the bulk peak maximum. The spot size of the He beam was $\sim 1.5\times1.5$ mm^2. Doses and dose rates were limited to $\sim 2\times10^{16}$ cm^{-2}.

2.3.2 Nuclear reaction analysis

For measuring damage in the C sublattice in 3*C*-SiC by channeling, the same scattering geometry as RBS/C was used but with 4.3 MeV $^4He^{2+}$ ions, taking advantage of the $^{12}C(\alpha,\alpha)^{12}C$ resonant reaction at $\sim$ 4.28 MeV that has an $\sim$ 100-fold larger scattering cross section compared to Rutherford. [19] Relative disorder in the C sublattice was defined as $\frac{Y-Y_{virgin}}{Y_{random}-Y_{virgin}}$, where Y, Y_{virgin}, and Y_{random} are channeling yields at the resonant energy from the sample of interest, an un-irradiated sample, and amorphous SiC, respectively.

2.3.3 Transmission electron microscopy

Irradiated samples from several experiments were studied by bright- and dark-field XTEM imaging with a Phillips CM300 microscope operating at 300 kV and by XTEM nano-diffraction with a minimally convergent probe with a lateral size of $\sim$ 1.8 nm (FWHM) with a Zeiss Libra microscope operating at 200 keV.

2.4 Facility

The 4 MV ion accelerator (National Electrostatics Corporation, model 4UH) at Lawrence Livermore National Laboratory was used for both ion irradiation and ion channeling analysis. This accelerator is a single-ended Van de Graaff style machine. The source is capable of producing ions from most compressed gases. The accelerator column was maintained at a pressure of $< 10^{-7}$ Torr. A schematic of the ion accelerator is shown in Fig. 2.2.

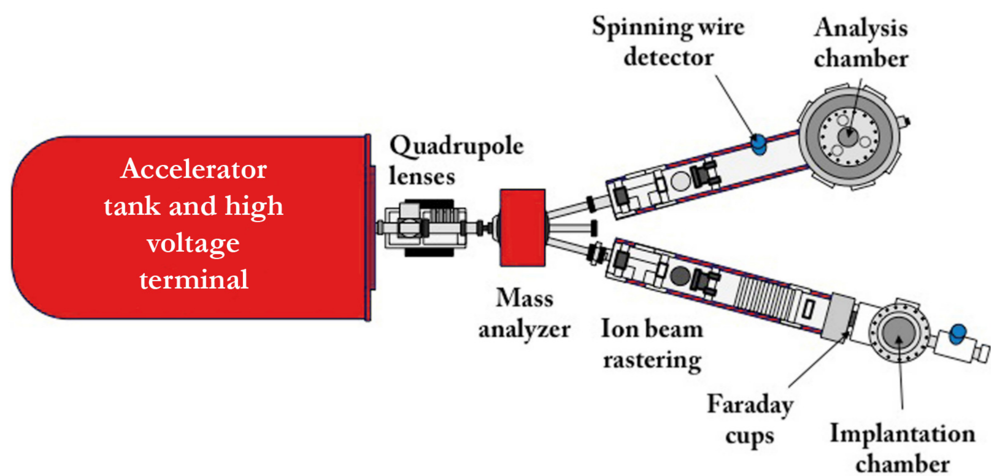

Figure 2.2: Schematic of the 4 MV ion accelerator (National Electrostatics Corporation, model 4UH) at Lawrence Livermore National Laboratory showing both the analysis and implantation beam lines.

3. RADIATION DEFECT DYNAMICS IN SI AT ROOM TEMPERATURE*

3.1 Introduction

The early studies by Myers et al. [12] and Charnvanichborikarn et al. [13] demonstrated the pulsed ion beam method for measuring the defect lifetime and diffusion length in Si at RT. At least for the irradiation conditions used in these early studies, radiation defect dynamics after the thermalization of collision cascades (i.e., after ~ 1 ps from the ballistic formation of the cascade) could be described by the following two parameters: the characteristic time constant τ of DA and the effective defect diffusion length L_d. In this scenario, [12–14] defect dynamics after cascade thermalization is viewed as the diffusion of some dominant point defects (whose origin still remains unknown) to a distance L_d over time τ.

They also found [12] that the defect relaxation behavior in Si irradiated at RT with 500 keV Ar ions closely follows a second order kinetic process,

$$n(t_{off}) = n(\infty) + \frac{n(0) - n(\infty)}{1 + \frac{t_{off}}{\tau}}, \tag{3.1}$$

where n is the maximum concentration of stable defects measured by ion channeling in the crystal bulk. In the simplest case of a second order kinetic process (i.e., $\frac{dn}{dt} \propto n^2$), the characteristic time constant τ depends on the initial defect concentration and, hence, could be expected to depend on ion dose and the maximum instantaneous dose rate F_{on}. If so, this would limit the usefulness of the above description

---

* Portions of this work are reprinted from Journal of Applied Physics, Vol 118 / Issue 13, J. B. Wallace, S. Charnvanichborikarn, L. B. Bayu Aji, M. T. Myers, L. Shao, S. O. Kucheyev, "Radiation defect dynamics in Si at room temperature studied by pulsed ion beams", Pages No. 135709, Copyright (2015), with the permission of AIP Publishing.

of radiation damage dynamics with only two parameters (τ and L_d). Moreover, radiation dynamics could also depend on the purity of the target material, which might account for the large discrepancy in previous estimates of τ and L_d in Si by other methods. [12, 13]

In this section, previous work by Myers and Charnvanichborikarn et al. [12, 13] is expanded and the robustness of the pulsed-beam method is evaluated by studying the dependence of τ and L_d in Si at RT on the doping level, ion dose, the instantaneous defect generation rate (defined by F_{on}), the duration of the active part of the pulse (t_{on}), and the average density of collision cascades (which depends on ion mass). Results show that both τ and L_d are essentially independent of the maximum instantaneous dose rate, total ion dose, and the dopant concentration within the ranges studied, demonstrating the robustness of the pulsed-beam method for studying radiation defect dynamics. Interestingly, both τ and L_d increase with increasing ion mass. This demonstrates that the average density of collision cascades influences not only the efficiency of damage accumulation and annealing but also defect dynamics. Finally, the (non-trivial) choice of pulsing parameters for measurements of τ and L_d is discussed.

3.2 Experiment

3.2.1 Targets

Float-zone (FZ) grown (100) Si single crystals with a resistivity of $\sim 5\ \Omega$ cm were clamped to a metal holder (Al, Ni, or Cu) with a thin layer of Cu-powder-impregnated thermal grease or Ag paste in between to improve thermal contact. To study possible effects of dopants on radiation dynamics, in some experiments, heavily B-doped Czochralski (CZ) grown (100) Si crystals with a resistivity of $\sim 0.02\ \Omega$ cm were used.

Table 3.1: Irradiation conditions of this study: the maximum instantaneous dose rate (F_{on}), total ion dose (Φ), the characteristic time constant of defect interaction processes (τ), and the efficiency of dynamic annealing (ξ). Ion energy was 500 keV for all four ion masses. Data for Ar ions for $F_{on} = 1.2 \times 10^{13}$ cm^{-2} s^{-1} is taken from Ref. [12].

Ion	F_{on} (10^{13} cm^{-2}s^{-1})	Φ (10^{13} cm^{-2})	τ (ms)	ξ (%)
^{20}Ne	2.9	80	3.6 ±0.3	95
^{40}Ar	1.2	24	6.0 ±1.5	78
^{84}Kr	0.5	6.9	6.7 ±0.4	59
^{129}Xe	0.3	3.5	13.0 ±1.4	34
^{40}Ar	2.2	20	4.8 ±0.4	74
^{40}Ar	0.5	20	3.4 ±1.0	75
^{40}Ar	1.3	17	7.6 ±1.9	80
^{40}Ar	1.3	14	5.1 ±3.1	66
^{40}Ar	0.5	14	7.8 ±2.8	83

3.2.2 Ion bombardment and ion channeling analysis

The 4 MV ion accelerator (National Electrostatics Corporation, model 4UH) at Lawrence Livermore National Laboratory was used for both ion irradiation and ion channeling analysis. Bombardment was done with 500 keV ^{20}Ne^{+}, ^{40}Ar^{+}, ^{84}Kr^{+}, or ^{129}Xe^{+} ions at 7° off the [100] direction to minimize channeling effects. As described in detail previously, [12, 13] in order to avoid complexity related to differences between instantaneous and average dose rates inherent to experiments with rastered ion beams, all irradiations were performed in a broad beam mode. Beam pulsing was performed by applying high voltage pulses to a pair of plates deflecting the beam in the vertical direction on and off the final beam defining aperture.

Three sets of interrelated experiments were performed. First, continuous beam bombardment to a range of doses (with constant dose rates) was carried out to

examine the damage accumulation process. Based on the damage buildup curves measured, for pulsed-beam experiments, the total doses were chosen to produce sub-amorphization damage for the case of continuous beam irradiation (i.e., $t_{off} = 0$). The second and third sets of experiments involved pulsed beam bombardment for the measurement of τ and L_d, respectively. As described previously, [12] in order to measure τ, the active part of the beam cycle, t_{on}, was kept constant at 1 ms (unless stated otherwise), while the passive part, t_{off}, was varied up to 100 ms. To measure L_d, [13] the duration of the passive part of the pulse (t_{off}) was kept constant at 100 ms (which, as shown in Sec. 3.3.2, is much larger than τ for all the irradiation conditions of this study), and the dependence of lattice damage on t_{on} (varied from 0.5 to 100 ms) was studied. For bombardment with different ion masses, the maximum instantaneous dose rate (F_{on}) was chosen to maintain a displacement generation rate of $\sim 2.5 \times 10^{-2}$ DPA s^{-1} at the depth of the maximum nuclear energy loss (R_{pd}). The details of the irradiation experiments performed are given in Table 3.1. Depth profiles of ballistically-generated vacancies [Fig. 3.1(a)] were calculated with the TRIM code (version SRIM-2013.00) [20] with a default threshold energy of 15 eV.

After ion irradiation, lattice disorder was measured by Rutherford backscattering/channeling (RBS/C) spectrometry with 2 MeV ^{4}He$^+$ ions incident along the [100] direction and backscattered into a detector at 164° relative to the incident beam direction. All RBS/C spectra were analyzed with one of the conventional algorithms [18] for extracting the effective number of scattering centers (referred to below as "relative disorder"). Error bars correspond to peak-to-peak noise in RBS/C-derived disorder profiles such as shown in Fig. 3.1(b)–3.1(d).

3.3 Results and discussion

3.3.1 Damage buildup

Figure 3.1(a) shows TRIM-code calculated depth profiles of lattice vacancies ballistically generated in Si by 500 keV Ne, Ar, Kr, or Xe ions. As expected, all four profiles exhibit unimodal Gaussian-like distributions with maxima at R_{pd}s (shown by vertical dashed lines). Representative profiles of stable lattice disorder (measured by RBS/C) produced by continuous beam bombardment (i.e., $t_{off} = 0$) with Ne, Ar, Kr, or Xe ions are shown in Fig. 3.1(b). In contrast to TRIM-predicted displacement distributions of Fig. 3.1(a), such experimental damage–depth profiles of Fig. 3.1(b) are bimodal with a relatively small peak at the sample surface and the main well-defined broad peak in the bulk at depths close to R_{pd} values. For heavy ions (Ar, Kr, and Xe), the overall shape of damage–depth profiles in Fig. 3.1(b) is close to that of ballistically generated displacements [Fig. 3.1(a)]. However, for lighter Ne ions, this shape deviates qualitatively, with the damage level in RBS/C-derived profiles nearly constant at $\sim 5\%$ in the first ~ 400 nm, and the major damage peak situated between ~ 600 and ~ 1000 nm from the surface, centered on the R_{pd}.

For all four ion species, the bulk damage accumulates monotonically with ion dose until Si is fully amorphized. The condition of the RBS/C yield reaching the random level (corresponding to a relative disorder level of 100% in RBS/C-derived damage profiles such as shown in Figs. 3.1(b)–3.1(d)) does not necessarily imply lattice amorphization. However, for Si at RT, amorphization has been confirmed by numerous previous electron microscopy investigations. [1,5,21–24] This is illustrated in Fig. 3.2, which shows disorder levels measured at the maxima of bulk damage peaks as a function of ion dose (in DPA at the R_{pd}). All damage buildup curves in Fig. 3.2 are nonlinear with sigmoidal shapes, indicating that the efficiency of the formation

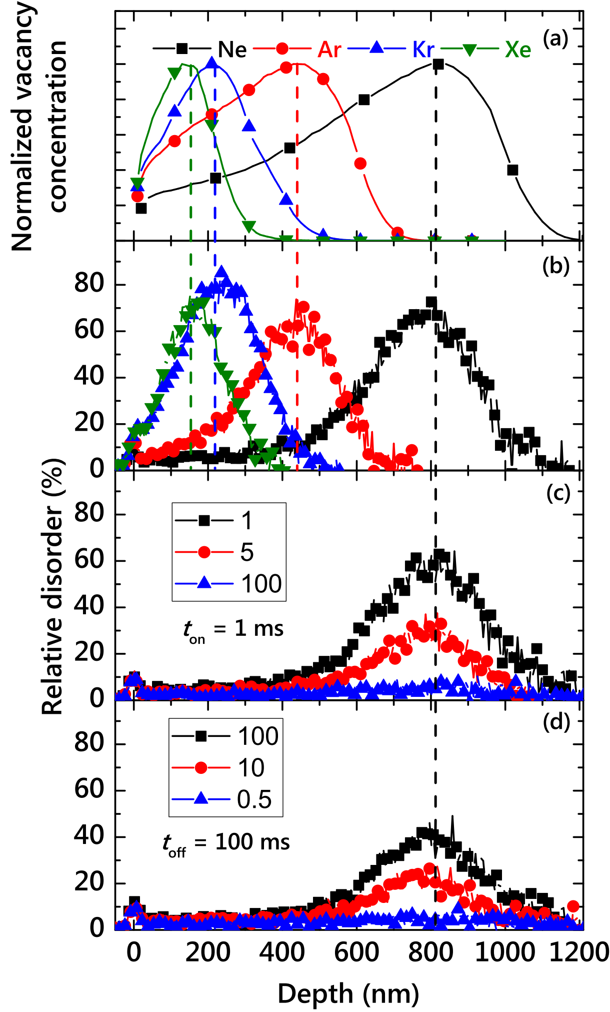

Figure 3.1: (Color online) (a) Normalized depth profiles of the concentration of lattice vacancies ballistically generated in Si by irradiation with 500 keV ^{20}Ne, ^{40}Ar, ^{84}Kr, or ^{129}Xe ions. Results of TRIM-code simulations. Positions of the vacancy distribution maxima (R_{pd}) are indicated by vertical dashed lines (at 795, 445, 210, and 150 nm). (b) Selected depth profiles of relative disorder for FZ-Si irradiated with Ne, Ar, Kr, and Xe ions to doses of 8, 2, 0.69, and 0.35×10^{14} cm^{-2} (or 0.77, 0.43, 0.37, and 0.30 DPA at R_{pd}), respectively. The legend in (a), relating symbols to ion masses, also applies to panel (b). Selected depth profiles of relative disorder in FZ-Si bombarded with a pulsed Ne ion beam (c) with different values of t_{off} (indicated in the legend in ms) and $t_{\mathrm{on}} = 1$ ms and (d) with different values of t_{on} (indicated in the legend in ms) and $t_{\mathrm{off}} = 100$ ms and all the other parameters fixed (a total dose of $\Phi = 8 \times 10^{14}$ cm^{-2} and $F_{\mathrm{on}} = 2.9 \times 10^{13}$ cm^{-2}s^{-1}).

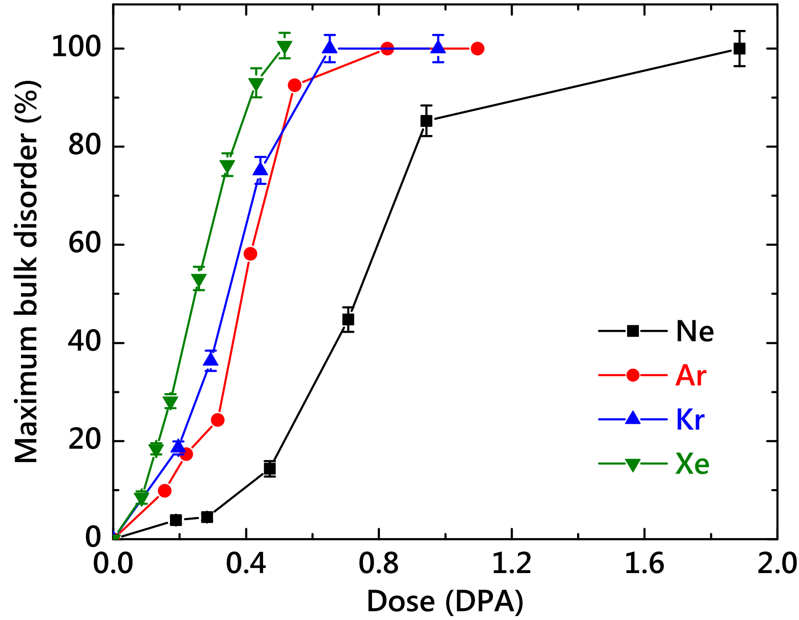

Figure 3.2: (Color online) Dose dependencies of relative disorder at the maximum of the bulk defect peak for FZ-Si bombarded at room temperature with 500 keV Ne, Ar, Kr, or Xe ions with a constant displacement generation rate of $\sim 2.5 \times 10^{-2}$ DPA/s at R_{pd}.

of stable lattice disorder from ballistically generated displacements strongly depends on the (defective) state of the lattice and, hence, on ion dose.

It is also seen from Fig. 3.2 that the damage production efficiency increases dramatically with increasing ion mass. For example, for doses resulting in 0.3 DPA, the bulk damage level differs by ~ 15 times after ^{20}Ne or ^{129}Xe ion bombardment. This is due to the strong dependence of damage production efficiency in Si on the density of collision cascades. Indeed, heavier ions produce denser collision cascades, resulting in nonlinear energy spikes and/or enhanced defect clustering. [1, 10, 25] All of the above findings are in qualitative agreement with previous extensive studies of ion-beam damage in Si at RT with continuous (or unintentionally pulsed during rastering) ion beams. [1, 4–6, 8–10, 12, 23]

Based on the damage buildup curves from Fig. 3.2, total ion doses (Φ) were selected for pulsed-ion-beam experiments so that stable disorder levels (n) produced by continuous beams (i.e., $t_{off} = 0$) with different ion masses are readily measurable by RBS/C and are below the amorphization level (i.e., $10 \lesssim n \lesssim 80\%$, with 100% corresponding to full amorphization).

3.3.2 Dynamic annealing time constant

Figure 3.1(c) shows representative damage–depth profiles for pulsed-ion-beam measurements of τ for the case of Ne-ion bombardment with three different t_{off} values and all the other parameters kept constant. It is seen from Fig. 3.1(c) that an increase in t_{off} from 1 to 100 ms leads to a dramatic reduction in the bulk damage level (n), while the surface defect peak remains unchanged. Such a trend of the reduction in n with increasing t_{off} applies to all the measurements of $n(t_{off})$ dependencies in the present study (Table 3.1). It is also consistent with previous pulsed-ion-beam investigation [12] of Si under 500 keV Ar ion irradiation.

The evolution of bulk disorder as a function of t_{off} for Ar ion bombardment is illustrated in Fig. 3.3, showing $n(t_{off})$ dependencies for cases with different Φ, F_{on}, and the initial doping level (FZ vs CZ crystals). Dashed lines in Fig. 3.3 are fitting curves with the second order rate equation (Eq. 3.1). The legend of Fig. 3.3 and Table 3.1 list values of the fitting parameters τ and the dynamic annealing efficiency ξ, which is defined as $\xi = \frac{n(0)-n(\infty)}{n(0)}$. These results reveal that, for 500 keV Ar ion bombardment at RT, within experimental errors, dynamic annealing obeys a second order kinetic behavior with a τ of ~ 5 ms, independent of Φ, F_{on}, and the initial doping level in the range studied. This demonstrates the robustness of the pulsed beam method and the description of the inherently complex DA process by a simplified scenario involving the (trap-limited) diffusion of some dominant mobile

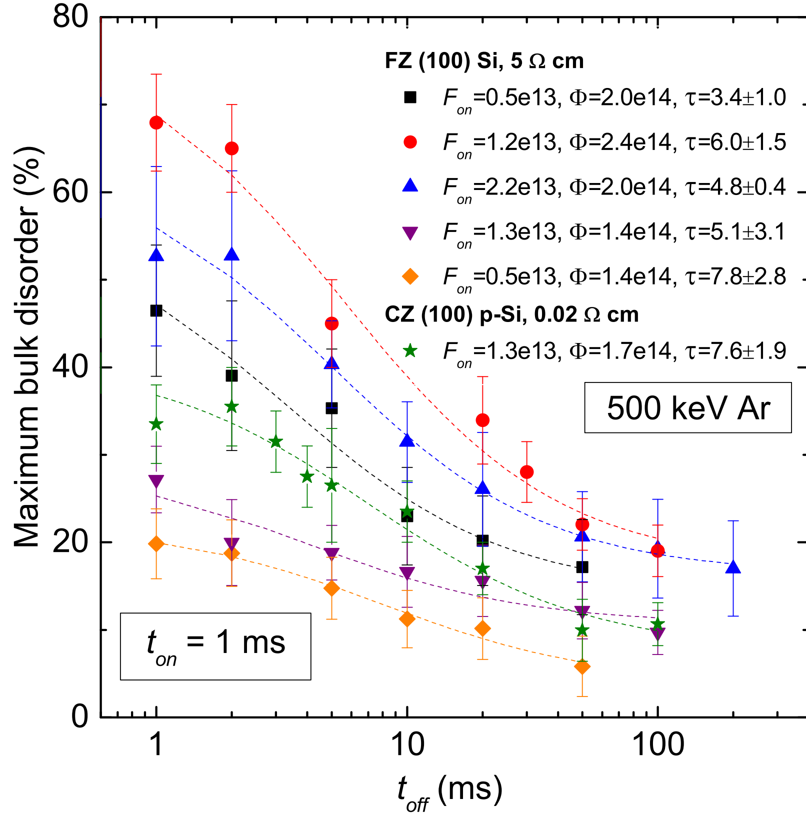

Figure 3.3: (Color online) Dependencies of relative disorder at the maximum of the bulk defect peak in FZ- and CZ-Si bombarded at room temperature with a pulsed beam of 500 keV ^{40}Ar ions with t_{on} = 1 ms and different F_{on} and Φ (given in the legend in units of cm^{-2} s^{-1} and cm^{-2}, respectively) on the duration of the passive part of the cycle, t_{off}, and all the other parameters fixed. Dashed lines are fitting curves of the second order rate equation (Eq. 3.1), with τ values shown in the legend in ms.

(unstable) defects to distances L_d over time τ.

Figure 3.3 and Table 3.1 also show that ξ increases with decreasing F_{on}. This is expected since, with the choice of F_{on} and t_{on} discussed in more detail in Sec. 3.3.4, ξ is essentially the magnitude of the dose rate effect, reflecting the difference between levels of stable lattice damage for irradiation with a continuous beam with a dose rate equal to F_{on} (for $t_{off} = 0$) and a continuous beam with the dose rate approaching

zero (for $t_{off} >> \tau$), when all individual collision cascades are allowed to fully relax before the impact of subsequent collision cascades with overlapping damage zones. Hence, pulsed ion beam bombardment with t_{on} lower than the critical value for defect interaction within each pulse (see Secs. 3.3.3 and 3.3.4) and $t_{off} >> \tau$ allows us to study the limiting case of dynamically non-interacting cascades (i.e., equivalent to $F_{on} \rightarrow 0$ with a continuous beam), which is challenging to access in conventional dose rate experiments due to prohibitively long irradiation times and associated beam stability and dosimetry issues.

Figure 3.4 and Table 3.1 illustrate the effect of ion mass on the $n(t_{off})$ dependence and, hence, on τ and ξ. The second order kinetic behavior for all the four ion species studied. Ion mass dependencies of τ and ξ are better illustrated in Fig. 3.5(a). With increasing ion mass, ξ rapidly decreases. This indicates that, for heavier ions, the intra-cascade formation of stable lattice disorder becomes more efficient and a smaller fraction of atomic displacements participate in DA processes. Figure 3.5(a) also reveals that τ increases with increasing ion mass and, hence, cascade density. Therefore, the cascade density influences not only the defect production efficiency (the fact that has been well established albeit not fully understood) [1, 25] but also the defect interaction dynamics.

The above result of the increase in τ with increasing ion mass is non-trivial. In fact, the sign of this cascade density effect on defect interaction dynamics is the opposite of what was suggested by Kinomura, Williams, and Fujii [26] in their systematic study of the ion mass effect on the rate of ion-beam-induced epitaxial crystallization (IBIEC) in Si. Indeed, they [26] argued that τ should be smaller for heavier ions, which would be expected for simple cases of nonlinear defect accumulation such as the formation of divacancies by trapping of two isolated vacancies. In such cases, an increase in cascade density should result in more efficient and faster defect annihila-

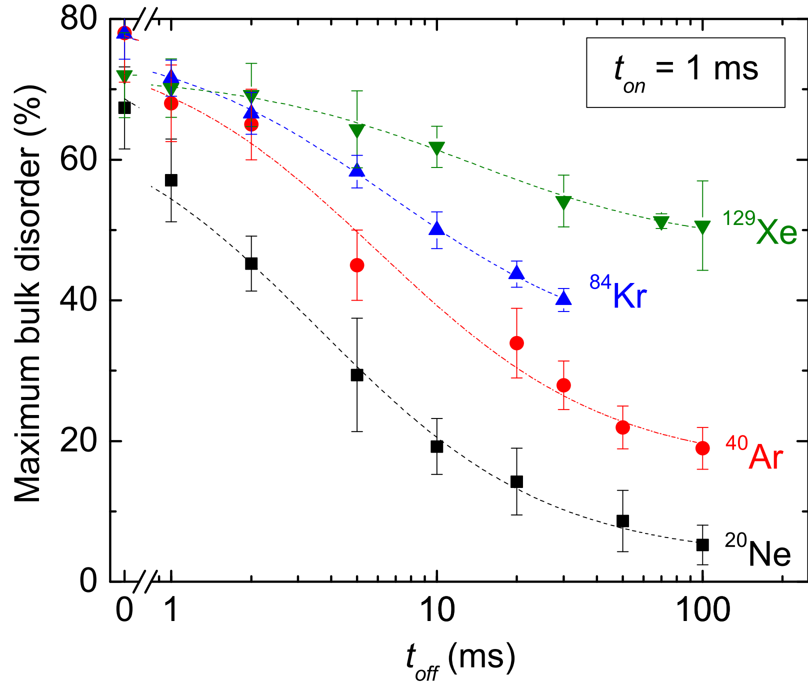

Figure 3.4: (Color online) Dependencies of relative disorder at the maximum of the bulk defect peak in FZ-Si bombarded at room temperature with pulsed beams of 500 keV ^{20}Ne, ^{40}Ar, ^{84}Kr, or ^{129}Xe ions on the duration of the passive part of the cycle, t_{off}, and all the other parameters fixed, as listed in Table 3.1. Solid lines are fitting curves with the second order rate equation (Eq. 3.1).

tion and, hence, shorter τ. Such arguments [26] contradict experimental finding that τ increases with increasing ion mass [Fig. 3.5(a)]. This illustrates the currently limited understanding of radiation defect dynamics even in the most extensively studied and arguably best understood material such as single-crystalline Si and highlights the need for further studies of radiation defect dynamics.

Understanding atomic-level mechanisms of the mass dependence of τ revealed by Figs. 3.4 and 3.5(a) will require comparison of experimental data with results of atomistic modeling. This is a formidable task that is beyond the scope of the present work. Instead, a defect interaction scenario is proposed herein that is consistent with experimental observations.

When describing radiation defect dynamics, all radiation-produced defects could divide into the following two major categories: mobile and stable lattice defects. For Si under ion bombardment at RT, likely only two types of defects are mobile and dominant: vacancies (Vs) and interstitials (Is). [2] Moreover, for relatively high ion doses and damage levels of relevance to electronics and nuclear materials applications and used in the present study, neutral vacancies and interstitials likely dominate, as the concentration of radiation-generated (stable) lattice defects largely exceeds the initial dopant concentration, and the material is in a semi-insulating state. [2] Defects that have negligible thermally-activated mobility and the rate of thermally-induced dissociation (at RT) over the time scales between ion irradiation and post-irradiation analysis typical for the experiments herein (i.e., up to several months) are referred to as "stable". For Si at RT, the divacancy ($2V$) is the best known example of stable defects, but many more complex stable point defect clusters are likely to form during ion irradiation. [2] Such stable defects could be annihilated or transformed to other defect types during ion irradiation as a result of their interaction with mobile defects. An example is the $2V + I \to V$ process.

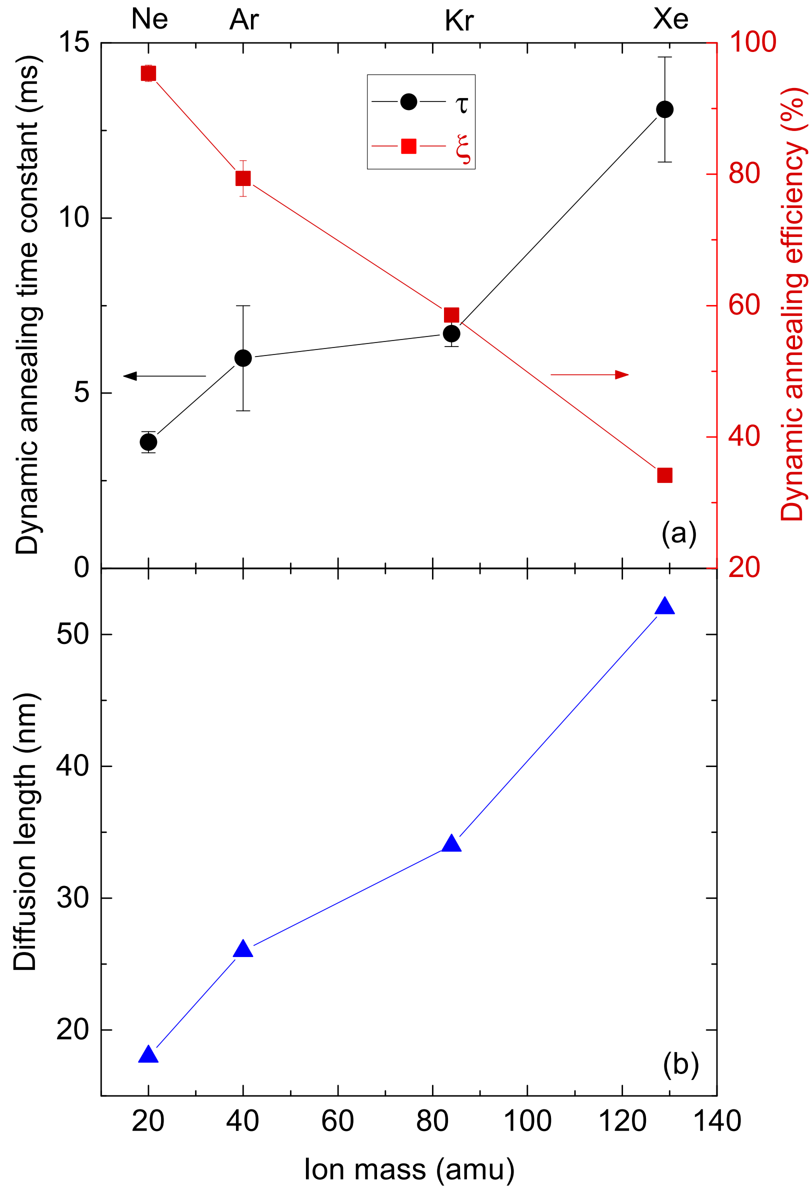

Figure 3.5: (Color online) Dependence of [(a), left axis] the DA time constant (τ), [(a), right axis] the DA efficiency (ξ), and (b) defect diffusion length (L_d) on ion mass for FZ-Si bombarded at room temperature with pulsed beams of 500 keV Ne, Ar, Kr and Xe ions with $t_{on} = 1$ ms and F_{on} values of 2.9, 1.2, 0.5, and 0.3 $\times$ 10^{13} cm^{-2} s^{-1}, respectively.

The type of the dominant mobile defects is not expected to depend strongly on cascade density. These are likely Vs and Is for Si at RT for all the irradiation conditions of this work. Both the instantaneous concentration of mobile defects and the type of stable lattice defects could, however, depend on the cascade density. For example, energy spikes form in dense subcascades generated by heavy ions, resulting in the formation of large defect clusters and inclusions of amorphous Si. [24,25,27,28] Such defect clusters or the amorphous/crystalline interface of amorphous zones could act as traps for migrating point defects, Vs and/or Is. If the trapping well depth is shallow, thermally-induced de-trapping (release) will follow. Such a trapping/release cycle slows down the defect relaxation dynamics. This could explain larger τ values measured here for irradiation with heavier ions that create denser collision cascades resulting in the formation of intra-cascade defect clusters and amorphous zones. Future systematic measurements of temperature dependencies of τ and ξ (and activation energies of the underlying processes) could shed light on the types of mobile defects and the defect reaction processes that dominate defect relaxation kinetics.

3.3.3 Defect diffusion length

3.3.3.1 Pulsed ion beam measurement of L_d

As discussed previously, [13] the effective diffusion length (L_d) of dominant mobile defects can be evaluated in pulsed-ion-beam experiments by measuring the dependence of the post-irradiation stable damage level (n) on t_{on}, with all the other irradiation parameters kept constant. Figure 3.1(d) shows representative damage–depth profiles for Si irradiated at RT with a pulsed beam of 500 keV Ne ions with different t_{on} and the same $t_{off} = 100$ ms (and, hence, $t_{off} >> \tau$ based on results from Sec. 3.3.2). It is seen from Fig. 3.1(d) that, with increasing t_{on}, n increases, while the height of the surface defect peak remains constant. The same trend of an

increase in n with increasing t_{on} is observed in all the $n(t_{on})$ measurements of the present study, which is also consistent with previous data for Ar ions. [13]

Figure 3.6 shows $n(t_{on})$ dependencies for Si bombarded with Ar ions with three different values of F_{on}. For all these F_{on} values, n is essentially independent of t_{on} for $t_{on} \lesssim t_{on}^{L_d}$ and increases for $t_{on} \gtrsim t_{on}^{L_d}$. Here, $t_{on}^{L_d}$ is the critical pulse duration for which mobile defects originating from different collision cascades begin to interact. It is seen from Fig. 3.6 that the value of $t_{on}^{L_d}$ depends on F_{on}. This is expected. Indeed, for $t_{on} = t_{on}^{L_d}$, the dose per every pulse is $F_{on}t_{on}^{L_d}$, and the average lateral distance between the centers of adjacent collision cascades is $L_{overlap} = \frac{1}{\sqrt{F_{on}t_{on}^{L_d}}}$. For every pulse, the interaction between mobile defects created in different collision cascades occurs only when the lateral distance between cascades is comparable or smaller than the effective diffusion length of mobile defects: $L_{overlap} \lesssim 2L_d$ (a factor of 2 is present since L_d defines the radius rather than the diameter of the effective defect interaction area).

The evaluation of L_d is better visualized when $n(t_{on})$ dependencies from Fig. 3.6 are replotted as $n(\frac{1}{2}L_{overlap})$. This is shown in Fig. 3.7 together with data for Ne, Kr, and Xe ions. As expected, the three curves for Ar ions for different values of F_{on} from Fig. 3.6 overlap each other in Fig. 3.7, revealing $L_d \approx 28$ nm. Bombardment with Ne ions is characterized by a slightly smaller L_d of ~ 17 nm, while the data for Kr and Xe ions reveals larger L_d, despite larger error bars due to the reduction in ξ with increasing ion mass. Such a monotonic increase in L_d with increasing ion mass is better illustrated in Fig. 3.5(b). The fact that L_d is larger for heavier ions is consistent with an increase in τ with increasing ion mass [Fig. 3.5(a)]. However, L_d does not scale as $L_d \propto \sqrt{\tau}$, indicating that the effective defect diffusivity also depends on cascade density.

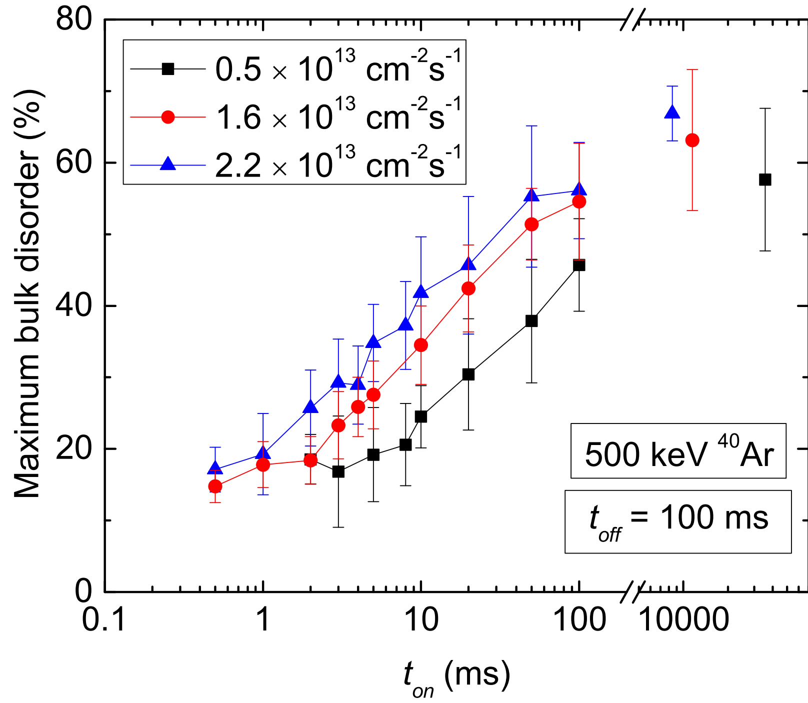

Figure 3.6: (Color online) Dependence of relative disorder at the maximum of the bulk defect peak in FZ-Si bombarded at room temperature with a pulsed beam of 500 keV ^{40}Ar ions with $t_{off} = 100$ ms and different F_{on} (as indicated in the legend) to a total dose of 2.2×10^{14} cm^{-2} on the duration of the active part of the cycle, $t_{\rm on}$.

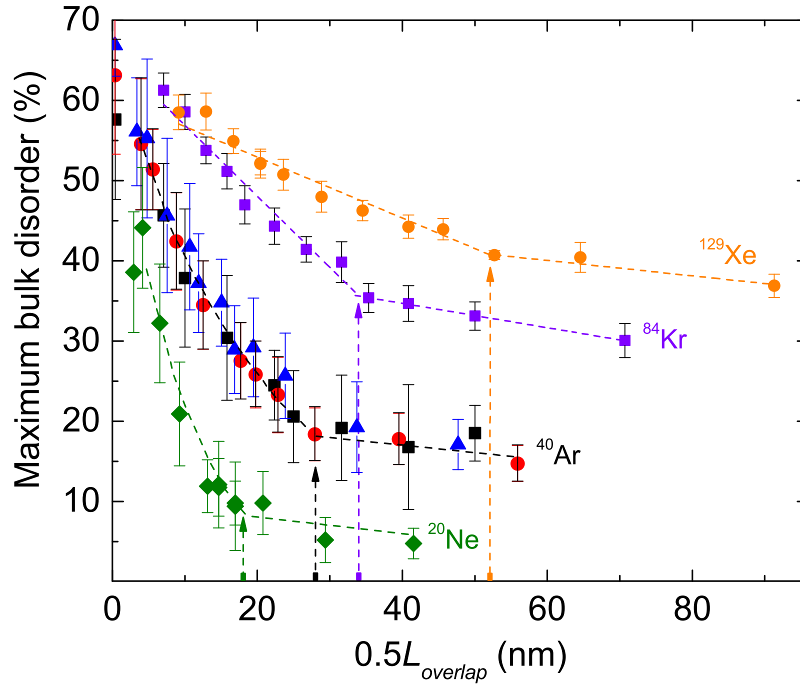

Figure 3.7: (Color online) Dependence of relative disorder at the maximum of the bulk defect peak in FZ-Si bombarded at room temperature with pulsed beams of 500 keV ^{20}Ne, ^{40}Ar, or ^{129}Xe ions with $t_{off} = 100$ ms (and different F_{on} of Ar ions) on the half of the average lateral distance between collision cascades in each pulse ($L_{overlap}$). Dashed lines are to guide the reader's eye. Arrows mark L_d values.

3.3.3.2 Variable-beam-tilt measurement of L_d

Figure 3.8 shows results of an alternative method of L_d measurements based on the difference of damage–depth profiles for cases of bombardment with ion beams tilted to different angles relative to the surface normal. This variable-beam-tilt approach was recently used to study the effect of the sample surface on radiation damage in GaN and ZnO crystals. [29, 30] In such experiments, ion mass and energy (and, hence, the density of collision cascades) are fixed (500 keV Xe for data in Fig. 3.8), and ion bombardment is performed for different beam tilt angles with constant displacement generation rates and total displacements at R_{pd}s. Figure 3.8(a) shows normalized displacement generation profiles, while Figs. 3.8(b) and 3.8(c) show RBS/C-derived damage–depth profiles for two different doses for Si bombardment with 500 keV Xe ion beams tilted to three different angles relative to the surface normal.

Figure 3.9 shows results of the analysis of data for variable beam-tilt Xe-ion irradiation of Si, including the dose dependence of the surface peak intensity [Fig. 3.9(a)], the damage level at the bulk defect peak maximum [Fig. 3.9(b)], and the damage production efficiency [Fig. 3.9(c)], which is defined as the ratio of depth-integrated stable bulk damage (without the contribution from the surface defect peak) to the total number of vacancies (calculated with the TRIM code) ballistically generated by the ion beam in the same region of the crystal. [29] It is seen from Figs. 3.8 and 3.9 that, within experimental error, the accumulation of damage both at the surface and in the bulk (at depths corresponding to R_{pd}s) is independent of the distance of the bulk defect peak from the surface (i.e., the length of the defect generation profile). Hence, the upper bound for L_d is $\sim 50 - 100$ nm. This is in full agreement with above estimates of L_d based on pulsed-ion-beam measurements.

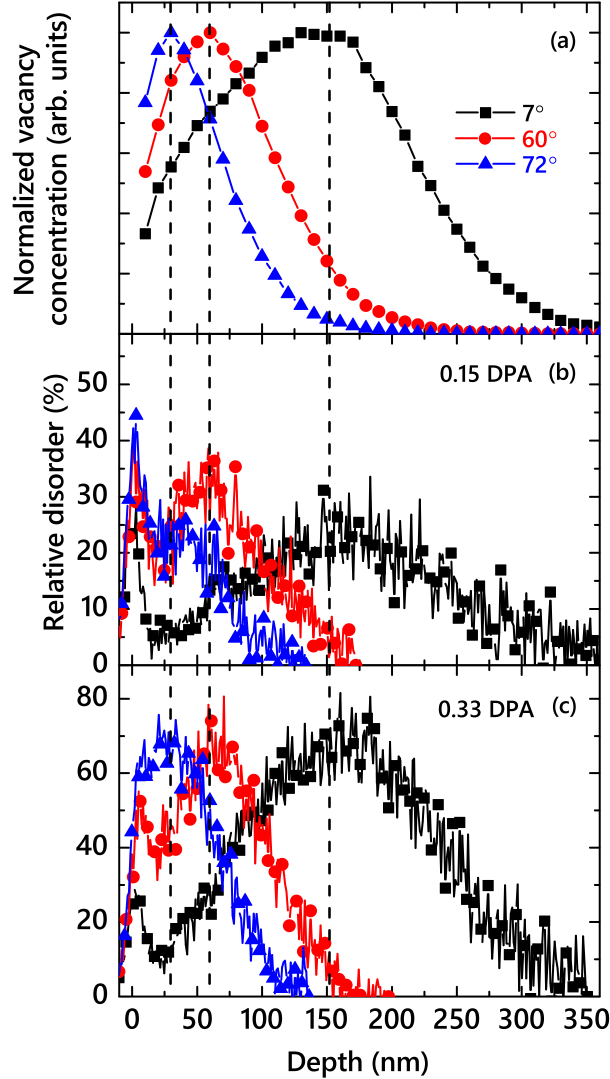

Figure 3.8: (Color online) (a) Normalized depth profiles of lattice vacancies ballistically generated in Si by irradiation with 500 keV Xe ions with different incident beam angles relative to the sample surface normal. Positions of the maxima, R_{pd}, of such profiles are indicated by vertical dash lines (at 30, 60, and 152 nm). (b) and (c) Depth profiles of relative disorder for Si irradiated at room temperature at various angles to ion doses of 0.15 and 0.33 DPA, respectively.

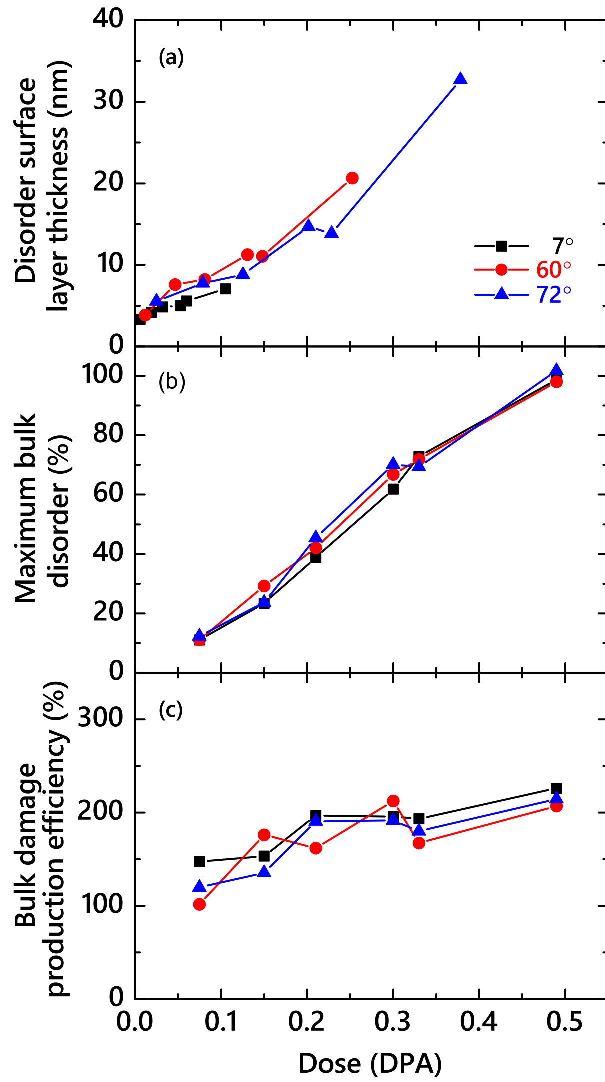

Figure 3.9: (Color online) Ion dose dependencies of (a) the effective thickness of surface amorphous layers, (b) the bulk damage peak maximum, and (c) the damage production efficiency for Si bombarded at room temperature with 500 keV Xe ions for three beam tilt angles.

Values of L_d of $\sim 15-50$ nm (Fig. 3.5 and Table 3.1) are also consistent with several previous estimates of L_d in Si bombarded with ions or electrons at RT [10, 31–34] but are much smaller than a L_d of $\sim 300-2000$ nm estimated in previous measurements of low-dose implanted Si. [35–38] This suggests that the DA processes governing the accumulation of stable defects in the low-dose regime are not the same as the DA processes dominating at the higher dose regime as used in the present study and that are of practical interest for nuclear and electronic materials technologies. Nevertheless, it will be interesting to apply the current pulsed-ion-beam method to study radiation defect dynamics in Si in the low-dose regime.

3.3.4 Choice of pulsing parameters

Finally, the choice of pulsing parameters is discussed (i.e., F_{on}, t_{on}, and t_{off}) for pulsed-ion-beam measurements of τ and L_d. In particular, focus is placed on the selection of F_{on} and t_{on}, which was not discussed in previous brief reports. [12, 13]

3.3.4.1 Choice of pulsing parameters in τ measurements

For the measurement of τ based on $n(t_{off})$ dependencies, it is important that the dynamic annealing efficiency ξ be large enough for the $n(t_{off})$ dependence to be measured by the defect characterization technique of choice. For the present work, with damage measured by RBS/C, ξ should be $\gtrsim 10\%$. Hence, the pulsed-ion-beam method is applicable to irradiation conditions with relatively large ξ. This is hardly a limitation of the pulsed-beam method for studies of radiation damage dynamics since, for cases with low ξ, the contribution of radiation defect dynamics to damage accumulation is also low.

As discussed above, ξ reflects the difference in the level of stable disorder between cases of a continuous beam irradiation with a constant dose rate of F_{on} and irradiation with a pulsed beam when, after the delivery of every pulse with a dose of $F_{on}t_{on}$,

the population of mobile defects is allowed to fully relax (Fig. 3.10). For $t_{on} = t_{on}^{L_d} = \frac{1}{4F_{on}L_d^2}$, [13] on average only one ion impact occurs for every pulse in the area defined by the defect diffusion length (L_d). Hence, for $t_{on} \lesssim t_{on}^{L_d}$, ξ is maximum as it defines the difference in the stable damage level between cases of bombardment with continuous beams with doses rates of $F = F_{on}$ and $F \rightarrow 0$. However, for $t_{on} > t_{on}^{L_d}$, the interaction of defects created in different cascades occurs during and after every pulse even for $t_{off} >> \tau$ since there will be more than one ion impact during each pulse in the L_d-defined area [Fig. 3.10(d)]. A consequence is a reduced ξ.

More importantly, the choice of F_{on} and t_{on} in $n(t_{off})$ studies of τ influences not only the ξ magnitude but also the τ value estimated from the fitting of $n(t_{off})$ curves. For pulsed-ion beam irradiation with $t_{on} \lesssim t_{on}^{L_d}$, due to beam pulsing, the actual average time interval between the arrival of ions to L_d-defined areas (i.e., the effective time of defect relaxation) is not t_{off} but $t_{off}^{effective} = (t_{on} + t_{off})\frac{t_{on}^{L_d}}{t_{on}}$ as illustrated in Fig. 3.10(b) for the case of $t_{on} = \frac{1}{2}t_{on}^{L_d}$. Hence, an analysis of $n(t_{off})$ curves will result in an underestimation of τ for $t_{on} < t_{on}^{L_d}$. For the opposite case of $t_{on} > t_{on}^{L_d}$, ξ is reduced, but the estimation of τ based on $n(t_{off})$ dependencies seems not to be affected since $t_{off}^{effective} = (t_{off} + t_{on}^{L_d})$, as illustrated in Figs. 3.10(c) and 3.10(d). However, for $t_{on} > t_{on}^{L_d}$, the initial concentration of mobile defects at the beginning of the passive portion of each pulse will increase with increasing the number of ion impacts to the L_d-defined area during t_{on}, and the defect decay time τ could depend on such an initial defect concentration. Therefore, for measurements of τ based on $n(t_{off})$ dependencies, $t_{on} \approx t_{on}^{L_d}$ should be chosen in order to maximize the interaction between mobile defects from only two cascades originating from successive pulses.

Figure 3.11(a) shows the dependence of τ, measured by fitting experimental $n(t_{off})$ dependencies with the second order Eq. 3.1, on t_{on} for the case of 500 keV

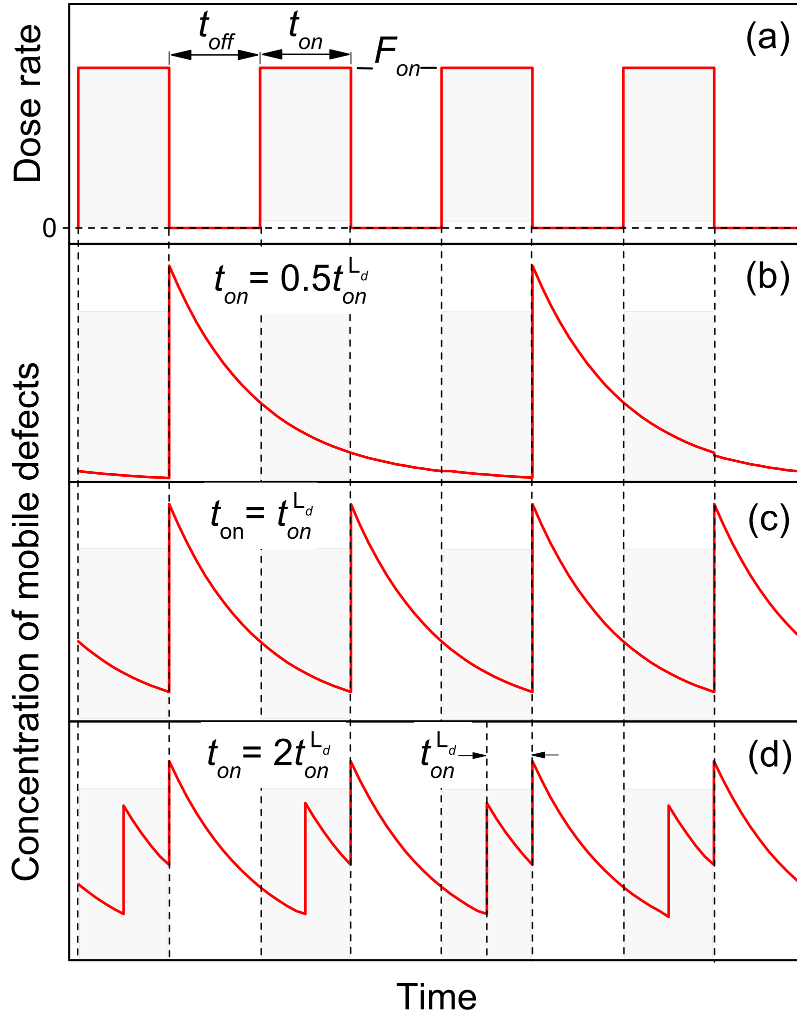

Figure 3.10: (Color online) Schematic of time dependencies of (a) the instantaneous dose rate for pulsed beam irradiation and (b) – (d) the concentration of mobile defects at a given depth in a region of radius L_d for a constant t_{on} and different F_{on} or L_d values resulting in $\frac{t_{on}}{t_{on}^{L_d}}$ of 0.5, 1.0, and 2.0, respectively.

Ar ion irradiation. It reveals that, as expected based on the above arguments, τ increases with increasing t_{on} up to ~ 1 ms and stays constant for $t_{on} \approx t_{on}^{L_d}$ (in the range of $\sim 1-2$ ms). The existence of such a plateau in the $\tau(t_{on})$ dependence can be explained by results of Fig. 3.11(b), showing the fraction of the sample area that has received 0, 1, 2, and 3 ion impacts for the total dose from two interacting pulses each of length t_{on}, with an ion impact area of $4L_d^2$ and $L_d = 28$ nm for Ar (see Sec. 3.3.3). [39] A comparison of Figs. 3.11(a) and 3.11(b) shows that such an "ideal" range of t_{on} (of $\sim 1-2$ ms) in Fig. 3.11(a) corresponds to a damage zone overlap regime between the maxima of curves for 1 and 2 ion impacts in L_d-defined areas. It is also seen from Fig. 3.11 that, for $t_{on} \gtrsim 2$ ms, corresponding to more than 2 ion impacts in the L_d-defined area, the τ value increases sharply. This is consistent with results from Sec. 3.3.2 that τ increases for irradiation regimes with a larger concentration of mobile defects in collision cascades. Interestingly, Fig. 3.11(a) also shows that τ exhibits a saturation stage for $t_{on} \geq 7$ ms. This saturation stage is expected for such a regime with $t_{on} \gg \tau$, when mobile defects generated at the beginning of each pulse decay before the end of the pulse and, hence, are unable to interact with mobile defects generated by ions from the next incoming pulse.

3.3.4.2 Choice of pulsing parameters in L_d measurements

For measurements of L_d based on the onset of the damage increase in $n(t_{on})$ dependencies corresponding to $t_{on}^{L_d}$, the selection of the other two pulsing parameters (F_{on} and t_{off}) is straightforward. As discussed previously, [13] $t_{off} >> \tau$ is chosen in order to suppress the interaction of mobile defects generated in different pulses. In addition, F_{on} should be chosen so that $t_{on}^{Ld} = \frac{1}{4F_{on}L_d^2} \lesssim \tau$. Otherwise, n will be independent of t_{on} as the population of mobile defects will decay between ion impact arrivals to L_d-defined areas since $t_{on}^{L_d}$, by definition, is the average time interval

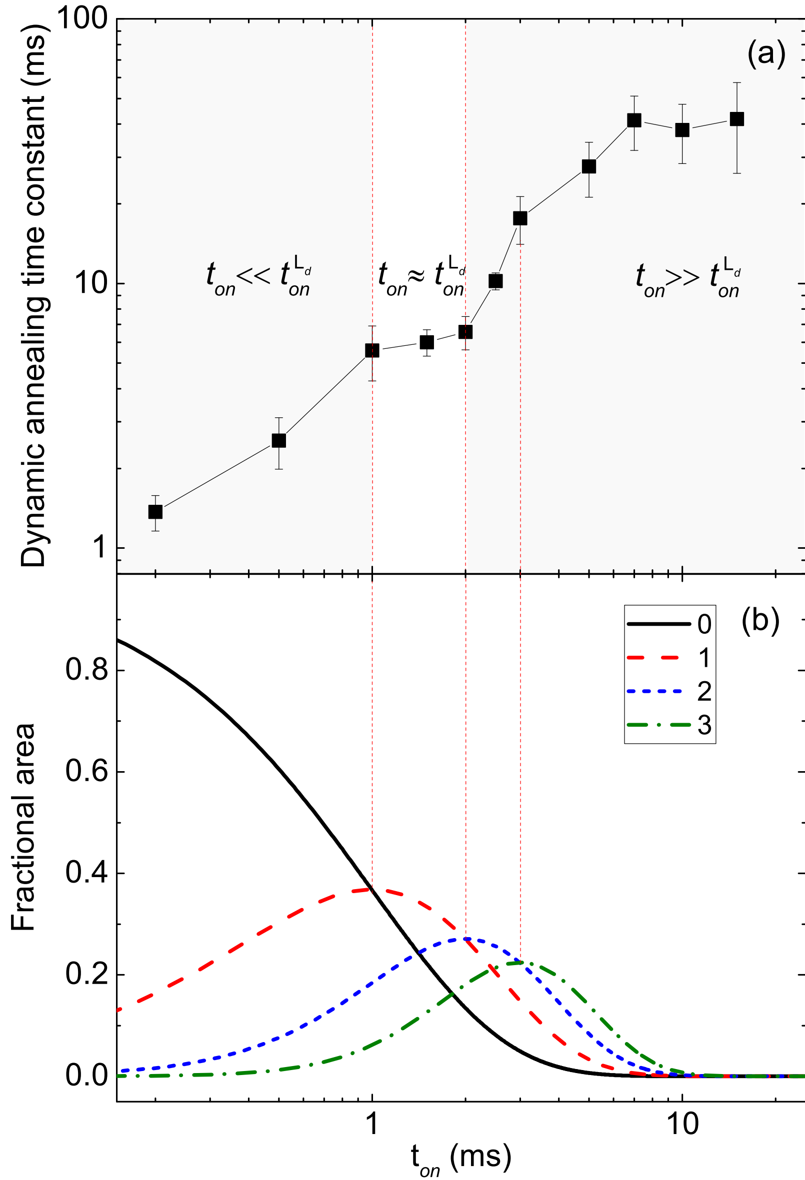

Figure 3.11: (Color online) (a) Dependence of the DA time constant (τ) on t_{on} for FZ-Si bombarded at room temperature with pulsed beams of 500 keV Ar ions with $t_{off} = 100$ ms and $F_{on} = 1.6 \times 10^{13}$ cm^{-2} s^{-1}. (b) The fraction of the sample area that has received 0, 1, 2, and 3 ion impacts for the total dose from two interacting pulses each of length t_{on}, with an ion impact area of $4L_d^2$ and $L_d = 28$ nm for Ar.

between ion impacts in L_d-defined areas during the active portion of the pulse.

3.4 Conclusions

Effects of the collision cascade density, the instantaneous dose rate, the total dose, and the dopant concentration on the parameters of radiation defect dynamics (τ and L_{d}) were studied in Si at room temperature. Results can be summarized as follows.

(i) A second order defect relaxation kinetics has been found for all the cases studied, with a defect relaxation time constant τ in the range of $4 - 13$ ms and a diffusion length L_d of $\sim 15 - 50$ nm at RT.

(ii) Both τ and L_d are essentially independent of the maximum instantaneous dose rate, total ion dose, and dopant concentration within the ranges studied (see Table 3.1). Both τ and L_d, however, increase with increasing ion mass, demonstrating that collision cascade density influences the parameters of radiation defect dynamics in Si.

(iii) This work emphasizes the importance of dynamic annealing effects in ion-irradiated Si and demonstrates the strengths and limitations of the pulsed-ion beam method to assess the defect dynamics.

These results will likely stimulate further studies of defect dynamics in technologically relevant materials. Of particular interest is the understanding of the radiation response of nuclear materials. The pulsed-ion-beam method can be applied for future studies of well-appreciated but still poorly understood [40] effects of the large difference in effective dose rates between ion irradiation in a laboratory and neutron irradiation in a nuclear reactor. Moreover, these results have direct implications for understanding the difference between rastered and broad-beam irradiation, which is a topic of current interest in the nuclear materials community. [40, 41] In ion ir-

radiation experiments with rastered ion beams, unintentional beam pulsing for any given area on the sample occurs. In contrast to the pulsed-ion-beam experiments of the present work, for typical rastered beams, the instantaneous dose rate depends not only on the rastering algorithm but also on the beam shape (focusing), which is difficult to measure and control. This significantly complicates the interpretation of data obtained with rastered ion beams. Finally, since radiation defect dynamics processes are expected to be thermally-activated, section 4 explores the temperature dependence of τ, shedding light on the underlying atomistics of defect interaction.

4. THE ROLE OF FRENKEL DEFECT DIFFUSION IN DYNAMIC ANNEALING IN ION-IRRADIATED SI*

The formation of stable radiation damage in crystalline materials often proceeds via so-called dynamic annealing (DA) processes, involving migration, recombination, and clustering of mobile point defects *during* irradiation. These DA processes are complex and remain poorly understood even for crystalline Si, which is the most extensively studied and arguably best understood material. [42] Since DA is believed to be thermally activated, determining activation energies (E_as) of the dominant DA processes is one of the first logical steps toward understanding radiation damage dynamics. This section focuses on identifying these dominant processes and their activation energies.

Several attempts to understand DA in Si by measuring associated E_as have been reported, albeit with limited success as they have revealed a very wide range of E_as of $\sim 0.2 - 1.7$ eV. [6, 8, 26, 43] For example, Linnros and Holmen [43] have extracted an E_a of 1.2 eV from the temperature (T) dependence of the ion dose rate at which the crystalline/amorphous interface is stationary for bombardment with 1.5 MeV Ne, Ar, or Xe ions in the T range of $\sim 100 - 300$ °C. In contrast, Schultz et al. [6] have found an E_a of 0.9 eV by plotting the T-dependence of the dose rate required to reach amorphization in the crystal bulk at a fixed dose for 1 MeV Si ion irradiation in a narrow T range of $\sim 40 - 80$ °C. Goldberg et al. [8] have expanded the approach of Schultz et al. [6] and found E_as in a wide range of $\sim 0.7 - 1.7$ eV for 80 keV ions with masses ranging from ^{12}C to ^{132}Xe and T in the range of $\sim 10 - 300$ °C. They [8]

* Portions of this work are reprinted from Scientific Reports, Vol 7, J. B. Wallace, L. B. Bayu Aji, A. A. Martin, S. J. Shin, L. Shao, S. O. Kucheyev, "The role of Frenkel defect diffusion in dynamic annealing in ion-irradiated Si", Pages No. 39754, Copyright (2017), under the Creative Commons Attribution 4.0 International License.

have found that the E_a value increases close-to-linearly with either ion mass or T (since, with increasing ion mass, the onset of bulk amorphization occurs at higher Ts for any given dose and dose rate). Finally, Kinomura et al., [26] following the work of Linnros et al., [44] have systematically studied T dependencies of the rate of ion-beam-induced epitaxial crystallization and found E_a values of $\sim 0.3 - 0.4$ eV in the T range of $\sim 250 - 400$ °C for irradiation with 3 MeV C, Si, Ge, or Au ions and an E_a of ~ 0.2 eV for 3 MeV C ion bombardment in the T range of $\sim 150 - 280$ °C. Such large inconsistency in the E_as reported ($\sim 0.2 - 1.7$ eV) highlights the complexity and currently limited understanding of the fundamental physics governing DA even for Si.

In this section, the pulsed ion beam technique is used [45–48] to measure the T dependence of the DA time constant (τ) in Si bombarded with 500 keV Ar ions in a regime of relatively high ion doses when damage accumulation is dominated by inter-cascade DA processes (i.e., by the interaction of mobile defects generated in different collision cascades). Results reveal two well-defined regions in the Arrhenius plot of the DA rate, with very different E_as of 73 and 420 meV, below and above ~ 60 °C, respectively. A comparison of these E_as with the literature values [49–53] and rate theory modeling results suggest that inter-cascade communication in Ar-ion-bombarded Si is carried out primarily by migrating interstitials and vacancies, with vacancy migration and interaction being the rate limiting processes.

4.1 Experimental

The 4 MV ion accelerator (National Electrostatics Corporation, model 4UH) at Lawrence Livermore National Laboratory was used for both ion irradiation and ion beam analysis. Float-zone grown (100) Si single crystals (with a resistivity of ~ 5 Ω cm) were bombarded with 500 keV $^{40}Ar^{+}$ ions at 7° off the [100] direction in the T

range from -20 to 140 °C. To improve thermal contact, the samples were attached to the Cu sample holder with conductive Ag paste. All irradiations were performed in a broad beam mode. [45] In each irradiation run, the total dose was split into a train of equal square pulses each with an instantaneous dose rate $F_{on} \approx 1.9 \times 10^{13}$ cm^{-2} s^{-1} and duration $t_{on} = 1$ ms, corresponding to $\sim 4.6 \times 10^{-5}$ displacements per atom per pulse. The depth profile of ballistically-generated vacancies was calculated with the TRIM code (version SRIM-2013.00) [20] with an atomic concentration of Si of 4.98×10^{22} atoms cm^{-3} and a threshold energy for atomic displacements of 13 eV. The pulsing parameters F_{on} and t_{on} were chosen based on previous pulsed beam measurements of Si at room T [45, 46] in order to maximize the DA efficiency and to limit the inter-cascade defect interaction within each pulse. The adjacent pulses were separated by time t_{off}, which was varied between 0.2 and 50 ms. The inset in Fig. 4.1(a) shows a schematic of the time dependence of the instantaneous dose rate and defines pulsing parameters t_{on}, t_{off}, and F_{on}. A more detailed description of the experimental arrangement can be found elsewhere. [45, 46]

The dependence of lattice damage on t_{off} was studied *ex-situ* at room T by ion channeling. Depth profiles of lattice disorder were measured with 2 MeV $^4He^+$ ions incident along the [100] direction and backscattered into a detector at 164° relative to the incident beam direction. Raw channeling spectra were analyzed with one of the conventional algorithms [18] for extracting depth profiles of relative disorder. Values of average relative bulk disorder (n) were obtained by averaging depth profiles of relative disorder over 20 channels ($\sim$ 38 nm) centered on the bulk damage peak maximum. Error bars of n are standard deviations. Total ion doses at different Ts were different and chosen such that, for continuous beam irradiation (i.e., $t_{off} = 0$), n was in the range of $0.6 - 0.9$ (with $n = 1$ corresponding to full amorphization).

4.2 Results and discussion

Figure 4.1 shows representative depth profiles of relative disorder for bombardment of Si with continuous ($t_{off} = 0$ ms) and pulsed ($t_{off} = 3$ and 30 ms) beams at Ts of 40 and 80 °C. It is seen that, for both Ts, these depth profiles are bimodal, with the first small peak at the sample surface and the second major peak in the crystal bulk. The bulk peak is centered on $\sim$ 500 nm, which corresponds to the maximum of the nuclear energy loss profile for 500 keV Ar ions. [20] It is seen from Fig. 4.1 that the average bulk disorder (n) decreases with increasing t_{off} for both Ts. This is better illustrated in Fig. 4.2, which summarizes all the $n(t_{off})$ dependencies for Ts from -20 to 140 °C. It is seen from Fig. 4.2 that, for all the Ts studied, n monotonically decreases with increasing t_{off}. This effect is due to the interaction of mobile defects generated in different pulses and, hence, in different cascades (i.e., inter-cascade defect interaction).

Decay dependencies, as revealed by Fig. 4.2, are commonly described by either first or second order decay equations in order to estimate decay time constants and, hence, kinetic rates. In a first kinetic order process, the rate is directly proportional to the concentration of interacting species, while in the second order process, the rate is proportional to the square of the concentration. Examples of the first order processes of defect interaction include trapping of interstitials or vacancies at sinks, whereas direct vacancy–interstitial annihilation and the formation of di-vacancies and di-interstitials are examples of the second order processes.

The $n(t_{off})$ dependencies from Fig. 4.2 were fitted via the Marquardt-Levenberg algorithm [54] with first ($n(t_{off}) = n_\infty + (n(0) - n_\infty)\exp(-t_{off}/\tau_1)$) and second order ($n(t_{off}) = n_\infty + \frac{n(0)-n_\infty}{1+\frac{t_{off}}{\tau_2}}$) kinetics equations, represented in Fig. 4.2 by solid and dashed lines, respectively. Here, $\tau_{1,2}$ is the characteristic decay time constant,

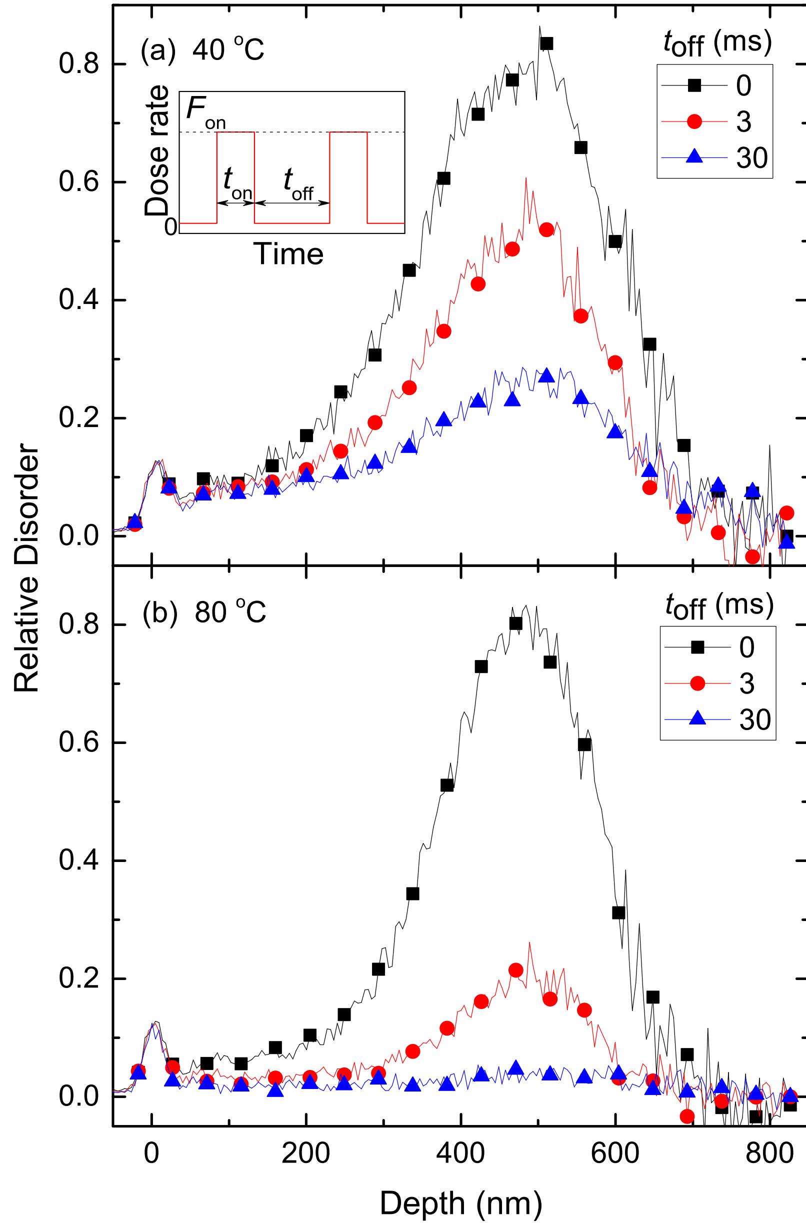

Figure 4.1: (Color online) Selected depth profiles of relative disorder in Si bombarded with a pulsed beam of 500 keV Ar ions with $F_{on} = 1.9 \times 10^{13}$ cm^{-2} s^{-1}, $t_{on} = 1$ ms, and different t_{off} values given in legends at temperatures and doses of (a) 40 °C and 2.7×10^{14} cm^{-2} and (b) 80 ° C and 5.0×10^{14} cm^{-2}. For clarity, only every 10th experimental point is depicted. The inset in (a) is a schematic of the time dependence of the instantaneous dose rate for pulsed beam irradiation, defining t_{on}, t_{off}, and F_{on}.

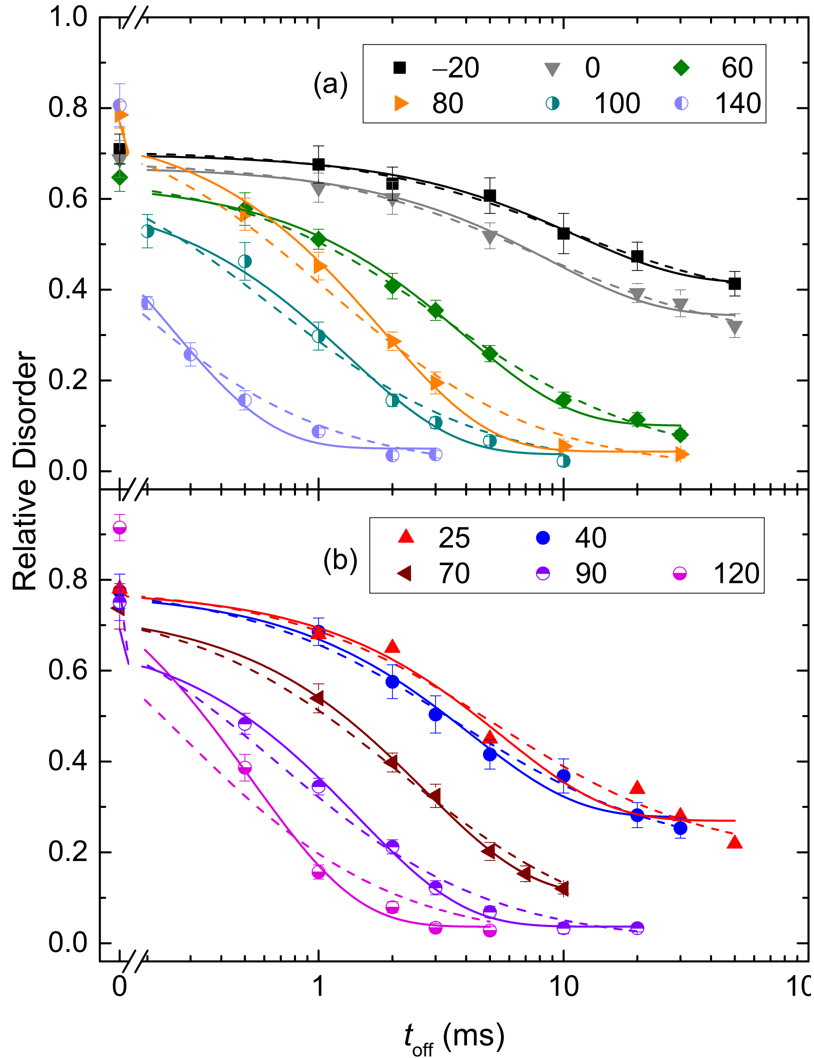

Figure 4.2: (Color online) Average relative bulk disorder in Si bombarded at different temperatures (given in legends in units of °C) with a pulsed beam of 500 keV Ar ions with $F_{on} = 1.9 \times 10^{13}$ cm^{-2} s^{-1} and $t_{on} = 1$ ms as a function of the passive portion of the beam duty cycle (t_{off}). Results of fitting the data with the first and second order decay equations are shown by solid and dashed lines, respectively. Results are separated into panels for clarity.

and n_∞ is relative disorder for $t_{off} >> \tau_{1,2}$. Since a decrease in n with increasing t_{off} is a result of inter-cascade defect interaction, the time constant τ reflects inter-cascade defect interaction processes. Below 60 °C, the data is fitted best with the second order decay equation, while the first order decay gives a better fit for all the $n(t_{off})$ dependencies above 60 °C. Such an evaluation of the kinetic order of $n(t_{off})$ dependencies was done by comparing R-squared values of fits with the first and second order decay equations. In all the cases of different Ts, however, R-squared values were > 0.96.

Temperature dependencies of τ_1 and τ_2 are plotted in Fig. 4.3, revealing a monotonic decrease with increasing T and a kink (i.e., a change in the first derivative) at 60 °C in both curves. As expected from the form of first and second order decay equations, $\tau_1 > \tau_2$. Also plotted in Fig. 4.3 is the T dependence of the DA efficiency $\xi_{1,2}$: [45, 46] $\xi = (n(0) - n_\infty)/n(0)$. Figure 4.3 shows that, within experimental errors, ξ increases with T, reflecting a corresponding decrease in n_∞, which is also clearly seen in $n(t_{off})$ dependencies of Fig. 4.2. Above $\sim$ 60 °C, ξ_1 saturates at $\sim$ 90%. Note that the apparent saturation of ξ_2 at 100% for higher Ts is an artifact of inferior fitting with the second order decay equation above 60 °C.

In Fig. 4.4, $\tau_{1,2}(T)$ dependencies are replotted from Fig. 4.3 in Arrhenius coordinates, with the DA rates ($k_{1,2}$) defined as $k_1 = \frac{1}{\tau_1}$ and $k_2 = \frac{1}{\tau_2(n(0)-n_\infty)}$ for the first and second order decay processes, respectively, and with kT having the usual meaning. Two Arrhenius regimes are clearly seen in Fig. 4.4, below and above 60 °C. Fitting of the data to $k_{1,2} = A_{1,2}\exp(-\frac{E_{a1,2}}{k_bT})$ gives E_as and pre-exponential factors ($A_{1,2}$) of $E_{a2} = 73 \pm 5$ meV and $A_2 = (6.1 \pm 1.3) \times 10^3$ Hz for $T < 60$ °C and $E_{a1} = 420 \pm 10$ meV and $A_1 = (1.43 \pm 0.69) \times 10^9$ Hz for $T > 60$ °C. Values of E_as obtained by fitting with the first and second order decay equations are comparable. Indeed, fitting data from Fig. 4.4 with the first order decay equation for $T < 60$

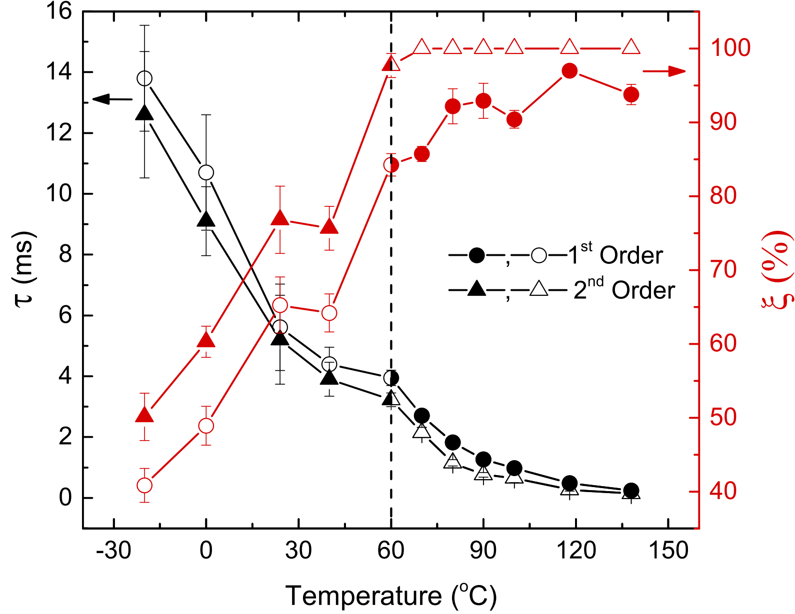

Figure 4.3: (Color online) Temperature dependencies of the effective time constant of DA (τ, the left axis) and the DA efficiency (ξ, the right axis) for fitting with the first (circles) and second (triangles) order decay equations. Solid symbols represent the best fit to the data.

°C and with the second order decay equation for $T > 60$ °C gives E_as and As of $E_{a1} = 110 \pm 10$ meV and $A_1 = (15.3 \pm 5.4) \times 10^3$ Hz for $T < 60$ °C and $E_{a2} = 440 \pm 20$ meV and $A_2 = (4.05 \pm 2.9) \times 10^9$ Hz for $T > 60$ °C.

The experimental data herein unambiguously reveals the existence of two distinct dominant DA process at Ts below and above 60 °C, evidenced by (i) the presence of two well-defined Arrhenius regions with vastly different E_as and As (Fig. 4.4), (ii) a saturation of ξ for $T > 60$ °C (Fig. 4.3), and (iii) the change from the second order to the first order kinetic behavior. The switch from the second kinetic order to the first order behavior at 60 °C points to a change in the dynamics of defect interaction. The Raman scattering measurements (with 633 nm laser light) of samples irradiated at different Ts, however, have not revealed any evidence of the change in the damage

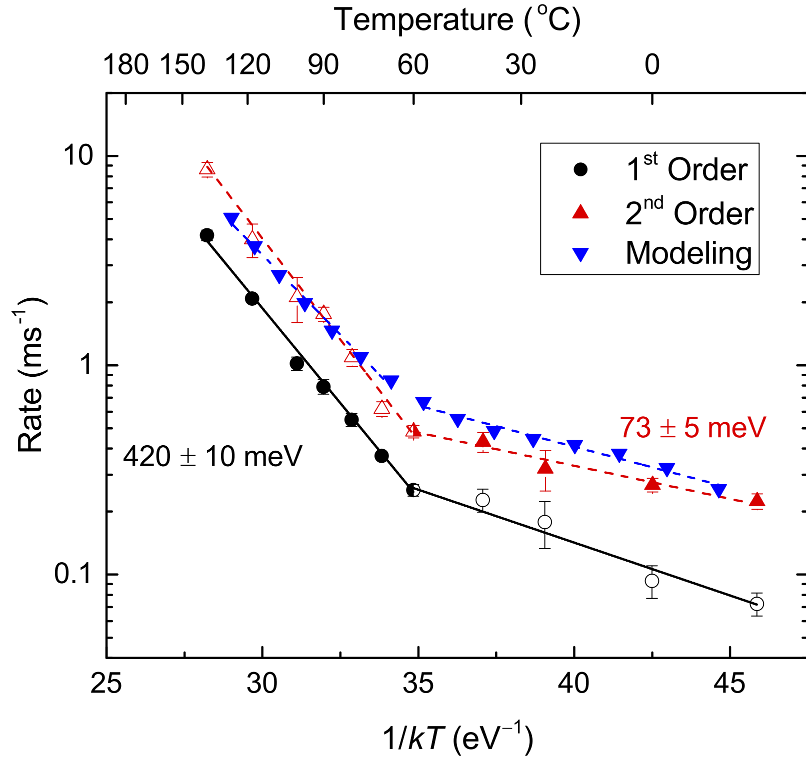

Figure 4.4: (Color online) Arrhenius plot of the DA rate. Solid symbols are results of the best fit to experimental $n(t_{off})$ dependencies, which is the second order decay below 60 °C and the first order decay above 60 °C. Straight lines show results of linear fitting, revealing activation energies of 420 meV and 73 meV above and below 60 °C, respectively. Results of rate theory modeling, described in the text, are also shown.

state at 60 °C. In addition, transmission electron microscopy analysis has not revealed any differences in the type of damage in Si irradiated with pulsed and continuous beams to the same disorder level.

The two E_as of $\sim$ 73 and $\sim$ 420 meV (Fig. 4.4) are in contrast to much larger E_a values of $\sim 0.7 - 1.7$ eV reported in previous dose rate studies. [6, 8, 43] In most of these prior attempts to measure the E_a of DA, [6, 8, 43] the dose rate was used as the rate of the kinetic process in the Arrhenius relationship, with the implicit assumption that the dose rate is proportional to the rate of the dominant DA process. The large

difference between the E_a values measured in the present work and those in previous dose rate studies [6, 8, 43] could be attributed to the fact that, in the dose rate approach, the E_a is effectively extracted from the $\xi(T)$ dependence. As discussed in detail recently, [46] for the choice of F_{on} and t_{on}, ξ is the magnitude of the dose rate effect; i.e., the difference between n for continuous beam irradiation with dose rates of $F = F_{on}$ and $F \to 0$. Hence, ξ reflects the fraction of ballistically-generated Frenkel defects that participate in DA processes for any given F_{on} rather than the *rate* of defect interaction. In other words, while τ reflects the DA rate (i.e., dynamics), ξ describes the DA "magnitude". This is further supported by Fig. 4.3, revealing qualitatively different $\xi(T)$ and $\tau(T)$ dependencies, indicating that parameters ξ and τ provide complementary information.

With such a large spread in the E_a values reported previously, [6, 8, 26, 43] the dominant DA processes in Si have remained elusive, with suggestions that the mobile defects in the high-dose regime dominated by inter-cascade DA processes behave differently from the migration of vacancies and interstitials in the low-dose regime of intra-cascade DA effects, commonly monitored by electron paramagnetic resonance (EPR), [49] positron annihilation spectroscopy (PAS), [50] and deep level transient spectroscopy (DLTS). [53] In contrast, these results strongly suggest that, even at relatively high doses and dose rates typical for technologically relevant radiation environments, point defect migration still plays a key role in inter-cascade DA. Note that an E_a of $\sim$ 73 meV for $T <$ 60 °C agrees with E_as previously associated with the migration of isolated interstitials in Si revealed in DLTS [53] and PAS [50] measurements. Similarly, an E_a of 420 meV for $T >$ 60 °C agrees with E_as assigned to the migration of neutral vacancies ($\sim 0.40 - 0.46$ eV) reported in EPR, [49] PAS, [50] and Raman spectroscopy [51] measurements. It is also consistent with several theoretical predictions. [55–59] It should be noted that charge states of mobile defects

are important for low dose irradiation conditions when lattice dopants determine the position of the Fermi level and the defect charge state. In contrast, the present study focuses on the regime of relatively high doses (and, hence, high damage levels) when likely only neutral vacancies and interstitials play a role. Indeed, in the present study, the concentration of radiation-generated (stable) lattice defects largely exceeds the initial dopant concentration, and the material is in a semi-insulating state. [46] This conclusion is further supported by a recent pulsed beam study which showed τ to be independent of the doping level for 500 keV Ar ion irradiation of Si at RT. [46]

The dominant role of defect migration in inter-cascade DA is also consistent with a relatively large average separation between the centers of adjacent cascades in every pulse ($\sim$ 72 nm or $\sim$ 300 atomic spacings). In such cases, inter-cascade defect interaction could not proceed without significant defect migration. For a three-dimensional random walk with a defect moving only a single atomic spacing during each jump, $\sim 200,000$ jumps would be necessary for the defect to travel the distance between the centers of two adjacent collision cascades. [60] Hence, while the E_a of defect migration may not be the largest energy barrier a defect on the path to recombination or trapping must overcome, it is a barrier which must be overcome numerous times.

4.3 Modeling

To get insight into the atomistics of defect interaction and to better correlate the E_as measured here with energetic barriers of specific defect migration or interaction processes, rate theory modeling is implemented and [61–64] bench-marked against the experimental data. A successful description of both $n(t_{off})$ and $\tau(T)$ dependencies has been obtained with a model considering only the following four processes: (i) ballistic Frenkel pair generation (Is and Vs), calculated with the TRIM code; [20] (ii)

the annihilation of Is and Vs at unsaturating sinks (such as point defect clusters), (iii) $V + V \rightarrow V_2$, and (iv) $I + V_2 \rightarrow V$. Here, I, V, and V_2 refer to interstitials, vacancies, and divacancies, respectively. The $V + I \rightarrow \emptyset$ reaction is omitted since it does not affect the balance between V and I, which is critical for stable damage accumulation within this model. In addition, adding the $V + I \rightarrow \emptyset$ reaction to the model has no effect on the resultant E_a values. The equations for T-dependent interaction parameters were taken from Titov et al. [64]. Migration energies of Vs and Is were set to 400 and 100 meV, respectively, while all other energetic barriers were set to zero. All capture radii were set to 5λ, where λ is the atomic spacing in Si. The total dose and the dose rate were set to 10^{12} cm^{-2} and 10^{13} cm^{-2}s^{-1}, respectively, with a t_{on} of 1 ms. The attempt frequency and the sink concentration were set to 10^{-11} s^{-1} and 8.5×10^{16} cm^3, respectively, and the bulk disorder (n) was represented by the V_2 concentration, as in previous studies. [61–64]

Results of such rate theory modeling are shown in Fig. 4.4, along with linear fits (dashed lines) to determine E_as. It is remarkable that, such a relatively simple model is capable of reproducing a rather complex experimental data: $n(t_{off})$ dependencies and the Arrhenius behavior of the DA rate. Within this model, an E_a of $\sim$ 400 meV in the Arrhenius plot of Fig. 4.4 for $T >$ 60 °C indeed corresponds to the V migration energy. However, an E_a of $\sim$ 100 meV for $T <$ 60 °C in Fig. 4.4 actually does not correspond to the I migration energy. Instead, it reflects a competition between the two channels for V annihilation, one by trapping at sinks and the other via the formation of V_2. While V_2 formation dominates at lower Ts, V annihilation at sinks becomes the rate limiting process at $T >$ 60 °C. The much lower E_a for I migration results in an I migration rate that is orders of magnitude faster than that of Vs. As a result, τ is controlled predominantly by the V migration rate in the entire T range studied. Hence, modeling also helps us understand the origin of the

critical T of 60 °C in Fig. 4.4.

However, this relatively simple model has limitations. It takes into account only a very limited subset of possible defect interactions and ignores possible contributions from interstitial clusters and larger vacancy clusters. This simple model cannot quantitatively describe the full range of the damage buildup up to lattice amorphization as it does not take into account the non-linear processes leading to a super-linear (sigmoidal) damage accumulation at elevated Ts. This model also does not include nonlinear cascade density effects leading to the formation of thermal and/or displacement spikes. [25] In addition, this model does not predict the switch from the 2nd to the 1st order kinetic behavior at 60 °C. More work is currently needed for the development of more sophisticated and physically realistic models that can describe the entire range of experimental observations, including the damage buildup and defect interaction dynamics under different irradiation conditions. Future experimental work is also needed to study non-linear spike effects on the temperature dependence of defect interaction dynamics in Si.

4.4 Conclusion

In conclusion, the pulsed beam technique was used to measure the T-dependence of the effective time constant of DA in Si bombarded in the T range from −20 to 140 °C with 500 keV Ar ions. Results have revealed two well-defined Arrhenius regimes described by activation energies of $\sim$ 73 and $\sim$ 420 meV, below and above 60 °C, respectively. A comparison of experimental data with rate theory modeling results suggests that inter-cascade DA in Si proceeds via interstitial and vacancy migration, and the DA rate is limited by processes of vacancy annihilation at sinks and divacancy formation. These results could have far reaching implications for future studies of radiation defect dynamics as the pulsed-beam method offers a novel way of

measuring DA rates and activation energies that could be directly compared with results of predictive modeling. Importantly, this method can be used to measure defect interaction rates under technologically relevant irradiation conditions of pronounced inter-cascade defect interaction in any material, opening the door to studying intricate defect interaction phenomena in materials with the composition across the periodic table.

5. CASCADE DENSITY EFFECTS ON DEFECT DYNAMICS

Section 3 demonstrated the dependence of ion mass on the defect lifetime and diffusion length in Si at room temperature. With increasing ion mass or increasing target mass, the cross section for elastic collision increases, hence leading to a higher density of displacements. Although Section 3 showed the dependence on ion mass, the correlation to cascade density was missing. The objective of this Section is to describe the effects of cascade density on the dynamic annealing behavior in Si. Cascade density is inherently difficult to define since such densities are dependent on the chosen averaging volume around a cascade. Section 5.1 lays the groundwork for discussing cascade density by deriving a fractal model of collision cascades to describe the defect diffusion length in Si and SiC. Section 5.2 studies the dependence of the defect lifetime and interaction processes of dynamic annealing on ion mass across a range of temperatures, making use of the fractal model as well. Finally, Section 5.3 unifies the concepts of ion cascade density (density of defects within a cascade) and flux effects (density of cascades within a material) in the concept of *super-cascade density* in order to describe the dynamic annealing behavior as a function of pulse duration in Si.

5.1 Defect diffusion in pulsed ion irradiated solids – a fractal approach

5.1.1 Introduction

Energetic ions propagating through a crystalline material can transfer their kinetic energy through collisions with nuclei of the target. These target atoms can then collide with other atoms, creating subsequent generations of recoiled atoms. The cumulative result of successive generations of collisional processes, is the formation of a ballistic cascade of point defects. [1] These defects are often highly mobile

and can interact through dynamic annealing processes, involving recombination and clustering. [1, 3–10] Previous studies have shown that the formation of stable lattice disorder can depend strongly on the bombarding ion mass and energy. [1] With increasing ion or target mass, the cross section for elastic scattering increases, leading to higher cascade density. [25, 65] However, the understanding of such effects on dynamic annealing is limited, even for Si which is arguably the simplest and most extensively studied material. [1]

The lack of understanding arises partially from the complex nature of ion collision cascades. Indeed, even defining *cascade density* is not straightforward since the density of defects is strongly dependent on the chosen averaging volume around the cascade. However, great progress was made toward describing cascade density, by Cheng et al. [66] and Winterbon et al. [67] when they showed that the distribution of defects within a collision cascade could be described within the framework of fractal geometry. [68] Rossi et al. [69] further advanced the understanding by showing that as the cascade evolves, the fractal dimensionality increases. Yet despite decades of research showing the clear effect of ion mass on dynamic annealing in Si and SiC, no studies have linked the fractal behavior of collision cascades to experimental results of radiation defect dynamics.

In this paper we have paired our pulsed ion beam method [15, 45–48, 70] for determining the characteristic diffusion length of defects with a fractal model for collision cascade damage production. We demonstrate this technique on $3C-$SiC, which is a technologically relevant material for both it's electronic and nuclear applications. [71, 72] These experiments were carried out at 100 $°C$ under bombardment with 500 keV Ne, Ar, Kr, and Xe ions. In addition data for Si [46] and $3C-$SiC [70] have been re-analyzed with the fractal model developed herein. Our results show that for $3C-$SiC at 100 $°C$ the diffusion length decreases weakly and is in the range

from $\sim 5-15$ nm. For $3C-$SiC irradiated in the T range of $\sim 25-200\ °C$ with 500 keV Ar, the diffusion length increases weakly from $\sim 4-6$ nm. In Si irradiated at RT by 500 keV Ne, Ar, Kr, and Xe ions, the diffusion length is shown to decrease with increasing ion mass from $\sim 40-20$ nm.

5.1.2 Experimental

Single-crystal epilayers of (001) $3C$-SiC epitaxially grown on 3-inch-diameter Si substrates at NOVASiC were used for this study. The epilayers had a thickness of $\gtrsim 2$ μm. The crystal quality of as-received films was verified by measuring a minimum 2 MeV He ion channeling yield of $\sim 1.5\%$, consistent across the wafer. As-received wafers were cleaved to $\sim 5 \times 40$ mm^2 sample strips. To improve thermal contact, the strips were attached to a Cu sample holder with silver paste. Temperature was measured by two thermocouples thermally anchored (with silver paste) to the sample holder at the opposite ends of the sample strips. Ion-beam heating effects were negligible ($\lesssim 0.1$ °C) for the irradiation conditions used in this experiment. The temperature of the sample holder, measured by the two thermocouples, increased by ~ 0.2 °C for the longest irradiation run with a continuous ion beam (i.e., the case with the maximum heat load).

Samples were bombarded with pulsed beams of 500 keV 500 keV ^{20}Ne, ^{40}Ar, ^{84}Kr, or ^{129}Xe ions at 7° off the [100] direction to minimize channeling. All irradiation experiments were performed in a broad beam mode (rather than a beam raster mode). [45] In each irradiation run, the total ion dose (Φ) was split into a train of equal square pulses. Each pulse had the same instantaneous dose rate (F_{on}) of 2.5×10^{13} cm^{-2} s^{-1} and duration (t_{on}), and was separated from the subsequent pulse by t_{off}. The inset in Fig. 5.1(a) shows a schematic of the time dependence of the instantaneous dose rate and defines pulsing parameters t_{on}, t_{off}, and F_{on}. In

these experiments, we kept t_{off} fixed in the range of 50 ms, which, as demonstrated previously, was much greater than the defect relaxation time constants τ. With F_{on}, t_{on}, Φ kept fixed, a series of samples was irradiated with different t_{on} varied between 0.3 and 30 ms. The total ion doses at different Ts were different and chosen such that, for continuous beam irradiation (i.e., $t_{off} = 0$), the level of average relative bulk disorder (n), measured by ion channeling, was in the range of $0.6 - 0.9$ (with $n = 1$ corresponding to full amorphization).

The dependence of stable lattice damage on t_{on} was studied *ex-situ* at room temperature by ion channeling. Depth profiles of lattice disorder in the Si sublattice were measured with 2 MeV $^4He^+$ ions incident along the [100] direction and backscattered into a detector at 164° relative to the incident beam direction. Raw channeling spectra were analyzed with one of the conventional algorithms [18] for extracting depth profiles of relative disorder. Values of n were obtained by averaging depth profiles of relative disorder over 10 channels ($\sim$ 25 nm) centered on the bulk damage peak maximum. Error bars of n are standard deviations. The 4 MV ion accelerator (National Electrostatics Corporation, model 4UH) at Lawrence Livermore National Laboratory was used for both ion irradiation and ion beam analysis. A more detailed description of the experimental arrangement can be found elsewhere. [45, 46]

5.1.3 Modeling

Depth profiles and three-dimensional distributions of ballistically-generated lattice vacancies were calculated with the TRIM code (version SRIM-2013.00, full cascade calculations) [20] with an atomic concentration of SiC and Si of 9.64×10^{22} atoms cm^{-3} (Ref. [71]) 5.0×10^{22} atoms cm^{-3}. The threshold energies for atomic displacement in SiC were 20 and 35 eV for C and Si sublattices, [73] respectively, and 15 eV for Si.

Cascade densities ($\rho_{cascade}$s) at R_{pd}s were calculated based on the algorithm similar to that proposed by Heinisch and Singh. [74] We define the $\rho_{cascade}$ as the average local density of lattice vacancies within individual cascades with an averaging radius of 10 nm. Such an averaging radius was chosen to be comparable with our recent estimates of the L_d in 3C-SiC. [75] Values of $\rho_{cascade}$ were obtained by averaging over $\gtrsim$ 600 individual cascades.

Ion cascade vacancy concentrations were found to scale with increasing R_c according to the standard definition of a fractal [68]

$$N_V = k_\circ \left(\frac{R_c}{a_\circ}\right)^D, \tag{5.1}$$

where N_V is the number of vacancies within R_c radius of a vacancy, $k_\circ$ is the structure prefactor, $a_\circ$ is the Bohr radius used to normalize R_c, and D is the fractal dimension. The cascade density is obtained by dividing $N_V(R_c)$ by the volume of the sphere with radius R_c.

5.1.4 Results and discussion

Figure 5.1(a) shows representative depth profiles of relative disorder in the Si sublattice of SiC for Ne, Ar, Kr, or Xe ion bombardment at 100 °C. For all irradiations, damage peaks are bimodal, with the first small peak at the sample surface and the second major peak in the crystal bulk. The crystal bulk peaks correspond approximately to the depth of maximum nuclear energy loss (R_{pd}) for each ion. The inset in Fig. 5.1(a) shows a schematic of the time dependence of the instantaneous flux for pulsed ion beam measurements, defining F_{on}, t_{on}, and t_{off}. Figure 5.1(b) shows TRIM-code calculated depth profiles of lattice vacancies ballistically generated in Si by 500 keV Ne, Ar, Kr, and Xe ions. As expected all profiles exhibit unimodal Guassian-like distributions with maximum also at the R_{pd}s. Figure 5.1(c)

shows the TRIM-code calculated depth profiles of ion concentration. Maximum ion concentrations occur just beyond the R_{pd} as expected.

Figure 5.1(d) shows the cascade density at $R_c = 10$ nm as a function of depth in SiC bombarded with 500 keV Ne, Ar, Kr, or Xe ions. The $R_c = 10$ nm was chosen based on previous experiments in SiC [70] which showed a diffusion length of ~ 10. The peak of the cascade density is shown to occur deeper into the material than either the maximum of the vacancy or ion concentration profile. This finding could explain previous studies which showed a change in depth of the bulk relative disorder peak with increasing temperature. [76] Such a conclusion would suggest that cascade density effects in $3C-$SiC increase with increasing temperature.

Figure 5.2 shows the average number of vacancies at the depth of maximum nuclear energy loss within a sphere of radius R_c centered on a vacancy for 500 keV Ne, Ar, Kr, and Xe ion cascades into SiC. When plotted on a log-log scale the vacancy number scales linearly as a function of R_c for all ion masses, indicating the fractal nature of collision cascades. The range over which the density scales linearly depends on the ion mass and energy. Thus to maintain linearity, we fit the data in the range of $R_c = 1 - 10$ nm and obtain D and k_o as described in Eq. 5.1.

Cascade densities and fractal parameters were calculated at the R_{pd} for 500 keV ion collision cascades into $3C-$SiC as a function of ion mass ranging from ^{4}He $-$ ^{238}U. Figure 5.3(a) shows the cascade density evaluated at $R_c = 10$ nm. An $R_c = 10$ nm was chosen based on previous experiments in $3C-$SiC which estimated a characteristic dynamic annealing diffusion length of 10 nm. [70] The cascade density is shown to increase monotonically with increasing ion mass, as expected. [25] Furthermore, the cascade density shows two linear regimes with different slopes which intersect just below Ne. Figure 5.3(b) shows the fractal dimension (right axis) and $k_\circ$ (left axis) as a function of R_c. The fractal dimension is shown to increase with increasing

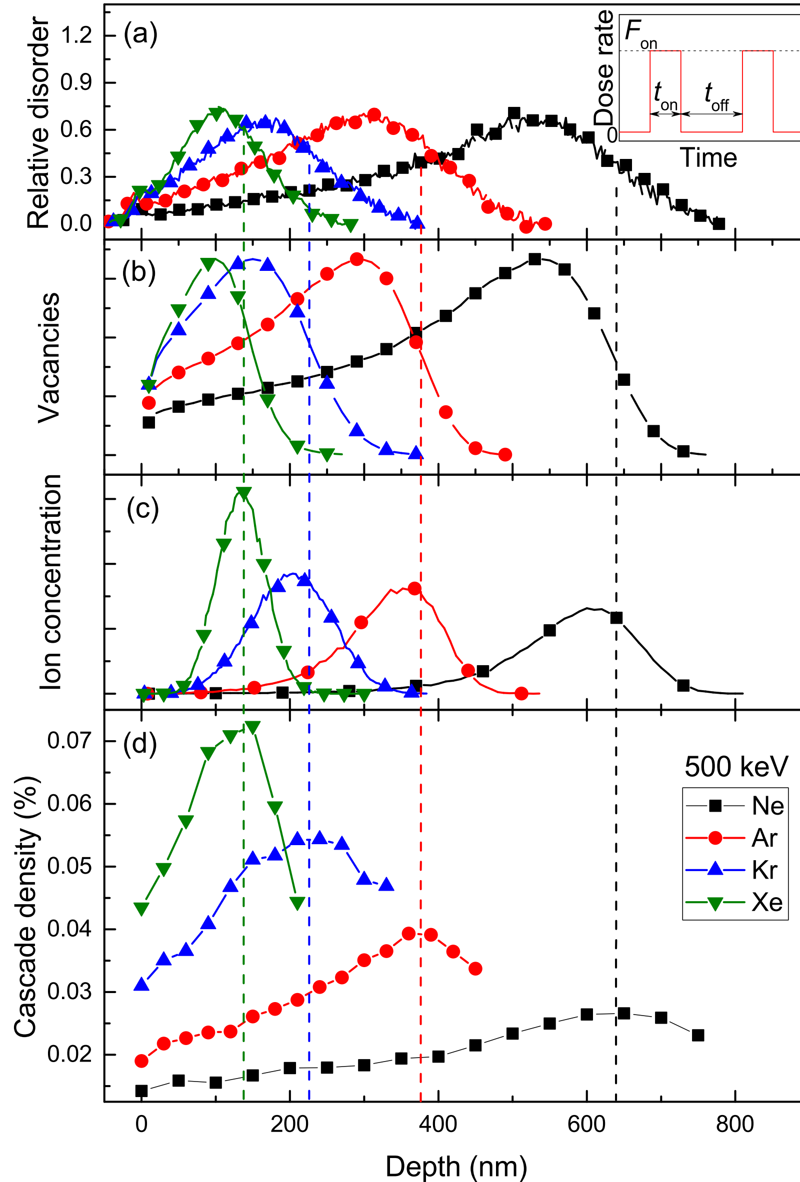

Figure 5.1: (Color online) (a) Selected depth profiles (measured by ion channeling) of the relative disorder in the Si sublattice of SiC bombarded with 500 keV Ne, Ar, Kr, and Xe ions at 100 °C. (b) Normalized TRIM code predicted profiles of the concentration of vacancies and (c) implanted atoms for 500 keV Ne, Ar, Kr, and Xe ion irradiation of SiC. (d) Cascade density as a function of depth from TRIM simulated ion cascades in SiC evaluated with R_c = 10 nm. The inset in (a) shows the time dependence of the instantaneous flux for pulsed beam irradiation, defining F_{on}, t_{on}, and t_{off}.

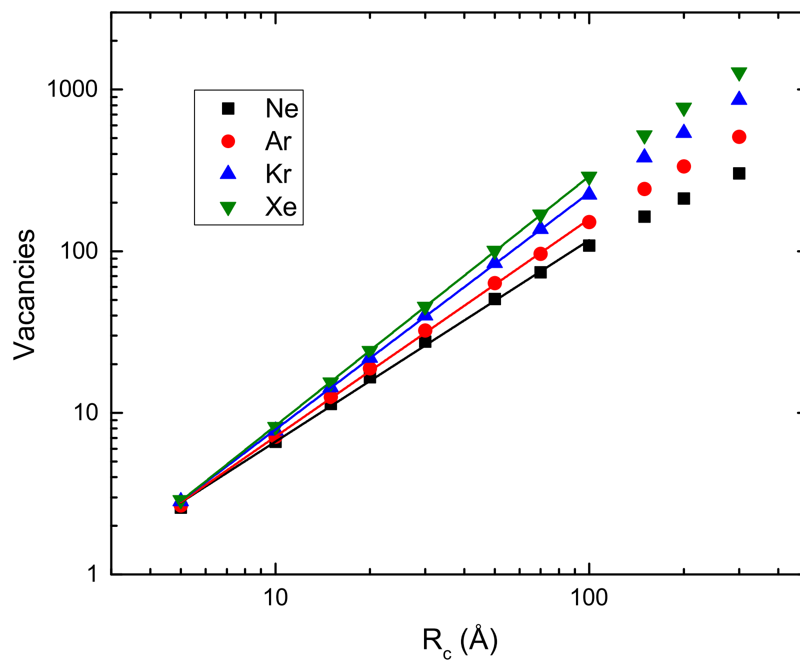

Figure 5.2: (Color online) Averaged number of vacancies within R_c of a vacancy for TRIM simulated 500 keV Ne, Ar, Kr, and Xe ion cascades in SiC at the depth of the maximum nuclear energy loss (R_{pd}). Solid lines are linear fits used to determine fractal dimension and structure factor.

ion mass, whereas the $k_\circ$ is shown to decrease. These findings are in agreement with previous studies of the fractal dimension. [69] Both D and $k_\circ$ show a similar change in linearity at $\sim$ Ne.

In order to link the fractal description of collision cascades with experimental pulsed ion beam measurements, the cascade density (ρ) dependence of damage formation efficiency (ϵ) must be assumed. Here we define ϵ as the relative disorder per DPA. Previous studies in Si [25, 65, 77, 78], Ge [65], GaN [28] and $3C-$SiC [79] have shown that ϵ increases with increasing ρ. If, for low t_{on} values, the efficiency of the stable damage formation scales with the cascade density, $\epsilon \propto \rho$. The cascade density around a vacancy increases with fluence according to $\rho = \rho_\circ(R_c) + g\phi_{pulse}$ where $\rho_\circ(R_c)$ is the fractal cascade density of an isolated ion cascade, g is the TRIM calculated defect concentration, and ϕ_{pulse} is the fluence per pulse defined by $\phi_{pulse} = F_{on}t_{on}$ where F_{on} and t_{on} are defined in the inset of Fig. 5.1(a). The defect formation efficiency is then,

$$\epsilon = n_d/\Phi_{tot} = A\left(\frac{3k_\circ R_c^{D-3}}{4\pi} + g\phi_{pulse}\right). \tag{5.2}$$

Figure 5.4 shows the relative disorder as a function of the fluence per pulse from 500 keV Ne, Ar, Kr, or Xe bombardment of (a) $3C-$SiC at 100 $°C$ and (b) Si at RT. The relative disorder for each ion species increases sub-linearly with increasing fluence per pulse. Solid lines in Fig. 5.4 are results of fitting the data to Eq. 5.2 (R_c and A) for $t_{on} << t_{on}^{ld}$ with fractal parameters from Fig. 5.3.

The resulting R_c values from fitting the data in Fig. 5.4 are shown in Fig. 5.5. The R_c values are the characteristic radius for defect diffusion around a vacancy or equivalently the defect diffusion length ($L_d^{fractal}$). For $3C-$SiC, $L_d^{fractal}$ is in the range from $\sim$ 5 to 15 nm and appears to decrease weakly with increasing ion mass. Similarly, $L_d^{fractal}$ for Si decreases monotonically from $\sim$ 40 to 20 nm with increasing

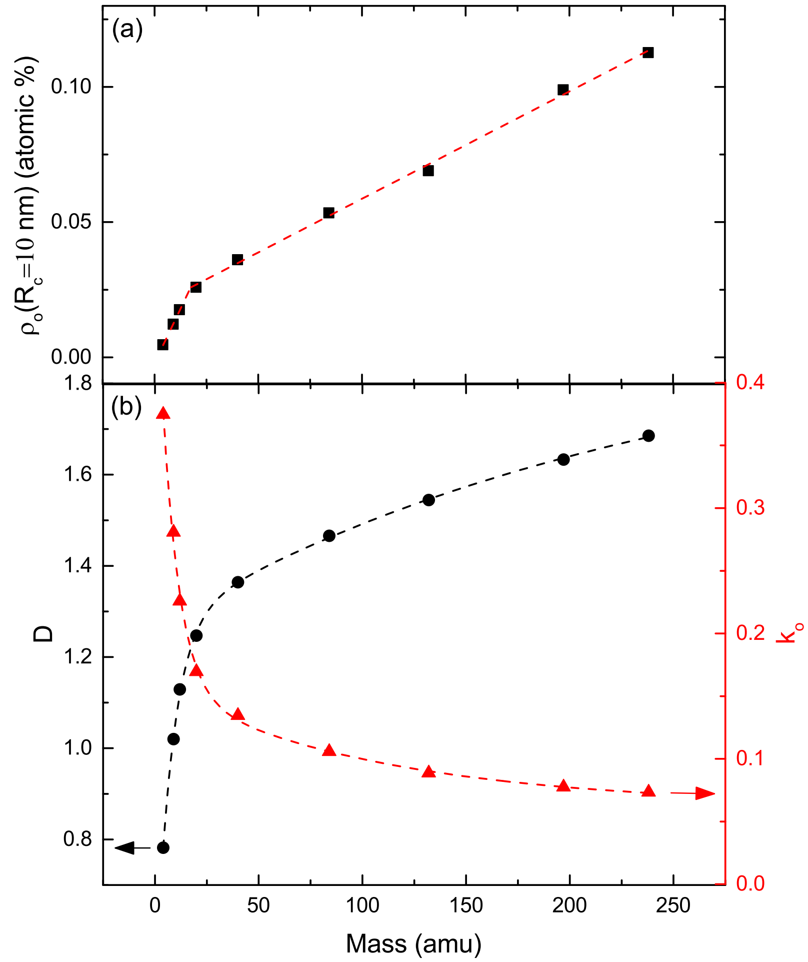

Figure 5.3: (Color online) Cascade density (a), fractal dimension (left axis (b)), and fractal structure factor $k_\circ$ (right axis, (b)) as a function of ion mass for TRIM simulated 500 keV ion cascades in SiC. Cascade density and fractal parameters were evaluated at the depth of the maximum nuclear energy loss (R_{pd}) and $R_c = 10$ nm. Dashed lines are to guide the eye.

ion mass from Ne to Xe. The previous estimate of L_d from this Si data, which used a cylindrical model of a cascade, showed L_d increasing with increasing ion mass from ~ 15 to 50 nm as shown by the empty symbols in Fig. 5.5. [46] The L_d in Ref. [46] was estimated as the average intercascade distance when $n(t_{on}) = 2n(t_{on} \rightarrow 0)$. A more recent work [80] described the t_{on} dependence by assuming a linear relation between Poisson distributed ion cascade overlap and stable disorder. Such measurements of L_d were likely closer to an effective diffusion zone for cascades which is a convolution of both the defect diffusion length and cascade size. Most importantly, neither of these models accounts for the differences in cascade density between ion masses. In contrast, $L_d^{fractal}$ is a measure of the average diffusion length of defects within a cascade with well-defined fractal cascade density. Thus, the increase in L_d in Fig. 5.5 (empty symbols) with increasing ion mass is likely due to the increase in relative cascade size, whereas the decrease in $L_d^{fractal}$ is likely the result of the increasing trap density for defects with increasing ion mass. For both L_d and $L_d^{fractal}$, the diffusion lengths are in quantitative agreement with previous estimates of L_d in Si bombarded with ions or electrons at RT [10, 31–34] but are much smaller than a L_d of ~ 300 to 2000 nm estimated in previous measurements of low dose implanted Si. [35–38]

Figure 5.6 shows an $L_d^{fractal}$ of $\sim 4-6$ nm which increases slightly with increasing temperature in the range of $20-200$ °C for 500 keV Ar into $3C-$SiC. The experimental dependence of the relative disorder on t_{on} was previously published elsewhere [70] showing an L_d of ~ 10 nm with a weak temperature dependence. [70] However, these estimates of L_d did not take into account the fractal structure of cascades, instead viewing the cascades as cylinders. Despite the difference of approximately a factor of two between $L_d^{fractal}$ and the L_d previously reported, $L_d^{fractal}$ shows a similar weak dependence on temperature.

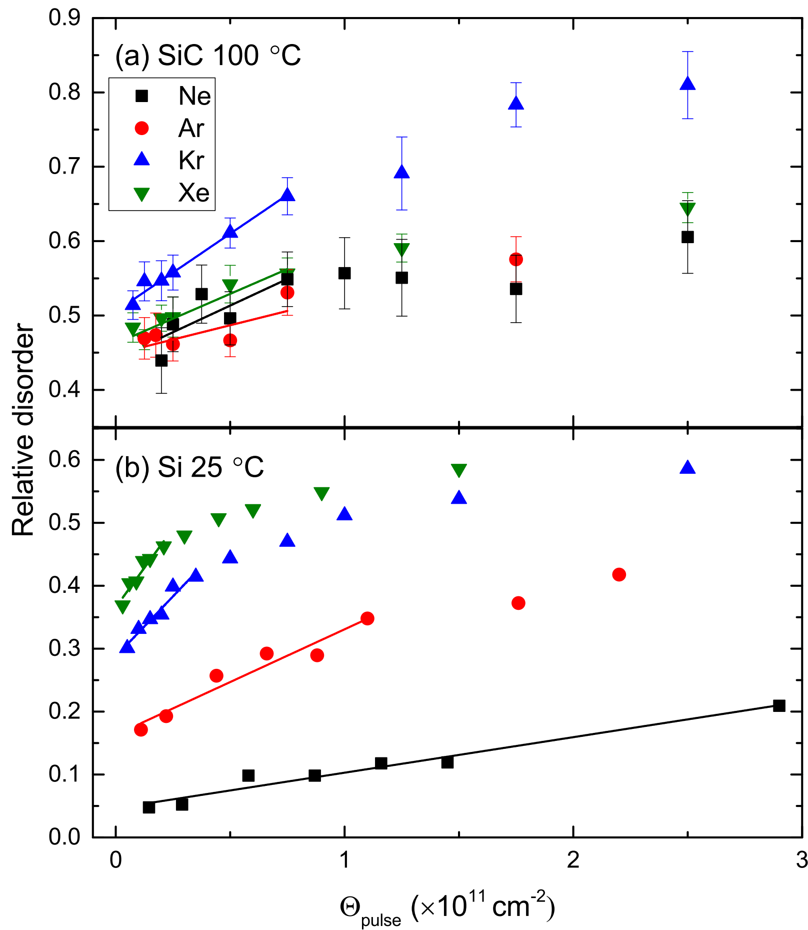

Figure 5.4: (Color online) Dependence of relative disorder at the maximum of the bulk defect peak in (a) SiC bombarded at 100 °C and (b) Si bombarded at RT with pulsed beams of 500 keV Ne, Ar, Kr, and Xe ions on the dose per pulse. Solid lines depict fitting to the fractal diffusion length model derived herein.

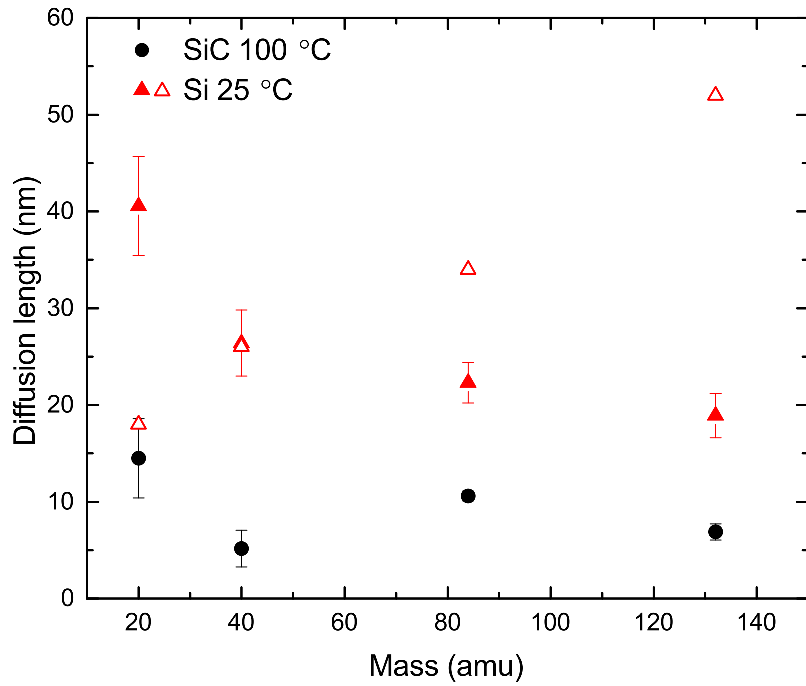

Figure 5.5: (Color online) Dependence of fractal defect diffusion length ($L_d^{fractal}$, solid symbols) and previously reported diffusion length [46] (L_d, open triangle symbols) on ion mass for bombardment of SiC at 100 °C and Si at RT with a pulsed beam of 500 keV Ne, Ar, Kr, and Xe ions.

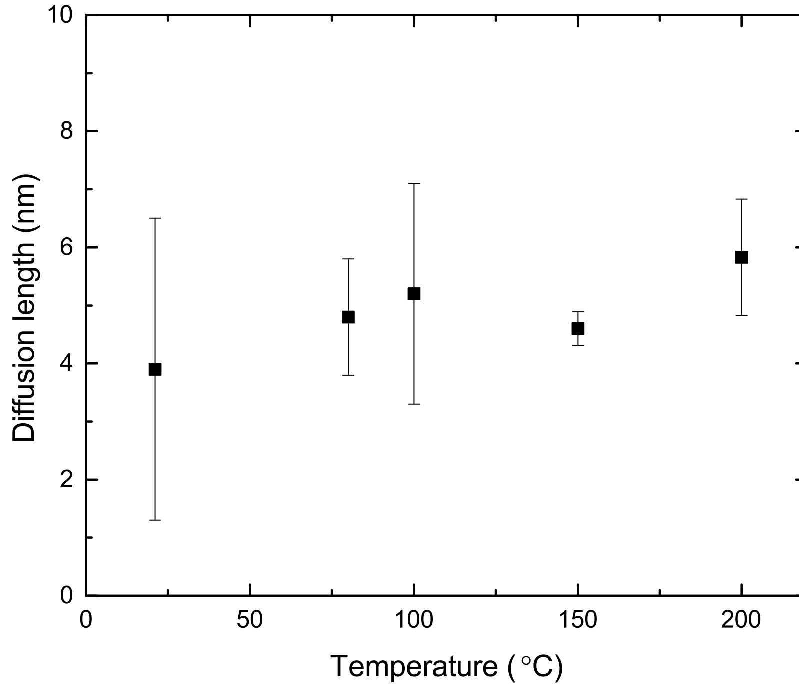

Figure 5.6: (Color online) Temperature dependence of the effective defect diffusion length (L_d) in $3C$-SiC bombarded with 500 keV Ar ions.

5.1.5 Conclusion

In this study, the pulsed ion beam method was linked to a radiation damage model which accounted for the fractal behavior of collision cascades. Using this approach, we showed the defect diffusion length in $3C-$SiC at 100 $°C$ bombarded with 500 keV Ne, Ar, Kr, and Xe ions. With increasing ion mass (and cascade density) the diffusion length increases weakly in the range from $\sim$ 5 to 15 nm. In addition, re-analysis of previously published data for $3C-$SiC bombarded with 500 keV Ar in the temperature range of $25 - 200$ $°C$ revealed a diffusion length which increased weakly with increasing T in the range of $\sim 4 - 6$ nm. In contrast, re-analysis of data for Si at RT bombarded by 500 keV Ne, Ar, Kr, and Xe showed a decreasing diffusion length from $\sim 40 - 20$ nm with increasing ion mass and, hence, cascade density. This

study provides a novel method for measuring the average defect diffusion length in ion cascades while accounting for the fractal behavior.

5.2 Influence of cascade density on radiation defect dynamics in Si studied by pulsed ion beam

5.2.1 Introduction

The formation of stable radiation damage is often affected by the spatial and temporal proximity of mobile point defects and their interaction through so-called dynamic annealing (DA) processes involving migration, recombination, and clustering *during irradiation.* [42] The spatial density of point defects within an ion cascade (cascade density), is a strong function of ion and target mass. [1,25] Despite decades of research into cascade density, its effect on the interaction processes of DA remains unknown even for Si, which is arguably the most simple and well-understood material in the field of ion implantation.

Previous studies [6,8,26,44] of the effect of ion mass on DA processes have revealed a continuum of activation energies (E_a) ranging from $\sim$ 0.2 - 1.7 eV depending on ion mass, temperature and technique. For example Golderg et al., [8] building on the work of Schultz et al., [6] found E_as in a wide range from $\sim 0.7 - 1.7$ eV for 80 keV ions with masses ranging from ^{12}C to ^{132}Xe and temperature (T) in the range of $\sim 10 - 300$ °C. They [8] have found that the E_a value increases close-to-linearly with either ion mass or T (since, with increasing ion mass, the onset of bulk amorphization occurs at higher Ts for any given dose and dose rate). Kinomura et al., [26] following the work of Linnros et al., [44] have systematically studied T dependencies of the rate of ion-beam-induced epitaxial crystallization and found E_a values of $\sim 0.3 - 0.4$ eV in the T range of $\sim 250 - 400$ °C for irradiation with 3 MeV C, Si, Ge, or Au ions and an E_a of ~ 0.2 eV for 3 MeV C ion bombardment in the T range of $\sim 150 - 280$

°C.

Recently, using a novel pulsed ion beam technique, [15,45–48,70,81] an E_a of ~ 0.1 and 0.4 eV was measured for the temperature dependence of the dynamic annealing rate in Ar bombarded Si above and below ~ 60 °C, respectively. [81] These E_as, were attributed to the dynamic annealing rate limiting migration of Frenkel pair defects as supported by modeling. [81] In a separate study [46] the DA defect lifetime was shown to increase with increasing ion mass. Although these studies clarified much in the way of DA in Si, many questions were left unanswered. For example, what is the origin of the critical transition temperature (T_c) at 60 °C. How does cascade density, ion energy, mass, and DPA rate affect the measured activation energies?

In this study, we use the pulsed ion beam method to answer these questions. Dynamic annealing in float-zone Si is studied as a function of temperature in the range from -30 – 210 °C for irradiation by 500 keV $^{20}Ne^+$, $^{84}Kr^+$, or $^{129}Xe^+$ and compared to previous data for $^{40}Ar^+$. Results across ion masses are compared using a model for radiation damage which captures the fractal nature of collision cascades. All ion masses showed qualitatively similar Arrhenius behavior with a drastic change in the DA rate above a critical temperature (T_c). For Ne, Ar, and Kr, E_as of ~ 0.4 and 0.1 eV are found, suggesting similar DA processes in all three cases. For Kr irradiations, τ and E_a were analyzed as a function of depth and hence at different cascade density, DPA rate, energy, and dose. Results, revealed no change in either high or low T E_as. However, T_c was found to decrease towards the surface. In contrast, the E_as of Xe are ~ 0.1 and 0.8 eV in the bulk where cascade density is highest and ~ 0.1 and ~ 0.4 eV in the near surface where the cascade density is similar to the maximum cascade density in Kr irradiated Si. The E_a of ~ 0.8 eV found near the maximum of the cascade density in Xe bombarded Si is similar to previously reported values for the total heat of melting in Si [65] which was suggested

to be responsible for the formation of thermal and displacement spikes in Si [65]. The critical temperature (T_c) at which the activation energy changes from ~ 0.1 to ~ 0.4 or ~ 0.8 eV is shown to increase with increasing ion mass or depth in the sample. Both the ion mass and depth dependencies can be reduced to a single dependence on cascade density. When T_c is plotted as a function of the cascade density, it is shown to increase linearly. These results reveal the effect of collision cascade density on the rate limiting processes of DA in ion irradiated Si.

5.2.2 Experimental

Float-zone grown (100) Si single crystals (with a resistivity of $\sim 5\ \Omega$ cm) were bombarded with 500 keV $^{20}Ne^+$, $^{40}Ar^+$, [81] $^{84}Kr^+$, or $^{129}Xe^+$ ions at 7° off the [100] direction in the T range from -30 to 210 °C. The 4 MV ion accelerator (National Electrostatics Corporation, model 4UH) at Lawrence Livermore National Laboratory was used for both ion irradiation and ion beam analysis. To improve thermal contact, the samples were attached to the Cu sample holder with conductive Ag paste. All irradiations were performed in a broad beam mode [45]. The total dose was split into a train of equal square pulses with instantaneous dose rates of $F_{on} \approx 2.7 \times 10^{13}$, 1.9×10^{13}, 0.8×10^{13}, and 0.45×10^{13} cm^{-2} s^{-1} for Ne, Ar, Kr, and Xe, respectively. In every irradiation, the pulse duration was $t_{on} = 1$ ms, corresponding to $\sim 4.6 \times 10^{-5}$ displacements per atom per pulse [20] in Ar, Kr, and Xe and $\sim 2.9 \times 10^{-5}$ displacements per atom per pulse in Ne. The depth profile of ballistically-generated vacancies was calculated with the TRIM code (version SRIM-2013.00) [20] with an atomic concentration of Si of 4.98×10^{22} atoms cm^{-3} and a threshold energy for atomic displacements of 13 eV. The adjacent pulses were separated by time t_{off}, which was varied between 0.1 and 100 ms. The inset in Fig. 5.7(a) shows a schematic of the time dependence of the instantaneous dose rate and defines pulsing parameters t_{on},

t_{off}, and F_{on}. A more detailed description of the experimental arrangement can be found elsewhere [15, 45–48, 70, 81].

The dependence of lattice damage on t_{off} was studied *ex-situ* at room T by ion channeling. Depth profiles of lattice disorder were measured with 2 MeV $^4He^+$ ions incident along the [100] direction and backscattered into a detector at 164° relative to the incident beam direction. Raw channeling spectra were analyzed with one of the conventional algorithms [18] for extracting depth profiles of relative disorder. Values of average bulk relative disorder (n) were obtained by averaging depth profiles of relative disorder over 20 channels ($\sim$ 38 nm). Error bars of n are standard deviations. Total ion doses at different Ts were different and chosen such that, for continuous beam irradiation (i.e., $t_{off} = 0$), n was in the range of $0.6 - 0.9$ (with $n = 1$ corresponding to full amorphization).

Depth profiles and three-dimensional distributions of ballistically-generated lattice vacancies were calculated with the TRIM code (version SRIM-2013.00, full cascade calculations) [20] with an atomic concentration in Si of 5.0×10^{22} atoms cm^{-3}. The threshold energies for atomic displacement in Si was 15 eV.

Cascade densities ($\rho_{cascade}$s) at R_{pd}s were calculated based on the algorithm similar to that proposed by Heinisch and Singh. [74] We define the $\rho_{cascade}$ as the average local density of lattice vacancies within individual cascades with an averaging radius of 20 nm. Such an averaging radius was chosen to be comparable with our recent estimates of the L_d in Si. [82] Values of $\rho_{cascade}$ were obtained by averaging over $\gtrsim 600$ individual cascades.

5.2.3 Results and discussion

Figure 5.7 shows representative depth profiles of relative disorder for Ar and Xe ion bombardment of Si with continuous ($t_{off} = 0$ ms) and pulsed ($t_{off} = 1$ and 2

ms) beams at Ts of (a) 100 and (b) 140 °C. It is seen that, for both Ts, these depth profiles are bimodal, with the first small peak at the sample surface and the second major peak in the crystal bulk. The bulk peaks are centered on $\sim$ 500 and 180 nm, which corresponds to the maximum of the nuclear energy loss profile for 500 keV Ar and Xe ions, respectively [20]. It is seen from Fig. 5.7 that the average bulk disorder (n) decreases with increasing t_{off} for both Ts and both ion species. In addition, the rate of change in stable disorder with changing t_{off} appears much faster under Ar irradiation compared to Xe irradiation.

The dynamic annealing behavior is better illustrated in Fig. 5.8, which summarizes $n(t_{off})$ dependencies for Ts in the range from -30 to 210 °C for (a) Xe, (b) Kr, (c) Ar [81], and (d) Ne. It is seen from Fig. 5.8 that, for all the Ts studied, n monotonically decreases with increasing t_{off}. This effect is due to the interaction of mobile defects generated in different pulses and, hence, in different cascades (i.e., inter-cascade defect interaction). Solid lines in Fig. 5.8 are fits of the data via the Marquardt-Levenberg algorithm [54] with the first order ($n(t_{off}) = n_\infty + (n(0) - n_\infty)\exp(-t_{off}/\tau)$) decay equation. The evaluation of the kinetic order of $n(t_{off})$ dependencies was done by comparing R-squared values of fits with the first and second order decay equations. In all the cases of different Ts, however, R-squared values were > 0.96. Here, τ is the characteristic decay time constant, and n_∞ is relative disorder for $t_{off} >> \tau$. In a first kinetic order process, the rate is directly proportional to the concentration of interacting species. Examples of the first order processes include trapping of interstitials or vacancies at sinks. Since a decrease in n with increasing t_{off} is a result of inter-cascade defect interaction, the time constant τ reflects inter-cascade and inter-pulse defect interaction processes.

Temperature dependencies of τ are plotted in Fig. 5.9(a), revealing a decrease with increasing T and decreasing ion mass. The decrease in τ with increasing T

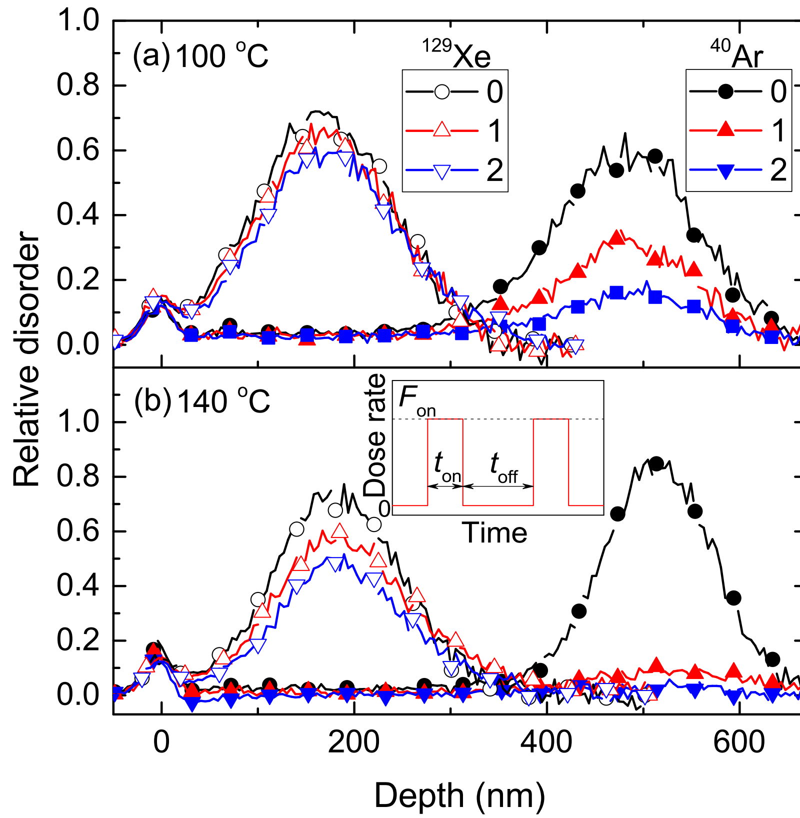

Figure 5.7: (Color online) Selected depth profiles of relative disorder in Si bombarded with a pulsed beam of 500 keV Ar and Xe ions with $F_{on} = 1.9 \times 10^{13}$ and 0.5×10^{13} cm^{-2} s^{-1} respectively, t_{on} = 1 ms, and different t_{off} values given in legends at temperatures of (a) 100 °C and (b) 140 °C. For clarity, only every 10th experimental point is depicted. The inset in (b) is a schematic of the time dependence of the instantaneous dose rate for pulsed beam irradiation, defining t_{on}, t_{off}, and F_{on}.

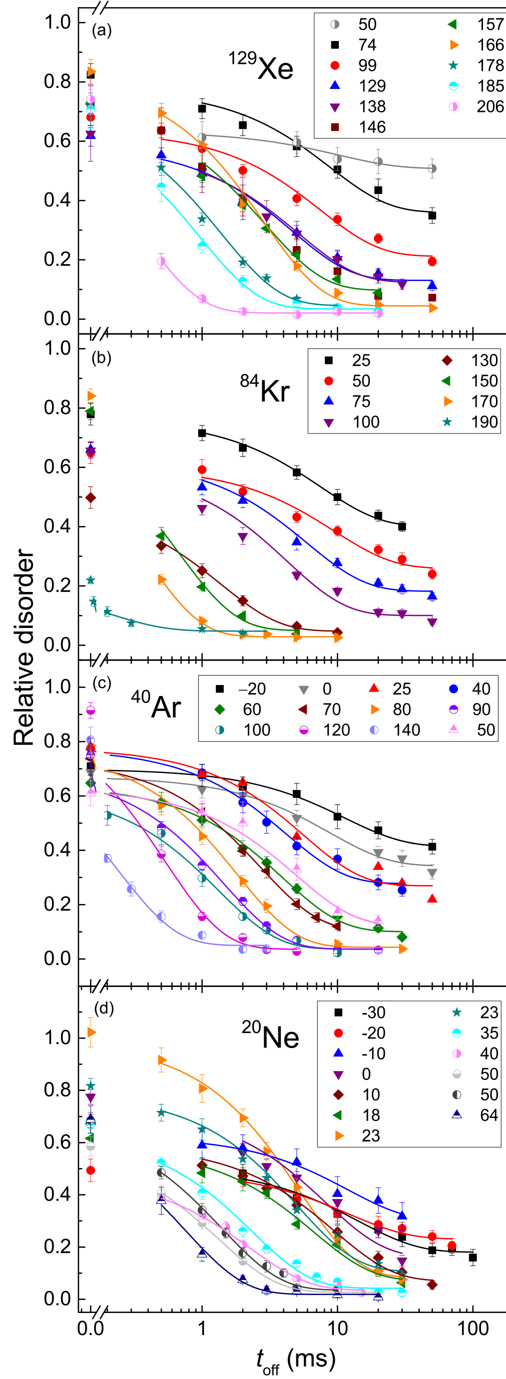

Figure 5.8: (Color online) Relative bulk disorder in Si bombarded at different temperatures (given in the legend in units of °C) with a pulsed beam of 500 keV (a) Xe, (b) Kr, (c) Ar and, (d) Ne ions with $F_{on} \approx 0.45 \times 10^{13}$, 0.8×10^{13}, 1.9×10^{13}, and 2.7×10^{13} cm^{-2} s^{-1}, respectively, and $t_{on} = 1$ ms as a function of the passive portion of the beam duty cycle (t_{off}). Solid lines show the results of fitting the data with the first order decay equations.

agrees with previous studies [6, 8, 26, 44] which showed DA in Si to be a thermally activated process. In addition, the decrease in τ with increasing ion mass and hence cascade density is in agreement with previous pulsed beam studies. However, this finding is the opposite of what was suggested by Kinomura, Williams, and Fujii [26] in their systematic study of the ion mass effect on the rate of ion-beam-induced epitaxial crystallization (IBIEC) in Si. Indeed, they [26] argued that τ should be smaller for heavier ions, which would be expected for simple cases of nonlinear defect accumulation such as the formation of divacancies by trapping of two isolated vacancies. In such cases, an increase in cascade density should result in more efficient and faster defect annihilation and, hence, shorter τ. Such arguments [26] contradict our experimental finding that τ increases with increasing ion mass [Fig. 5.9(a)].

Figure 5.9(b) shows the T dependence of the DA efficiency ξ, which is define as before [45,46]: $\xi = (n(0) - n_{\infty})/n(0)$. Figure 5.9(b) shows that, within experimental errors, ξ increases with T for all ion masses, reflecting a corresponding decrease in n_{∞}, which is also clearly seen in $n(t_{off})$ dependencies of Fig. 5.8. With increasing ion mass, ξ rapidly decreases. This indicates that, for heavier ions, the intra-cascade formation of stable lattice disorder becomes more efficient and a smaller fraction of atomic displacements participate in DA processes. Therefore, the cascade density influences not only the defect production efficiency (the fact that has been well established albeit not fully understood) [1,25] but also the defect interaction dynamics.

In Fig. 5.10, we replot the $\tau(T)$ dependencies from Fig. 5.9 in Arrhenius coordinates, with the DA rate defined as $\frac{1}{\tau_1}$ for the first order decay processes and with kT having the usual meaning. For each ion mass in Fig. 5.10, two Arrhenius regimes are clearly seen. Linear fitting of the data gives E_as of ~ 0.1 at lower temperature and ~ 0.4 or ~ 0.8 eV at higher temperature as, shown in Fig. 5.10. The pre-exponential factors were 5.2×10^{12}, 8.0×10^{8}, 5.2×10^{8}, and 1.0×10^{9} Hz above T_c and 3.5×10^{4},

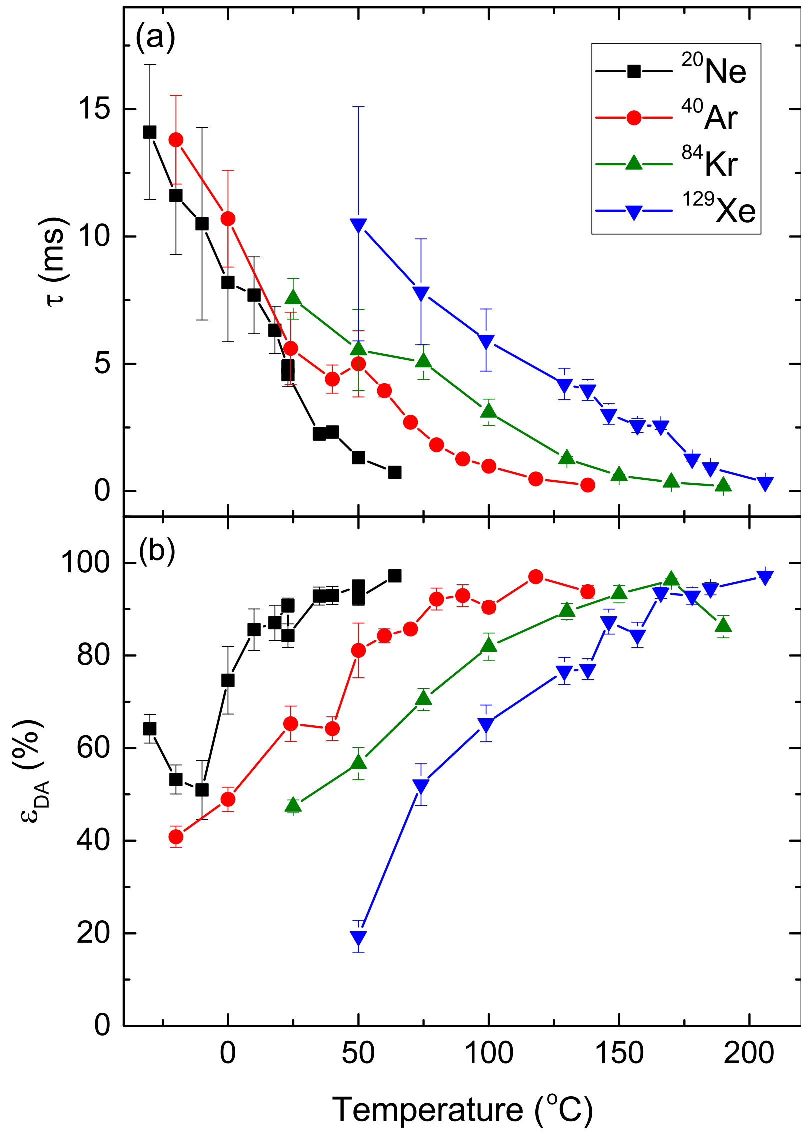

Figure 5.9: (Color online) Temperature dependencies of (a) the effective time constant of DA (τ) and (b) the DA efficiency (ξ) for fitting of the bulk relative disorder with the first order decay equations in Si bombarded with a pulsed ion beam 500 keV Ne, Ar, Kr, and Xe ions.

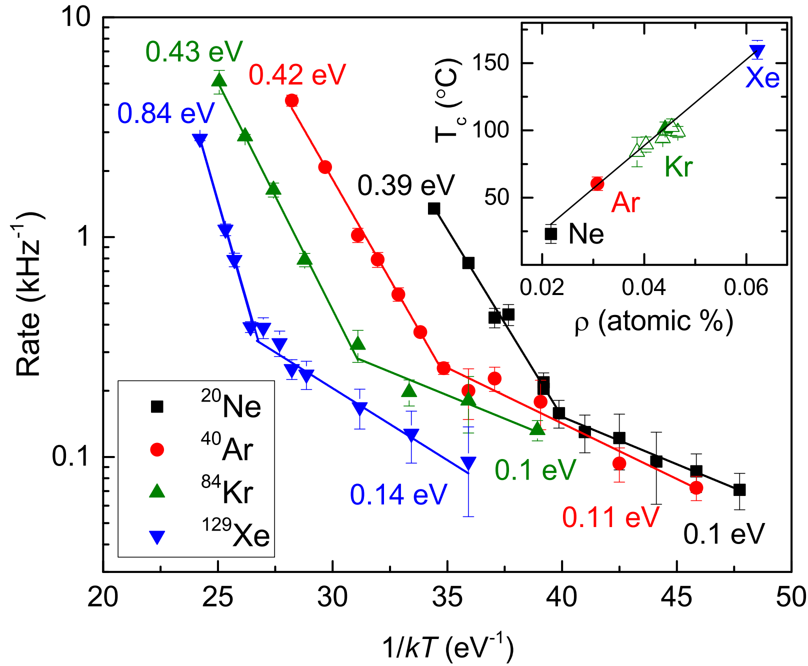

Figure 5.10: (Color online) Arrhenius plot of the DA rate for Si bombarded with a pulsed ion beam 500 keV Ne, Ar, Kr, and Xe ions. Straight lines show results of linear fitting, revealing activation energies of $\sim$ 0.4 eV and $\sim$ 0.1 eV for Ne, Ar, and Kr and $\sim$ 0.8 and $\sim$ 0.1 eV for Xe at low and high T, respectively. The inset shows the critical temperature (T_c) of dynamic annealing at which E_a changes for each ion as a function of cascade density [82] (ρ) evaluated at $R_c = 20$ nm. For Kr, T_c in the inset is shown at depths between $\sim$ 150 and 400 nm (open symbols) with ρ corresponding to the cascade density at each depth.

5.1×10^3, 1.5×10^4, and 7.9×10^3 Hz below T_c for Ne, Ar, Kr, and Xe, respectively.

The critical temperature (T_c) at which the activation energy changes from 0.1 to 0.4 or 0.8 eV in Fig. 5.10 is shown to increase with increasing ion mass and, hence, cascade density. The inset in Fig. 5.10 shows T_c as a function of cascade density [82] from a single pulse. The T_c is shown to increase almost linearly with increasing cascade density. It should also be noted that if plotted on an Arrhenius scale, the cascade density increases with an activation energy of $\sim$ 0.1 eV. Further work in modeling of dynamic annealing processes is required to understand why the

critical cascade density should increase linearly or follow Arrhenius behavior with T_c. However, such linearity makes predicting the critical temperature across a range of cascade densities straightforward.

Previous pulsed ion irradiations in Si by 500 keV Ar [81] attributed the 0.1 [50,53] and 0.4 [49–51] eV activation energies to the rate limiting migration of Frenkel pair defects *during irradiation*. For Ne, Ar, and Kr the activation energies in Fig. 5.10 are similar, which suggest similar rate limiting processes in all three ion species. In contrast, the activation energies in Xe irradiations are $\sim$ 0.1 and 0.8 eV below and above 160 °C, respectively. The increase in the high T activation energy for DA in Xe in comparison to Ne, Ar, and Kr cannot be attributed simply to a change in temperature since the Kr and Xe temperature ranges overlap significantly. Instead, the increase in E_a could be due to a threshold cascade density effect.

Towards the surface of the material, where the ion energy is higher, the cross section for elastic scattering collisions decreases leading to a lower cascade density. This depth dependence of cascade density provides a means to test whether the change in E_a from 0.4 to 0.8 eV demonstrated above is the result of a threshold cascade density effect. To test this hypothesis, we calculate Kr and Xe cascade densities as a function of depth. [82] Figure 5.11 shows the cascade density (left axis) as a function of depth for 500 keV Kr and Xe into Si. The peak of the cascade density occurs at $\sim$ 350 and 180 nm for Kr and Xe, respectively. Since the cascade density decreases toward the surface where the nuclear stopping power is lower, analyzing τ and E_a as a function of depth provides a means to characterize the role of cascade density across a continuum of values for each ion. The vertical dashed line at $\sim$ 60 nm in Fig. 5.11 shows the depth at which the cascade density in Xe is equal to the maximum of the cascade density in Kr. If the change in high T E_a observed in Xe irradiation is the due to cascade density effects, then E_a should decrease to

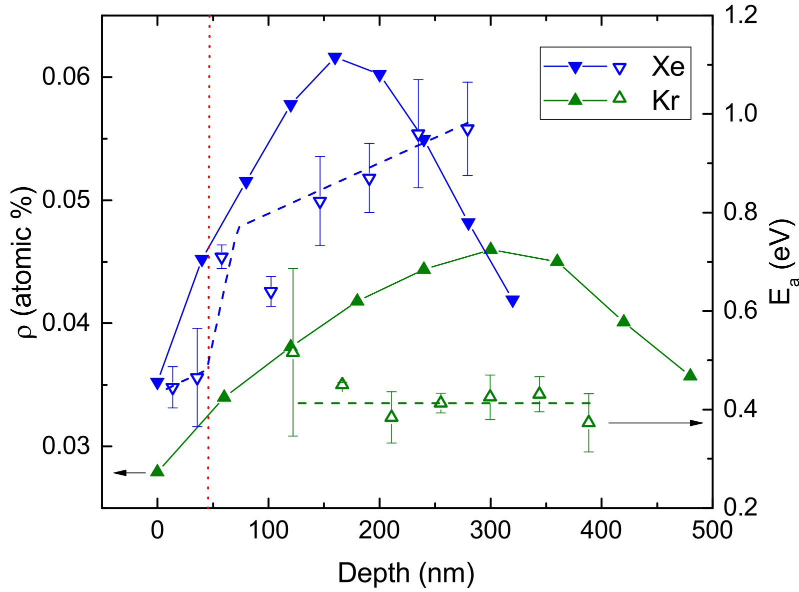

Figure 5.11: (Color online) Cascade density [82] as a function of depth from TRIM simulated Kr and Xe ion cascades in Si evaluated with $R_c = 20$ nm (left axis) and the activation energy at high T (right axis) as a function of depth in Kr and Xe. The dotted vertical line shows the depth at which the cascade density in Xe drops below the peak cascade density in Kr. Dashed lines over E_a values are to guide the eye.

~ 0.4 eV at depths less than ~ 60 nm.

Figure 5.11 shows E_a (right axis) in Kr and Xe as a function of depth. The E_a of Kr is approximately constant from the depth of $\sim 100 - 400$ nm. However, T_c decreases linearly with decreasing cascade density toward the surface, as shown in Fig. 5.10. A similar linear change was observed with changing cascade density from changing ion mass. This suggest that the cascade density defined through our fractal model is the fundamental parameter determining T_c.

In contrast to Kr, the E_a in Xe is seen to decrease from ~ 0.95 ev at 300 nm (well beyond the maximum of the bulk relative disorder) to ~ 0.7 eV at 100 nm. Below 100 nm, the E_a in Xe drops sharply to ~ 0.45 eV. The abrupt change in E_a below ~ 100 nm suggest the existence of a threshold cascade density at ~ 0.023 V/nm^3

or ~ 0.04 atomic percent. Below this threshold, DA appears to be rate limited by the migration rate of Frenkel pair defects as suggested by previous studies [81] and further supported in this study. Above the threshold, the activation energy increases to ~ 0.7 - 0.9 eV, which corresponds to previously suggested values for the total heat of melting in Si. [65] Thompson et al. [65] suggest that this E_a may indicate the presence of thermal or displacement spikes in Si. However, additional modeling efforts are required to justify such a claim.

Furthermore, the consistency of E_a with depth in Kr further suggest that this E_a may be fundamental to DA in Si. With changing depth the DPA rate, total DPA, total disorder, and effective ion energy are all changing. It is possible that these parameters are acting in unison to cancel one another. However, the more likely scenario is that the E_a of the dominant DA processes in Si is independent of these experimental parameters in the range studied. It should also be noted that the low T E_a in both Xe and Kr of ~ 0.1 eV was, within error bars, independent of depth.

5.2.4 Conclusion

In this study, we have shown the effect of cascade density on the characteristic time constant of dynamic annealing (τ) in Si bombarded by 500 keV Ne, Ar, Kr, or Xe ions in the temperature range from ~ -30 to 210 °C. Results showed τ to decrease monotonically with both increasing temperature and increasing ion mass. In each ion, the dynamic annealing rate revealed two well defined Arrhenius regions above and below a critical temperature (T_c). The T_c was found to increase with increasing ion mass and increasing depth towards the maximum of cascade density. Using a fractal model [82] of cascade density, we found that T_c increases close to linearly with increasing cascade density. For Ne, Ar, and Kr irradiations, the activation energies were independent of ion mass and hence cascade density giving values of

$\sim$ 0.1 and 0.4 eV below and above the T_c for each ion, respectively. In addition, Ne, Ar, and Kr activation energies were approximately constant with depth and hence cascade density. This result suggest similar rate limiting processes of dynamic annealing at all depths and ion cascade densities. Previous pulsed beam studies showed evidence that these activation energies represented the rate limiting migration of Frenkel defects. In contrast, in Xe irradiations, the activation energy is $\sim$ 0.8 eV in the bulk and decreases sharply to $\sim$ 0.4 eV near the surface where the cascade density is comparable to the maximum cascade density in Kr irradiations. This result suggest the existence of a threshold cascade density effect in Si, which corresponds to a change in the rate limiting processes of dynamic annealing. These results reveal the effect of ion cascade density on the rate limiting processes controlling dynamic annealing in Si.

5.3 The effect of super-cascade density on dynamic annealing in Si

5.3.1 Introduction

The formation of stable radiation damage is often strongly dependent on the spatial and temporal distribution of mobile radiation generated defects. Through so-called dynamic annealing(DA) processes defects migrate, recombine, and cluster into a wide array of defect complexes. [42] The relevant spatial and temporal scales of DA are dependent on the concentration of defects within a cascade, referred to as *cascade density effects*, and the relative concentration of cascades in the material, referred to as *flux effects*. [1,25] Although these effects have been studied as separate aspects of DA, the defect concentration is the underlying mechanism driving both effects. Despite decades of research there is still no clear link between cascade density effects and flux effects.

The current lack of understanding is a reflection of the complexity of such effects.

Describing the distribution of defects within a cascade is non-trivial and has been the subject of numerous studies. Cheng et al. [66] and Winterbon et al. [67] showed that the spatial distribution of defects within a collision cascade can be described with the framework of fractal geometry. [68] The fractal description of collision cascades was recently used to describe the DA defect diffusion length in ion irradiated Si and SiC. [82] The fractal super-cascade density was defined as,

$$\rho = \frac{3k_{\circ}R_c^{D-3}}{4\pi} + g\phi_{pulse}, \tag{5.3}$$

Where $k_{\circ}$ is the fractal structure factor, R_c is the averaging radius around defects, D is the fractal dimension, g is the TRIM calculated DPA/ion-A, and ϕ_{pulse} is the ion fluence per pulse. Here we define the super-cascade density as the fractal-defined density of defects (Eq. 5.3) within a sphere of radius R_c around a given defect for multiple coincident overlapping ion cascades. Thus, super-cascade density is a hybridization of fractal cascade density and flux effect concepts.

In this study we apply the pulsed ion beam method to study the role of *super-cascade* defect density in Si bombarded with 500 keV Ne, Ar, and Xe ions. Here we study the effect of super-cascade density by performing multiple measurements of the characteristic DA lifetime of defects (τ_{impact}) over a range of ion fluence-per-pulse settings. Results reveal that below a critical fluence-per-pulse(ϕ_{L_d}), τ_{impact} decreases with increasing super-cascade density below T_c, where DA is rate limited by 2nd order kinetics, whereas τ_{impact} is approximately constant above T_c where DA is rate limited by 1st order kinetics. However, above ϕ_{L_d}, τ_{impact} was shown to increase for all ion masses. Furthermore, the T_c value is shown to increase linearly with increasing super-cascade density from changing fluence-per-pulse, changing ion mass, and changing depth. This last result suggests that the concept of super-cascade density is the link

between describing cascade density effects and flux effects.

5.3.2 Experimental

Float-zone grown (100) Si single crystals (with a resistivity of $\sim 5\ \Omega$ cm) were bombarded with 500 keV $^{20}Ne^{+}$, $^{40}Ar^{+}$, or $^{129}Xe^{+}$ ions at 7° off the [100] direction in the T range from 20 to 100 °C. The 4 MV ion accelerator (National Electrostatics Corporation, model 4UH) at Lawrence Livermore National Laboratory was used for both ion irradiation and ion beam analysis. To improve thermal contact, the samples were attached to the Cu sample holder with conductive Ag paste. All irradiations were performed in a broad beam mode [45]. The total dose was split into a train of equal square pulses with instantaneous dose rates of $F_{on} \approx 2.7 \times 10^{13}$, 1.9×10^{13}, and 0.45×10^{13} cm^{-2} s^{-1} for Ne, Ar, and Xe, respectively. The adjacent pulses were separated by time t_{off}, which was varied between 0.1 and 100 ms. The pulse duration was varied between 0.2 and 50 ms. The inset in Fig. 5.12(a) shows a schematic of the time dependence of the instantaneous dose rate and defines pulsing parameters t_{on}, t_{off}, and F_{on}. A more detailed description of the experimental arrangement can be found elsewhere [15, 45–48, 70, 80, 81, 83].

The dependence of lattice damage on t_{off} was studied *ex-situ* at room T by ion channeling. Depth profiles of lattice disorder were measured with 2 MeV $^{4}He^{+}$ ions incident along the [100] direction and backscattered into a detector at 164° relative to the incident beam direction. Raw channeling spectra were analyzed with one of the conventional algorithms [18] for extracting depth profiles of relative disorder. Values of average bulk relative disorder (n) were obtained by averaging depth profiles of relative disorder over 20 channels ($\sim$ 38 nm). Error bars of n are standard deviations. Total ion doses at different Ts were different and chosen such that, for continuous beam irradiation (i.e., $t_{off} = 0$), n was in the range of $0.6 - 0.9$ (with $n = 1$

corresponding to full amorphization).

Depth profiles and three-dimensional distributions of ballistically-generated lattice vacancies were calculated with the TRIM code (version SRIM-2013.00, full cascade calculations) [20] with an atomic concentration in Si of 5.0×10^{22} atoms cm^{-3}. The threshold energies for atomic displacement in Si was 15 eV.

Cascade densities ($\rho_{cascade}$s) at R_{pd}s were calculated based on the algorithm similar to that proposed by Heinisch and Singh. [74] We define the $\rho_{cascade}$ as the average local density of lattice vacancies within individual cascades with an averaging radius of 20 nm. Such an averaging radius was chosen to be comparable with our recent estimates of the L_d in Si. [82] Values of $\rho_{cascade}$ were obtained by averaging over $\gtrsim 600$ individual cascades.

5.3.3 Results and discussion

Figure 5.12 shows representative depth profiles of relative disorder for Ar ion bombardment of Si at 100 °C with pulsed (t_{off} values given in the legend) beams at t_{on}s of (a) 0.5 and (b) 5 ms. It is seen that, for all irradiations, the depth profiles are bimodal, with the first small peak at the sample surface and the second major peak in the crystal bulk. The bulk peak is centered on ~ 500 nm, which corresponds to the maximum of the nuclear energy loss profile for 500 keV Ar ions in Si. It is seen from Fig. 5.12 that the average bulk disorder (n) decreases with increasing t_{off} for both t_{on} values.

The dynamic annealing behavior is better illustrated in Fig. 5.13, which summarizes $n(t_{off})$ dependencies for t_{on}s in the range of 0.3 – 20 ms for Si irradiated at 100 °C with a pulsed beam of 500 keV Ar. It is seen from Fig. 5.13 that, for all the t_{on}s studied, n monotonically decreases with increasing t_{off}. This effect is due to the interaction of mobile defects generated in different pulses and, hence,

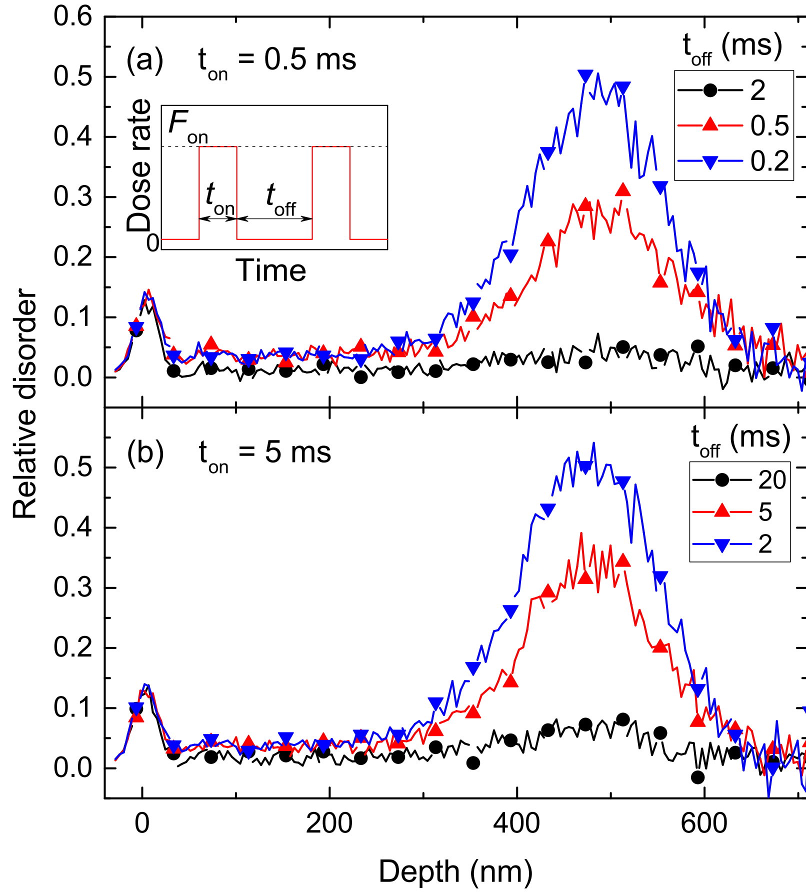

Figure 5.12: (Color online) Selected depth profiles of relative disorder in Si bombarded at 100 °C with a pulsed beam of 500 keV Ar ions with $F_{on} = 1.8 \times 10^{13}$, fluence of 9.0×10^{14} cm^{-2}, and different t_{off} values given in legends at $t_{on} = 0.5$ (a) and 5 (b) ms. For clarity, only every 10th experimental point is depicted. The inset in (a) is a schematic of the time dependence of the instantaneous dose rate for pulsed beam irradiation, defining t_{on}, t_{off}, and F_{on}.

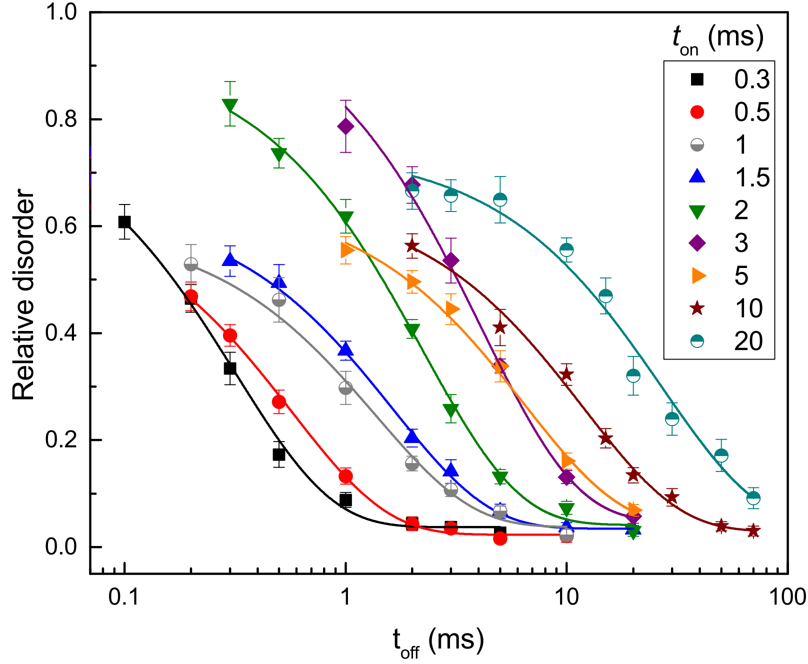

Figure 5.13: (Color online) Relative bulk disorder in Si bombarded at 100 °C with a pulsed beam of 500 keV Ar ions with $F_{on} = 1.8 \times 10^{13}$ cm^{-2} s^{-1} and t_{on} given in the legend in units of ms as a function of the passive portion of the beam duty cycle (t_{off}). Results of fitting the data with the first order decay equations are shown by solid lines.

in different cascades (i.e., inter-cascade defect interaction). Solid lines in Fig. 5.13 are fits of the data via the Marquardt-Levenberg algorithm [54] with the first order ($n(t_{off}) = n_\infty + (n(0) - n_\infty)\exp(-t_{off}/\tau)$) decay equation. The evaluation of the kinetic order of $n(t_{off})$ dependencies was done by comparing R-squared values of fits with the first and second order decay equations. In all the cases of different Ts, however, R-squared values were > 0.96. Here, τ is the characteristic decay time constant, and n_∞ is relative disorder for $t_{off} >> \tau$. Since a decrease in n with increasing t_{off} is a result of inter-cascade defect interaction, the time constant τ reflects inter-cascade defect interaction processes.

The resulting τ from fitting the data in Fig. 5.13 is shown in Fig. 5.14(a) along

with additional pulsed beam experiments at temperatures and ion species given in the legend. Under all irradiations conditions used in this study, τ was observed to increase with increasing t_{on}. The increase in τ with increasing t_{on} is due to (1) a change in defect lifetime with changing super-cascade density within a single pulse and (2) changing average effective time between ion impacts into L_d defined (diffusion zone) regions. The former effect is a reflection of the actual physics of defect interaction changing whereas the latter is an artifact of the choice of the t_{on} parameter and should be separated from (1). Separating (1) and (2) requires knowledge of the characteristic DA diffusion length (L_d), which was studied in Si at RT and 100 °C. [46, 80] The L_d values can be used to determine the average time between ion impacts (t_{off}^{impact}) into L_d-defined regions as a function of t_{on}. When the average number of ion impacts per pulse into L_d defined regions of space is unity, we define the beam time on as $t_{on}^{L_d}$. For $t_{on} < t_{on}^{L_d}$, the time between ion impacts is $t_{off}^{impact} = (t_{on} + t_{off})\frac{t_{on}^{L_d}}{t_{on}}$. When $t_{on} > t_{on}^{L_d}$, $t_{off}^{impact} = (t_{off} + t_{on}^{L_d})$. See Ref. [46] for a detailed derivation and discussion of t_{off}^{impact}.

Fitting the $n(t_{off}^{impact})$ to the first order decay equation gives $\tau_{impact}(t_{on})$ dependencies shown in Figure 5.14(b). Whereas, τ was dependent on both the changing super-cascade density within a single pulse and the choice of t_{on}, τ_{impact} is dependent on only the change in super-cascade density within a single pulse. Below $t_{on}^{L_d}$, τ_{impact} for Ar irradiations at RT and 40 °C and Xe irradiation at 100 °C is shown to decrease with increasing t_{on} and hence super-cascade density. Previous studies in Si showed that DA below the critical temperature ($T_c = 60$ °C) is dominated by 2nd order defect kinetics. An increase in the mobile defect concentration under 2nd order kinetics results in a decrease in τ_{impact} as shown here.

However, this result is in contrast to previous pulsed beam results at RT in which τ increased with increasing ion mass and hence cascade density under a constant DPA

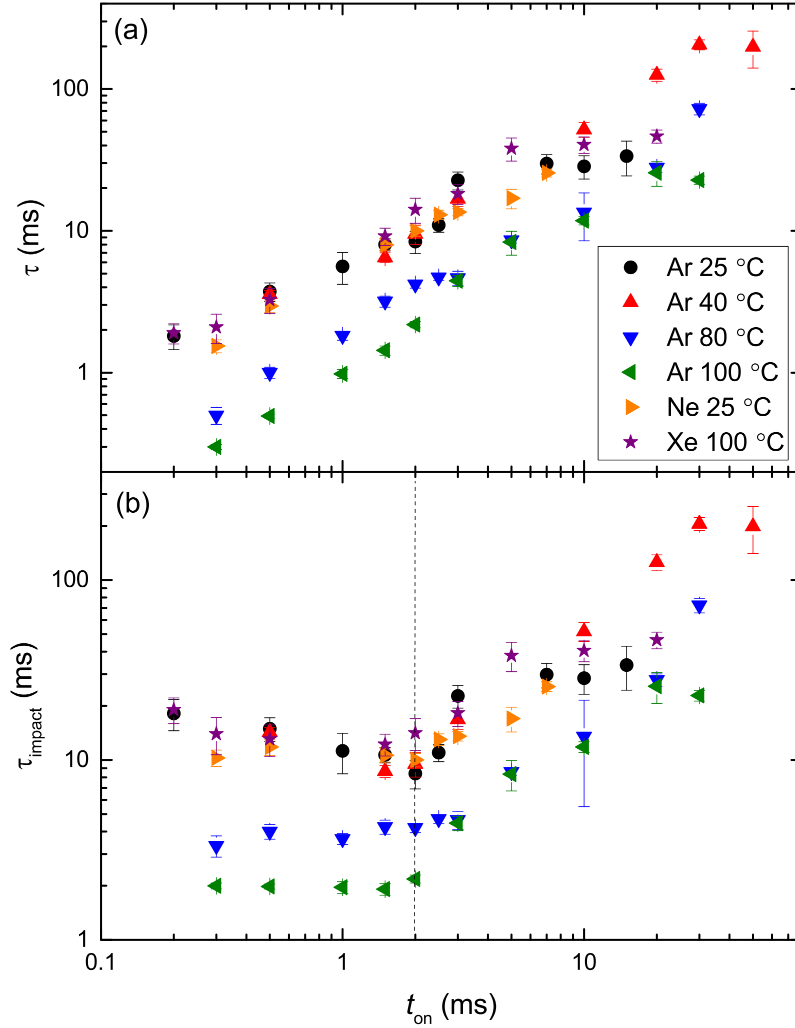

Figure 5.14: (Color online) t_{on} dependencies of the effective time constant of DA (τ_{eff}) for first order fitting of Si bombarded with 500 keV Ne, Ar, and Xe at temperatures given in the legend.

per pulse and t_{on} across all ion masses. It should be noted that τ and τ_{impact} are a measure of the *intercascade* DA time constant. Thus, only the mobile portion of the defect population, which is capable of escaping the cascade core has an effect on the measured τ values. If the total DPA per pulse is held constant as in Ref. [46], then the concentration of mobile defects participating in intercascade DA will likely decrease with increasing ion mass. The DA range, which is proportional to the fraction of defects capable of intercascade DA, is shown to decrease with increasing ion mass hence supporting the above hypothesis. Thus, the increase in τ with increasing ion mass in Ref. [46] is likely due to a decrease in mobile defect concentration, which by definition of second order kinetics, leads to an increase in τ. Thus, the results from Ref. [46] are in agreement with the current study.

In contrast, in the 80 and 100 °C Ar irradiations and RT Ne irradiations, τ_{impact} in Fig. 5.14(b) is approximately constant for $t_{on} < t_{on}^{L_d}$ and begins to increase sharply above $t_{on}^{L_d}$. These temperatures are above the respective transition temperatures (T_c) of $\sim$ 60 °C in Ar and 23 °C in Ne, which marks a change in the dominant processes of DA in Si from 2nd to 1st order kinetics. [83] Since DA above T_c follows 1st order kinetics, [81, 83] the concentration of mobile defects does not appreciably affect τ_{impact}.

The increase in τ_{impact} for all ion species and temperatures above $t_{on}^{L_d}$ is a consequence of multiple overlapping ion cascade volumes within a single pulse. This increase could be due to the fact that as cascades within a single pulse begin to overlap more of the mobile defect concentration is converted into stable disorder leading to a lower net concentration of mobile defects and hence an increase in τ_{impact} as is likely the case in Ref. [46]. The increase of τ_{impact} above $t_{on}^{L_d}$ could also be the result of our model used to determine t_{impact}. More work is required to understand the cascade density behavior above $t_{on}^{L_d}$.

The Ar irradiation τ values in Fig. 5.14 are shown to decrease with increasing T for the majority of t_{on} values studied. In Fig. 5.15 we have plotted the dynamic annealing rate ($1/\tau$) on an Arrhenius axis for various values of t_{on} for Ar irradiations. It should be noted that the activation energy is independent of whether τ or τ_{impact} is used. The activation energy between 80 and 100 °C $\tau(t_{on})$ measurements was constant at $\sim$ 0.4 eV for $t_{on} < 2$ ms. With increasing t_{on}, the critical temperature T_c at which the DA changes from $\sim$ 0.1 to 0.4 eV increases. Previous studies in Si irradiated by 500 keV Ne, Ar, Kr, or Xe showed a linear dependence of T_c with super-cascade density. The inset in Fig. 5.15 shows that when T_c from Ar $t_{on}(\tau)$ measurements is plotted as a function of the cascade density, T_c is approximately where the linear dependence from Ref. [83] predicts it should be. These results demonstrate that T_c is dependent on the local super-cascade density of overlapping cascades within some time interval on the scale of τ_{impact} values reported here. Thus, at a given temperature there is a critical super-cascade density which corresponds to a change in the dominant mechanisms of DA. This defect density could correspond to the defect solubility limit above which damage readily nucleates in Si.

5.3.4 Conclusion

In this study, we have shown that the DA time constant τ, changes with choice of t_{on} as the result of (1) a change in the effective time between ion impacts into L_d-defined regions and (2) a change in the super-cascade density within a single pulse. The former is an artifact of the choice of t_{on} whereas the latter is a reflection of the actual defect physics. By accounting for the effective time between ion impacts into L_d-defined regions, we isolated 2 in a time constant termed τ_{impact}. Below the critical temperature (T_c), which marks a change in the dominant processes of DA in Si, τ_{impact} was shown to decrease slightly with increasing t_{on} below $t_{on}^{L_d}$. Above $t_{on}^{L_d}$,

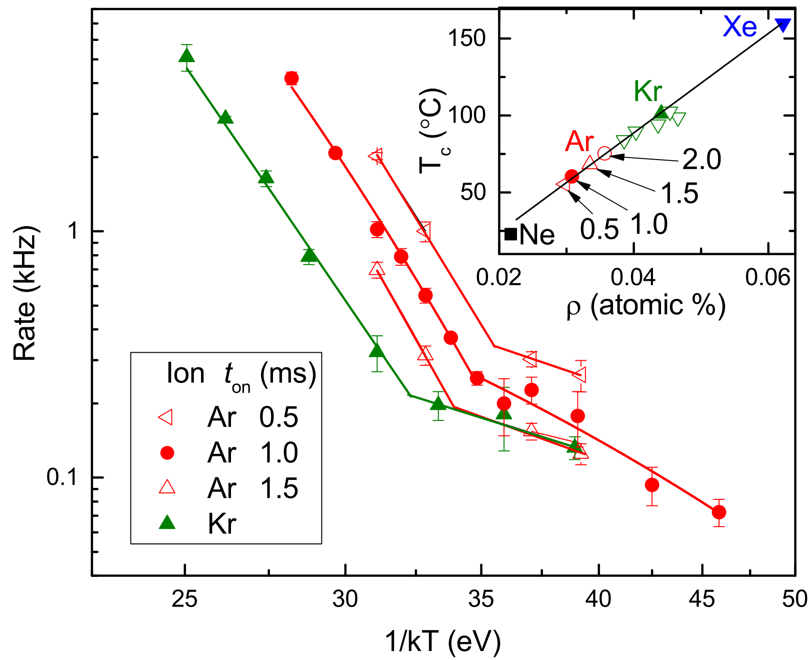

Figure 5.15: (Color online) Arrhenius plot of the DA rate. Straight lines show results of linear fitting, revealing activation energies of ~ 0.4 eV and ~ 0.1 eV. The inset shows an Arrhenius plot of the cascade density [83] at $R_{cut} = 20$nm revealing an activation energy of 0.1 eV.

τ_{impact} was found to increase with increasing t_{on}. Above $t_{on}^{L_d}$ multiple impacts are occurring into L_d-defined regions within every pulse leading to a significant increase in the super-cascade density which could lower the portion of mobile defects able to participate in intercascade DA causing an increase in 2nd order τ. At T above an ions T_c and below $t_{on}^{L_d}$, τ_{impact} was found to be approximately constant with increasing t_{on}. However, above $t_{on}^{L_d}$, τ_{impact} is shown to increase rapidly. This suggest that the influence of super-cascade density on the defect lifetime is minimal for $T > T_c$ and $t_{on} < t_{on}^{L_d}$. Finally, T_c was found to increase linearly with increasing super-cascade density within a given pulse.

6. RADIATION DEFECT DYNAMICS IN SIC*

Silicon carbide (SiC) is an important material for electronics [72, 84] and nuclear materials [71, 85] technologies. For both of these applications, the fundamental understanding of radiation damage processes is highly desirable, particularly for practically-relevant irradiation at room temperature (T) and above. For such irradiation conditions, all three main commonly available polymorphs of SiC ($3C$, $4H$, and $6H$) exhibit pronounced dynamic annealing (DA), [86–96] which refers to migration, recombination, and clustering of radiation-generated point defects *during* irradiation. The degree of DA increases with increasing sample T. This is evidenced as a reduction in the level of stable post-irradiation disorder or as an increase in the ion dose required to reach a certain level of disorder with increasing T. [86–90, 92, 96] The DA also manifests as a dose rate dependence of damage (with all the other irradiation conditions being constant). [91–93, 95] However, due to complexity of radiation defect interaction processes and the lack of direct experimental methods to study them, mechanisms of DA in SiC remain elusive. Indeed, physically very different models of point defect interaction can describe the same experimental T-dependencies of the amorphization dose. [97] More sophisticated measurements of radiation defect dynamics are needed to unravel the underlying mechanisms.

---

* Portions of this work are reprinted from Applied Physics Letters, Vol 106 / Issue 20, J. B. Wallace, L. B. Bayu Aji, L. Shao, S. O. Kucheyev, "Time constant of defect relaxation in ion-irradiated 3 C-SiC", Pages No. 202102, Copyright (2015), with the permission of AIP Publishing.

* Portions of this work are reprinted from Scientific Reports, Vol 6, L. B. Bayu Aji, J. B. Wallace, L. Shao, S. O. Kucheyev, "Non-monotonic temperature dependence of radiation defect dynamics in silicon carbide", Pages No. 30931, Copyright (2016), under the Creative Commons Attribution 4.0 International License.

6.1 Time constant of defect relaxation in ion-irradiated 3*C*-SiC

Previous studies of radiation effects in 3*C*-SiC have revealed a strong (close to exponential) temperature dependence of the amorphization dose for temperatures above ~ 0 °C, and a weak dependence at lower temperatures. [88–90, 97, 98] With increasing sample temperature, the amorphization dose increases, [88–90,97,98] indicating that ballistically-generated defects experience more efficient dynamic annealing, involving migration and interaction (i.e., clustering and recombination) of point defects. For such a regime with pronounced dynamic annealing, damage accumulation is often dominated by intra- and/or inter-cascade defect interaction processes, with the efficiency of the formation of stable lattice defects depending on instantaneous concentrations of interacting (unstable) point defects during irradiation. Dynamic effects significantly complicate radiation damage processes and limit predictability of most of the phenomenological damage buildup models developed. [99] Indeed, in a dynamic regime, radiation damage production depends on the density of collision cascades (determined by ion mass and energy) and on both average and instantaneous dose rates, reflecting the dynamic interaction of defects generated in different collision cascades.

No previous experimental studies of radiation defect dynamics in 3*C*-SiC was found. However, several reports have revealed strong dose rate effects in 4*H*-SiC at elevated temperatures. [91, 93, 100] For example, Kuznetsov et al. [91] have found that, for 100 keV Si ion irradiation of bulk 4*H*-SiC crystals at 100 °C, the level of stable lattice disorder ranges from full amorphization (i.e., a relative disorder level of 100%) to merely $\sim$ 20% depending on the dose rate (with all the other irradiation conditions unchanged). They have also shown that such dynamic dose rate effects become dominant somewhere in the temperature range between RT and

80 °C. Such conventional dose rate effect studies, [91, 93, 100] however, do not allow a straightforward extraction of the time and length constants of dynamic annealing. [15, 45] Speculative assumptions about the explicit defect interaction processes are required in order to separate spatial and temporal information in the analysis of dose rate effect data. [10] Moreover, results for $4H$-SiC cannot be readily extrapolated to $3C$-SiC due to the differences that are expected in dynamic radiation defect processes in these two materials at elevated temperatures. Indeed, the type and energetics of both point and extended defects, which play the dominant role in dynamic annealing processes, depend on the lattice structure.

In this section, the dynamics of radiation defects in $3C$-SiC bombarded at 100 °C with 500 keV Ar ions is studied using the pulsed-ion-beam method. [15, 45] Results reveal pronounced dynamic annealing in $3C$-SiC under these irradiation conditions, with a characteristic time constant of ~ 3 ms and a dynamic annealing efficiency of $\sim 40\%$ for both sublattices of $3C$-SiC.

6.1.1 Experimental

In this study, single-crystal epilayers of (001) $3C$-SiC epitaxially grown on 3-inch-diameter Si substrates at NOVASiC are used. The epilayers had a thickness of $\gtrsim 2$ μm. Wafers were cleaved to $\sim 5 \times 40$ mm^2 strips. The crystal quality of as-received films was verified by measuring a minimum 2 MeV He ion channeling yield of $\sim 1.5\%$, consistent across the wafer. To improve thermal contact, the samples were attached to a Ni sample holder with silver paste. Temperature was measured by two thermocouples attached to the sample holder at the opposite ends of the sample matrix. The thermocouples were thermally anchored with silver paste. Ion-beam heating effects were negligible ($\lesssim 0.1$ °C) for the dose rate and ion energy used in this experiment. The temperature of the sample holder, measured by the thermocouples, increased by

~ 0.2 °C for the longest irradiation run with a continuous ion beam (i.e., the case with the maximum heat load). Beam heating was estimated with assumptions of steady state one-dimensional heat transport across the sample thickness with a homogeneous generation term at the sample surface. Films were bombarded at 100 ± 1 °C with 500 keV $^{40}Ar^{+}$ ions at 7° off the [100] direction to minimize channeling effects. The 4 MV ion accelerator (National Electrostatics Corporation, model 4UH) at Lawrence Livermore National Laboratory was used for both ion irradiation and ion beam analysis.

As in previous pulsed beam experiments, [15, 45] all irradiations were performed in a broad beam mode rather than with rastered beams. The central portion of the beam, estimated to be wider than ~ 15 mm in diameter (measured with a spinning-wire-based beam profile monitor and by making burn marks on kapton targets), was selected with an $\sim 4 \times 5$ mm^2 final beam defining aperture. A small triangle wave (with frequency of ~ 11 Hz and ~ 3 Hz in the horizontal and vertical directions, respectively) was applied to electrostatic deflection plates to improve beam uniformity. This wave extended the beam width by only $\sim 10\%$ compared to the unperturbed beam. Beam pulsing was achieved by applying high voltage pulses to a pair of parallel plates deflecting the beam in the vertical direction off the final beam defining aperture. A total dose of 3.5×10^{14} cm^{-2} was split into a train of $\sim 18,400$ equal pulses, each with an instantaneous dose rate F_{on} of $\sim 1.9 \times 10^{13}$ cm^{-2} s^{-1} and duration $t_{on} = 1$ ms (and, hence, with a dose per each pulse, $F_{on} \times t_{on}$, of $\sim 1.9 \times 10^{10}$ cm^{-2}, corresponding to an average distance between ion impacts on the sample surface in each pulse, $\frac{1}{\sqrt{F_{on} t_{on}}}$, of ~ 73 nm). The adjacent pulses were separated by t_{off}, which was varied between 1 and 50 ms. The inset in Fig. 6.1 shows a schematic of the time dependence of the instantaneous dose rate and defines pulsing parameters t_{on}, t_{off}, and F_{on}.

The dependence of lattice damage in both Si and C sublattices on t_{off} was studied *ex-situ* at RT by ion channeling. Depth profiles of lattice disorder in the Si sublattice were measured with 2 MeV $^{4}He^{+}$ ions incident along the [100] direction and backscattered into a detector at 164° relative to the incident beam direction. Spectra were analyzed with one of the conventional algorithms [18] for extracting the effective number of scattering centers (referred to below as "relative disorder") in the Si sublattice. The level of bulk disorder was defined as an average and error bars as the standard deviation over 20 channels ($\sim$ 38 nm) around the bulk peak maximum. For measuring damage in the C sublattice by channeling, the same scattering geometry was used, but with 4.3 MeV $^{4}He^{2+}$ ions, taking advantage of the $^{12}C(\alpha,\alpha)^{12}C$ resonant reaction at $\sim$ 4.28 MeV that has an $\sim$ 100-fold larger scattering cross section compared to Rutherford. [19] Relative disorder in the C sublattice was defined as $\frac{Y - Y_{virgin}}{Y_{random} - Y_{virgin}}$, where Y, Y_{virgin}, and Y_{random} are channeling yields at the resonant energy from the sample of interest, an un-irradiated sample, and amorphous SiC, respectively. The spot size of both He beams was $\sim 1.5\times1.5$ mm^2. Doses and dose rates were limited to $\sim 2\times10^{16}$ cm^{-2} and $\sim 3\times10^{13}$ cm^{-2} s^{-1}, respectively, for both He beams.

6.1.2 Results and discussion

Figure 6.1(a) shows representative depth profiles of relative disorder in the Si sublattice for bombardment with continuous (t_{off} = 0 ms) and pulsed (t_{off} = 5 and 50 ms) beams of 500 keV Ar ions. Figure 6.1(b) shows channeling spectra of resonant scattering, reflecting damage in the C sublattice in the same samples as in Fig. 6.1(a). Depth profiles of Fig. 6.1(a) are bimodal, with distinct surface and bulk peaks. The surface peak is much smaller than the bulk peak, reflecting a limited role of the (001) 3*C*-SiC surface in damage accumulation for these irradiation

conditions. The bulk peak is situated at ~ 300 nm. This depth is close to the peak of the nuclear energy loss profile of 500 keV Ar ions. [20, 73] The depth profile of vacancies was calculated with the TRIM code (version SRIM-2013.00, full cascade calculations) [20] with an atomic concentration of SiC of 9.64×10^{22} atoms cm^{-3} (Ref. [71]) and threshold energies for atomic displacements of 20 and 35 eV for C and Si sublattices, respectively. [73] For continuous beam bombardment, it is seen from Fig. 6.1(a) that the bulk damage peak level is $\sim 70\%$, and the shape of the damage–depth profile is close to that of ballistically-generated vacancies calculated with the TRIM code [20] and also shown in Fig. 6.1(a) by a dashed line. All these observations are consistent with a previous ion channeling study [90] of epilayers of $3C$-SiC irradiated at 100 °C with 360 keV Ar ions with an average dose rate of 2×10^{12} cm^{-2} s^{-1} that was not intentionally pulsed. Note that, in a typical ion irradiation experiment, unintentional beam pulsing for any given area on the sample occurs as a result of beam rastering. In this case, the instantaneous dose rate depends not only on the rastering algorithm but also on the beam shape (focusing), which is difficult to control. Hence, only average dose rates are commonly quoted in radiation damage studies.

Figures 6.1(a) and 6.1(b) reveal that, for both sublattices, relative bulk disorder decreases with increasing t_{off}. This effect is better illustrated in Fig. 6.2, showing that, as t_{off} increases, the level of relative disorder in the bulk decreases from its initial value of $\sim 70\%$ to a saturation level of $\sim 40\%$ for $t_{off} \gtrsim 20$ ms. Within experimental errors, the data could be fitted reasonably well with either the first or second order kinetic decay equations (i.e., $\propto \exp(-\frac{t_{off}}{\tau})$ and $\propto (1 + \frac{t_{off}}{\tau})^{-1}$ decay processes, where τ is a characteristic defect relaxation time constant). Fitting curves for the Si sublattice with the first and second order rate equations with a nonlinear least-squares Marquardt-Levenberg algorithm are shown in Fig. 6.2 by dashed and

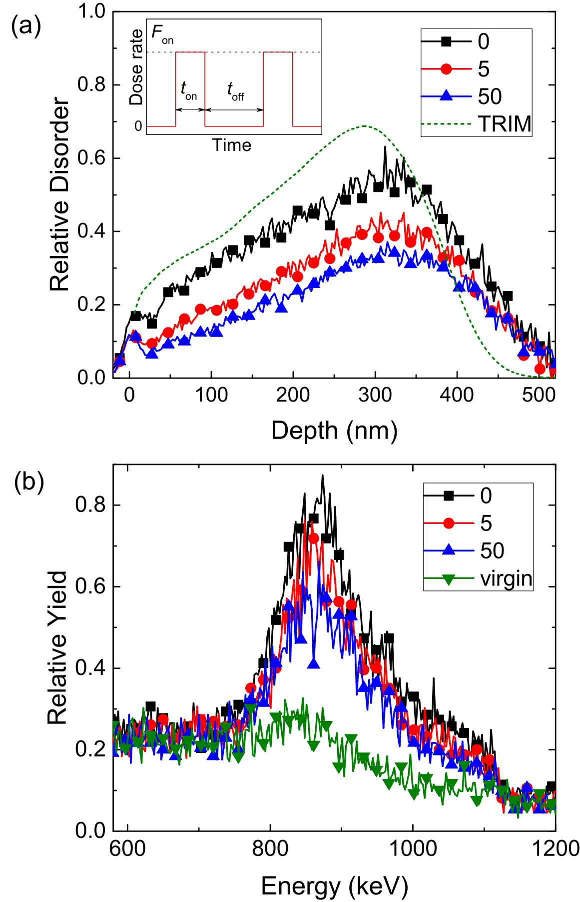

Figure 6.1: (Color online) Selected (a) depth profiles of relative disorder in the Si sublattice and (b) ion channeling spectra of the ^{12}C(α,α)^{12}C resonant scattering, reflecting damage in the C sublattice, for 3C-SiC bombarded at 100 °C with a pulsed beam of 500 keV Ar ions with different values of t_{off} (given in the legend) and all the other parameters fixed (the total dose = 3.5×10^{14} cm^{-2}, t_{on} = 1 ms, and F_{on} = 1.9×10^{13} cm^{-2} s^{-1}). For clarity, only every 10th experimental point is depicted. Also shown by a dashed line in (a) is the normalized TRIM-code predicted profile of lattice vacancies for 500 keV Ar ion irradiation of SiC. The projected range and straggling of Ar ions are 329 and 66 nm, respectively. The inset in (a) is a schematic of the time dependence of the instantaneous dose rate for pulsed beam irradiation, defining t_{on}, t_{off}, and F_{on}.

solid lines, respectively. For the Si sublattice, the first and second order fits yield τ values of 4.6 ± 0.8 ms and 3.2 ± 0.3 ms and a dynamic annealing efficiency ξ of 38% and 44%, respectively. Corresponding values for the C sublattice are τ of 5.0 ± 1.7 ms and 3.2 ± 1.2 ms and ξ of 44% and 48%. The dynamic annealing efficiency is defined as $\xi = \frac{n_0 - n_\infty}{n_0}$, where n_0 and n_∞ are relative disorder levels for the case of continuous beam irradiation with $t_{off} = 0$ ms and for the case of $t_{off} >> \tau$ when the damage level is saturated at its lowest value.

An important observation from Figs. 6.1 and 6.2 is that, within experimental errors, dynamic annealing parameters are the same for both Si and C sublattices. This implies a strong coupling of defect relaxation processes in the two sublattices. No previous experimental studies of radiation defects in different sublattices of 3*C*-SiC were found in literature. the result is, however, consistent with predictions of a strong coupling of defects in the two sublattices reported in a recent *ab initio* molecular dynamics (MD) simulation study of point-defect-induced amorphization in 3*C*-SiC at 100 K by Jiang et al. [101] They [101] attributed the coupling of defect accumulation in the two sublattices to defect-induced mechanical instability, pointing to a fundamental difference between damage accumulation in elemental and compound semiconductors. Identical (within experimental errors) radiation damage buildup behavior in C and Si sublattices has also been reported in several ion channeling studies of bulk 4*H*-SiC and 6*H*-SiC crystals. [102–104] Although this points to some similarity between radiation processes in the three main polymorphs of SiC, more work is currently needed to understand the effect of SiC crystallography on radiation dynamics.

A τ of ~ 3 ms and a ξ of 44% measured in this section for 3*C*-SiC at 100 °C are smaller than the corresponding (second order kinetics) values of τ of ~ 6 ms and ξ of $\sim 80\%$ reported in the only other pulsed beam study of τ to date for Si

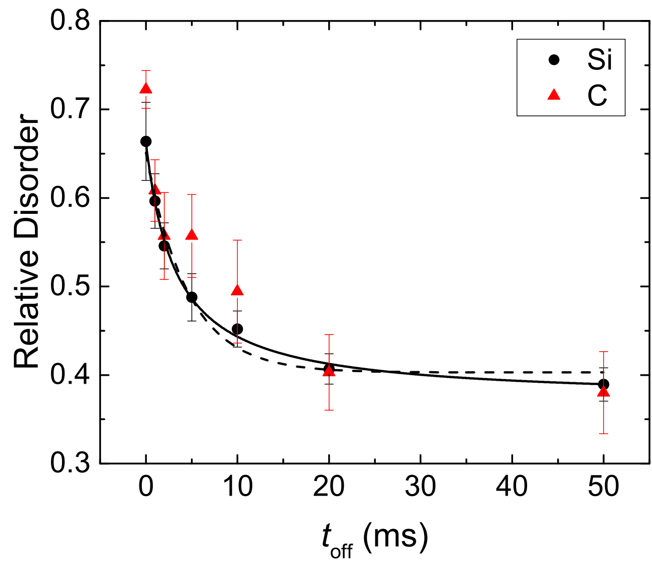

Figure 6.2: (Color online) Relative bulk disorder in Si and C sublattices (as indicated in the legend) of 3*C*-SiC bombarded at 100 °C with a pulsed beam of 500 keV Ar ions as a function of the passive portion of the beam cycle (t_{off}). Fitting curves of the data for the Si sublattice with the first and second order rate equations are shown by dashed and solid lines, respectively.

bombarded at RT with 500 keV Ar ions. [45] The difference between τ values for $3C$-SiC and Si is not unexpected, as radiation damage accumulation processes often vary dramatically between different materials and irradiation conditions. In fact, it appears to be coincidental that τ values in Si at RT and $3C$-SiC at 100 °C are of the same order of magnitude, given that even small changes in defect migration and interaction barriers could result in a large difference in defect relaxation time scales.

More relevant, the value of τ measured in this section for $3C$-SiC at 100 °C is significantly larger than the upper limits of τ of 10 ps predicted in MD simulations [73, 105] and 10 μs estimated by Rong et al. [105] in their kinetic Monte Carlo (KMC) simulations of 10 keV Si ion irradiation in the temperature range of $100 - 1000$ K. Such a gross underestimation of τ in MD simulations (by 9 orders of magnitude!) [73, 105] is not surprising, given that MD is computationally unsuitable for modeling the long time-scale evolution of defects. The still significant underestimation of τ in previous KMC simulations [105] (by 3 orders of magnitude) points to the currently limited understanding of radiation dynamics in SiC. Since defect relaxation dynamics measured in pulsed-ion-beam experiments reflects the parameters describing migration and interaction processes of point defects, this data could provide critical validation for future modeling efforts of radiation damage based on KMC and rate equation approaches. Finally, the τ value measured in this section is much lower than a τ of $\sim$ 100 s estimated by Posselt et al. [106] for bulk $6H$-SiC crystals based on dose rate effect measurements for 70 keV Ga ion irradiation at RT and 225 °C. Such a large gap between different previous estimates of τ demonstrates a currently limited understanding of radiation dynamics in the SiC materials system and points to a need for further systematic studies.

6.1.3 Conclusion

In summary, the pulsed-ion-beam method [45] was used for quantitative measurements of the dynamic annealing time constant (τ) in 3C-SiC. A τ of $\sim$ 3 ms or $\sim$ 5 ms (with assumptions of the second or first order kinetic decay, respectively) and a dynamic annealing efficiency of $\sim$ 40% have been measured for defects in both the Si and C sublattices of 3C-SiC irradiated at 100 °C with 500 keV Ar ions. This has demonstrated the applicability of the pulsed-ion-beam technique [45] for studies of radiation defect dynamics in materials other than Si. Furthermore, statistically indistinguishable radiation dynamics parameters for C and Si sublattices demonstrate a close temporal and spatial coupling of damage accumulation between the two sublattices of SiC. These results have direct and important implications for understanding and predicting radiation damage in 3C-SiC at elevated temperatures and demonstrate that taking into account radiation defect dynamics is essential in the development of physically sound, predictive models of radiation damage buildup (such as MD, KMC, and/or rate theory).

6.2 Temperature dependence of radiation defect dynamics in $4H-$SiC

This section focuses on the $\tau(T)$ dependence in 4H-SiC bombarded with energetic Ar ions in the T range of 25 – 250 °C. Results reveal a non-monotonic $\tau(T)$ dependence with a maximum of $\sim$ 5 ms at $\sim$ 100 °C, reflecting a change in the dominant DA mechanism at $\sim$ 100 °C. This result has important practical implications since design strategies for radiation-tolerant materials are determined by the dominant defect formation and DA processes.

6.2.1 Experimental

High purity semi-insulating (0001) 4H-SiC single crystals (with a diameter of 100 mm, a resistivity of $\gtrsim 10^9$ Ω cm, and a nominal micropipe density of < 60 cm^{-2}), obtained from Cree, Inc., were bombarded with 500 keV Ar ions at 7° off the [0001] direction in the T range of $25-250$ °C. The crystal quality of as-received 4H-SiC wafers was verified by measuring a minimum 2 MeV He ion channeling yield of $\sim$ 1.6%, consistent across the wafer. The 4 MV ion accelerator (National Electrostatics Corporation, model 4UH) at Lawrence Livermore National Laboratory was used for both ion irradiation and ion beam analysis. To improve thermal contact, the samples were attached to the Ni sample holder with conductive Ag paste. The sample holder temperature was monitored with a chromel/alumel thermocouple (with an accuracy of ± 1 °C). All irradiations were performed in a broad beam mode. [45] Irradiated areas were $\sim 4 \times 5$ mm^2. Ion beam pulsing was achieved by applying high voltage pulses to a pair of parallel plates deflecting the beam in the vertical direction off the final beam defining aperture so that the total dose was split into a train of equal square pulses each with an F_{on} of $\sim (1.7 \pm 0.05) \times 10^{13}$ cm^{-2} s^{-1} and duration $t_{on} = 1$ ms. The adjacent pulses were separated by time t_{off}, which was varied between 1 and 100 ms. For irradiation at $T \gtrsim 200$ °C that required larger total doses, t_{off} was limited to 20 ms, which was still much larger than the DA time constants at these Ts. A more detailed description of the experimental arrangement can be found elsewhere. [46, 95]

The dependence of lattice damage on t_{off} was studied *ex-situ* at room temperature by ion channeling. Depth profiles of lattice disorder in the Si sublattice were measured with 2 MeV He ions incident along the [0001] direction and backscattered into a detector at 164° relative to the incident beam direction. The spot size of the

He beam was $\sim 1.5 \times 1.5$ mm^2. Spectra were analyzed with one of the conventional algorithms [18] for extracting the effective number of scattering centers (referred to below as "relative disorder"). Values of averaged bulk disorder (n) were obtained by averaging depth profiles of relative disorder over 10 channels (~25 nm) centered on the bulk damage peak maximum. Error bars of n are standard deviations. Error bars of τ, ξ, and the DA rate are standard errors of the non-linear fitting described above.

The depth profile of vacancies was calculated with the TRIM code (version SRIM-2013.00, full cascade calculations) [20] with an atomic concentration of SiC of 9.64×10^{22} atoms cm^{-3} [71] and threshold energies for atomic displacements of 20 and 35 eV for C and Si sublattices, respectively. [73] To convert to DPAs (at the depth corresponding to the maximum of the nuclear energy loss profile), ion doses in 10^{14} Ar ions cm^{-2} are multiplied by 0.0898. The projected range and straggle of 500 keV Ar ions are ~ 320 and ~ 70 nm, respectively.

6.2.2 Results and discussion

Figure 6.3 shows an exponential T dependence of the dose required to achieve an averaged bulk disorder level (n) of 0.7 (with $n = 1$ corresponding to complete amorphization) for continuous beam irradiation (i.e., $t_{off} = 0$) of 4H-SiC. Such a dose increases from 0.2 to 4.3 displacements per atom (DPA) when T is increased from 25 to 250 °C, reflecting the thermally activated nature of DA processes. An increase in the dose required to reach a certain disorder level with increasing T is expected. [86–90, 92, 94, 96] Indeed, at higher Ts, point defects have higher diffusivity and experience more efficient vacancy-interstitial recombination. It should, however, be noted that the doses revealed by Fig. 6.3 are smaller than those reported in the previous studies of SiC [86–90, 92, 94] due to a larger dose rate used in the present

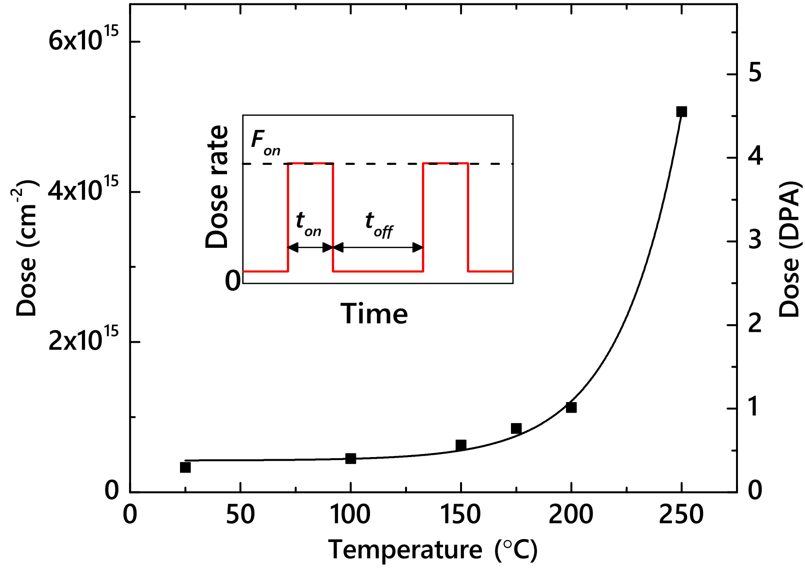

Figure 6.3: (Color online) Temperature dependence of the ion dose required to reach a damage level of 0.7 in 4H-SiC bombarded with a continuous beam (i.e., $t_{off} = 0$) of 500 keV Ar ions with a dose rate of 1.7×10^{13} cm^{-2} s^{-1}. The solid line is an exponential fit to the data. The inset is a schematic of the time dependence of the instantaneous dose rate for pulsed beam irradiation, defining t_{on}, t_{off}, and F_{on}.

work. As discussed in detail in recent systematic study of the damage buildup in 3C-SiC, [96] this highlights the dominant role of DA in the formation of stable post-irradiation damage in SiC at elevated Ts. Based on damage buildup data such as shown in Fig. 6.3, ion doses were chosen for pulsed beam experiments at different Ts so that, for $t_{off} = 0$ (i.e., continuous beam irradiation), n is in the range of $0.6 - 0.8$, which is a nonlinear regime of damage buildup with pronounced DA. [9, 95, 96]

Figure 6.4 shows representative depth profiles of relative disorder for bombardment of 4H-SiC with continuous or pulsed beams at Ts of 25, 100, and 250 °C. Each panel of Fig. 6.4 shows data for cases when all the irradiation conditions are kept constant except for t_{off}. It is seen that, for all three Ts shown, depth profiles are bimodal, with the first small peak at the sample surface and the second major peak

in the crystal bulk. The bulk peak (with a height of n) is centered on $\sim$ 300 nm, which corresponds to the maximum of the nuclear energy loss profile for 500 keV Ar ions. It is also seen from Fig. 6.4 that n decreases with increasing t_{off} for all three Ts. The reduction in n with increasing t_{off} occurs in all measurements at different Ts. Figure 6.4 further shows that the degree of reduction in n with increasing t_{off} increases dramatically with increasing T. For example, for $T = 250$ °C [Fig. 6.4(c)], an increase in t_{off} from 0 to 5 ms results in an $\sim$ 2.5-fold reduction in n. In contrast, the damage level at the sample surface is independent of t_{off}, suggesting different mechanisms of bulk and surface disordering. [34, 45, 46, 95]

Figure 6.5 summarizes $n(t_{off})$ dependencies for all the Ts of this study ($25 - 250$ °C). It reveals that n monotonically decreases with increasing t_{off} in all these cases. Solid lines in Fig. 6.5 are fits of the data via the Marquardt-Levenberg algorithm with the second order decay equation ($n(t_{off}) = n_\infty + \frac{n(0)-n_\infty}{1+\frac{t_{off}}{\tau}}$). Here, n_∞ is relative disorder for $t_{off} >> \tau$. All the $n(t_{off})$ dependencies from Fig. 6.5 obey the second order decay better than the first order (i.e., exponential) decay.

The $\tau(T)$ dependence is shown in Fig. 6.6, revealing a non-monotonic behavior, when τ first rapidly increases with T, reaches a maximum at 100 °C, followed by a monotonic decrease for $T \gtrsim 100$ °C. Also plotted in Fig. 6.6 is the T dependence of the DA efficiency (ξ): [45] $\xi = \frac{n(0)-n_\infty}{n(0)}$. As discussed in detail recently, [46] for the choice of F_{on} and t_{on}, ξ is the magnitude of the dose rate effect; i.e., the difference between n for continuous beam irradiation with dose rates of $F = F_{on}$ and $F \to 0$. It is seen from Fig. 6.6 that, in contrast to the $\tau(T)$ dependence, ξ increases monotonically with T in the T range of $25 - 175$ °C. At $\sim$ 175 °C, ξ reaches a maximum of $\sim$ 80%, followed by a slight decrease at 250 °C. Hence, both $\tau(T)$ and $\xi(T)$ dependencies of Fig. 6.6 are non-trivial, reflecting the complexity of defect interaction processes.

Values of τ revealed by Fig. 6.6 are in the range of $\sim 1 - 5$ ms. These are

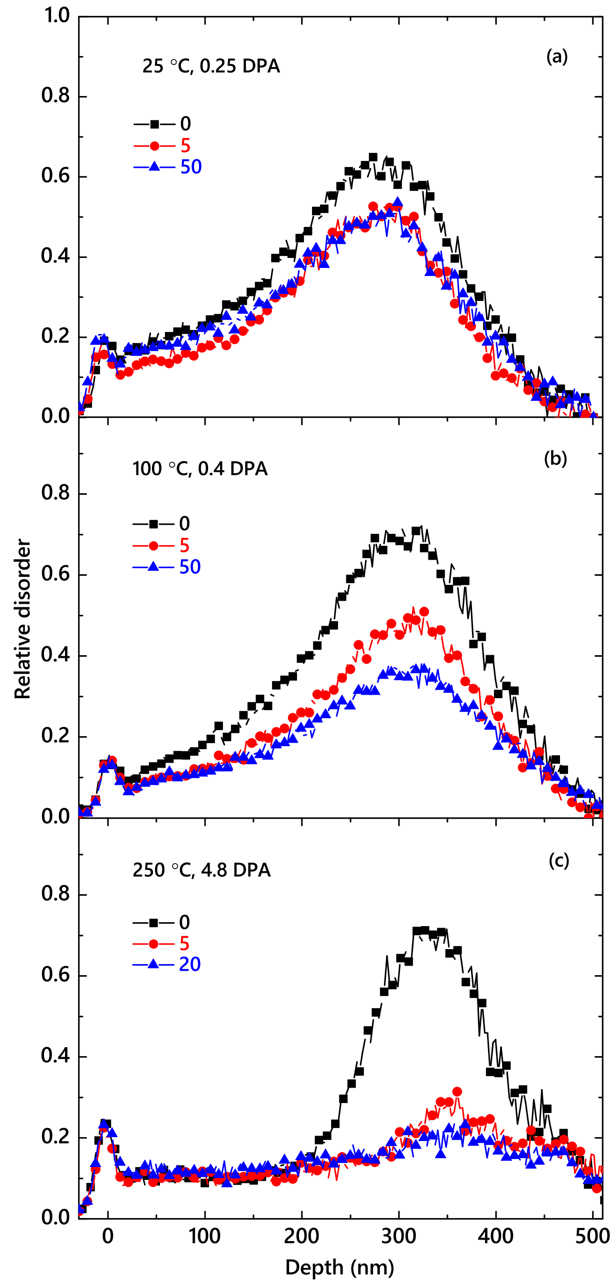

Figure 6.4: (Color online) Selected depth profiles of relative disorder in 4H-SiC bombarded with a pulsed beam of 500 keV Ar ions with $F_{on} = 1.7 \times 10^{13}$ cm^{-2} s^{-1}, $t_{on} = 1$ ms, and different t_{off} values, given in legends (in units of ms), at different temperatures and total doses, also shown in the legends. For clarity, only every 5th experimental point is depicted.

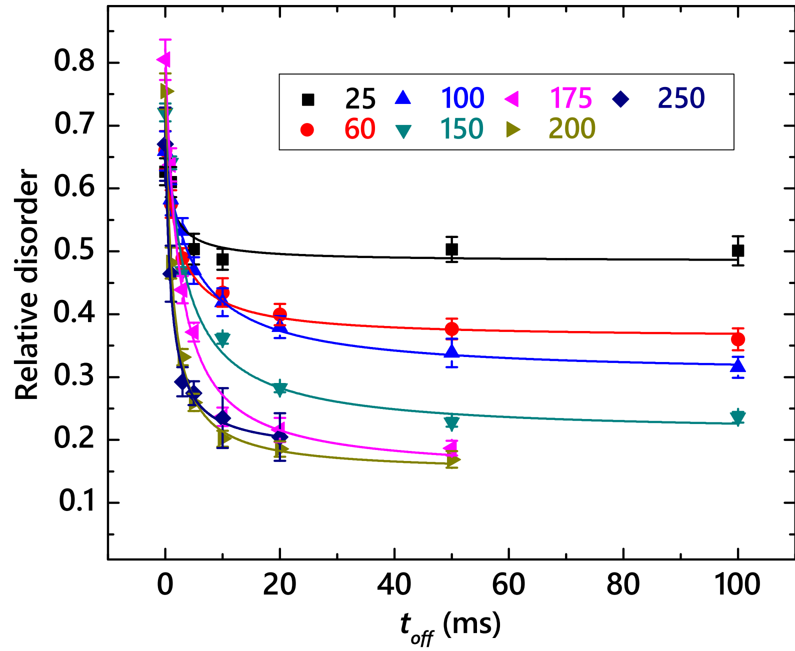

Figure 6.5: (Color online) Level of relative bulk disorder in 4H-SiC bombarded with 500 keV Ar ions with $F_{on} = 1.7 \times 10^{13}$ cm^{-2} s^{-1} and $t_{on} = 1$ ms as a function of the passive portion of the beam duty cycle (t_{off}) at different temperatures, given in the legend (in units of °C). Fitting curves of the data with the second order decay equation are shown by solid lines.

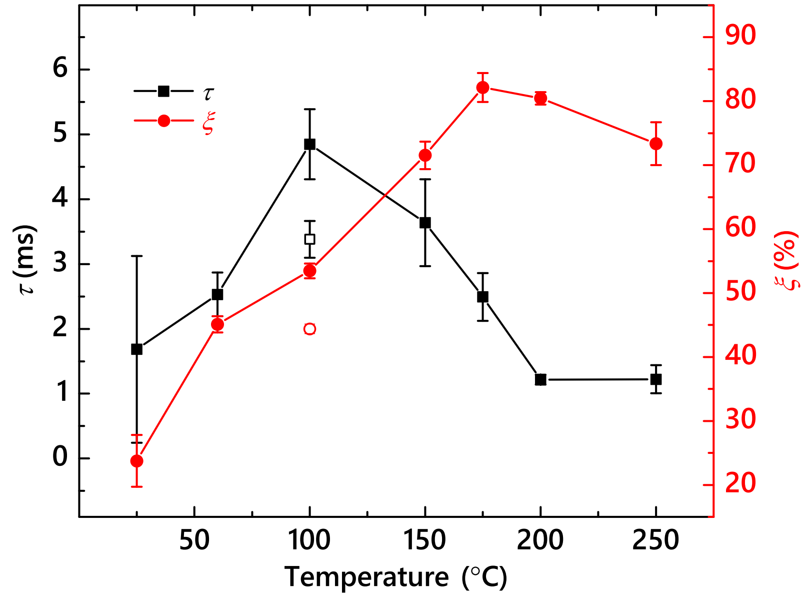

Figure 6.6: (Color online) Closed symbols: temperature dependencies of the effective time constant of DA (τ) and the DA efficiency (ξ) for 4H-SiC bombarded with 500 keV Ar ions with $F_{on} = 1.7 \times 10^{13}$ cm^{-2} s^{-1} and $t_{on} = 1$ ms. Open symbols show data points for 3C-SiC irradiated at 100 °C with 500 keV Ar ions with $F_{on} = 1.9 \times 10^{13}$ cm^{-2} s^{-1} and $t_{on} = 1$ ms, taken from Ref. [95].

orders of magnitude larger than the predictions of molecular dynamics (MD) and kinetic Monte Carlo simulations discussed in section 6.1. [95] This highlights both the well-known limitations of MD to model long-time defect evolution and the currently limited understanding of radiation defect dynamics in SiC. Interestingly, Fig. 6.6 also shows one data point available for 3*C*-SiC at 100 °C (taken from section 6.1 [95]), revealing a larger τ for 4*H*-SiC than for 3*C*-SiC. This finding is not unexpected, given that DA processes depend on the type and properties of lattice-structure-specific point and extended defects. [95,96] Values of τ for SiC (Fig. 6.6) are also comparable to those for Si measured previously for room T bombardment with different ions ($\sim 4 - 13$ ms). [45,46] Future theoretical studies of defect interaction bench-marked against the pulsed beam data are needed to find out if such similarity in τ values reflects similarity in defect relaxation processes in different materials. Moreover, further systematic measurements of the $\tau(T)$ dependencies for 3*C*-SiC and 6*H*-SiC will be interesting, revealing similarities and differences in DA of the three main commonly available SiC polymorphs.

A non-monotonic $\tau(T)$-dependence of Fig. 6.6 reveals the existence of a transition temperature (T_r) of $\sim$ 100 °C. Such a T_r of 100 °C is not evident from the T dependence of the damage buildup (as shown in Fig. 6.3 and in numerous previous studies [86–90, 92, 96]). Neither is it revealed by the $\xi(T)$ dependence that, as mentioned above, reflects the T dependence of the dose rate effect, also studied previously in traditional measurements with continuous ion beams (or unintentionally scanned beams due to rastering). [91,92] A special role of $T \sim 100$ °C has, however, been noted in a number of previous studies of all three main polymorphs of SiC: 4*H*-SiC, [93] 6*H*-SiC, [107–110] and 3*C*-SiC, [111–114] evidenced either as the onset of post-irradiation defect annealing, [108–113] as a rapid decrease in the cross-section of damage production, [107] as a qualitative change in the radiation resistance of

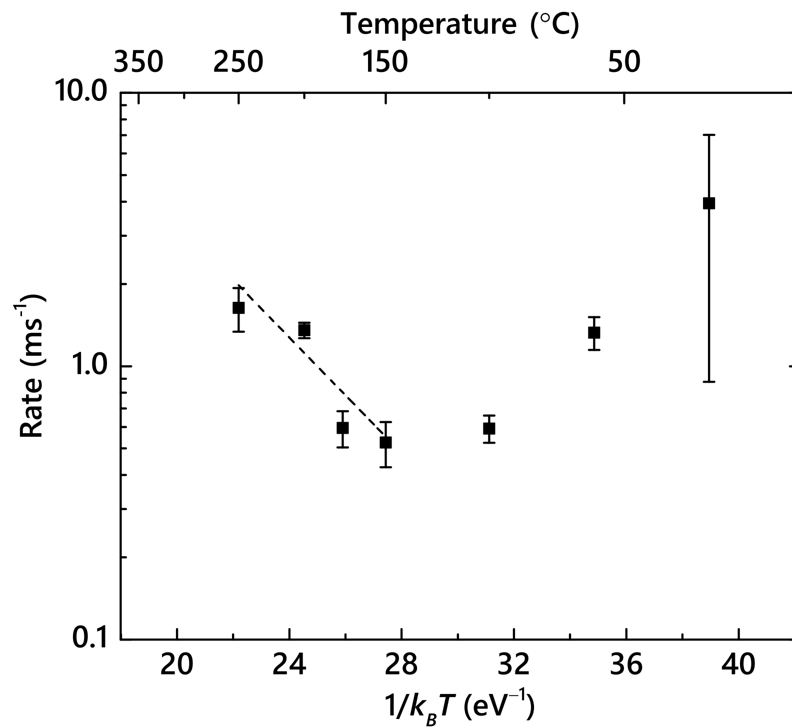

Figure 6.7: Arrhenius plot of the DA rate defined as $1/(\tau(n(0) - n_{inf}))$ for a second order decay process. The straight line shows results of linear fitting, revealing an activation energy of 0.25 ± 0.05 eV for the temperature range of $150 - 250$ °C.

nanocrystalline SiC, [114] or as a maximum of the concentration of open-volume defects monitored by positron annihilation spectroscopy. [93] The non-monotonic $\tau(T)$-dependence of Fig. 6.6 unambiguously shows that qualitatively different defect relaxation processes are dominant above and below a transition temperature (T_r) of ~ 100 °C.

In order to better understand the mechanism of DA, in Fig. 6.7, the $\tau(T)$ dependence from Fig. 6.6 was replotted in Arrhenius coordinates, with the DA rate defined as $\frac{1}{\tau(n(0)-n_\infty)}$, and with k_BT having the usual meaning. For the second order decay process ($\frac{d(n-n_\infty)}{dt} = -R(n-n_\infty)^2$), the decay time constant (τ) depends on the initial concentration of mobile defects, and the decay rate is $R = \frac{1}{\tau(n(0)-n_\infty)}$. A regime with a negative effective activation energy (E_a) is clearly seen in Fig. 6.7 for $T \lesssim 100$ °C. A negative E_a combined with an increase in ξ for $T \lesssim 100$ °C (see Fig. 6.6) could suggest the dominance of thermally activated processes of defect detrapping. Indeed, processes of defect trapping and de-trapping that do not involve defect recombination result in an increase in the effective lifetime of mobile defects and, hence, a reduced DA rate characterized by the negative E_a.

At $T \gtrsim 100$ °C, thermally activated processes of defect recombination appear to dominate when τ decreases with increasing T. An Arrhenius regime with a positive E_a is seen for the T range of $150-250$ °C. Linear fitting of the data gives an E_a and a pre-exponential factor of 0.25 ± 0.05 eV and $(5.23 \pm 0.62) \times 10^2$ Hz, respectively. This E_a value is much smaller than an E_a of 1.3 eV obtained by Kuznetsov et al. [91] by the analysis of the T-dependence of the dose rate effect in the T range of $20-225$ °C based on the method proposed by Schultz and co-workers, [6] which is equivalent to the analysis of the $\xi(T)$ dependence of Fig. 6.6. Such an apparent inconsistency in E_a could be attributed to limitations of the method of Schultz et al. [6] Indeed, ξ (i.e., the magnitude of the dose rate effect) reflects the fraction of ballistically-

generated Frenkel defects that participate in DA processes for any given F_{on} rather than the *rate* of defect interaction. The E_a of ~ 0.25 eV is consistent with E_a values for 6H-SiC reported by Weber et al. [90, 115] from the analysis of the T dependence of the amorphization dose based on the empirical model of Morehead-Crowder. [116] Dedicated modeling and simulation studies are currently needed to better understand the atomistics of DA and to correlate the apparent activation energies measured here with energetic barriers of specific defect migration and interaction processes in SiC polymorphs.

6.2.3 Conclusion

In conclusion, the pulsed beam method was used to measure the temperature dependence of both the characteristic time constant (τ) and the efficiency of DA in the Si sublattice of 4H-SiC bombarded with 500 keV Ar ions in the temperature range of $25 - 250$ °C. Results have revealed a non-monotonic T-dependence of τ with a maximum at 100 °C, indicating a change in the dominant DA mechanism at ~ 100 °C. The Arrhenius regime in the T range of $150 - 250$ °C is described by an activation energy of ~ 0.25 eV. The details of radiation defect dynamics revealed in this work have important implications for understanding, predicting, and controlling radiation damage in SiC and for benchmarking future theoretical efforts.

7. DYNAMIC ANNEALING IN GE STUDIED BY PULSED ION BEAMS

7.1 Introduction

For the past decade, there has been renewed interest in the use of Ge for high-speed, low-power electronics. [117] Ion implantation is the preferred tool for selective-area doping of semiconductor devices. However, implantation of dopants is accompanied by the formation of lattice defects that strongly influence material properties. Hence, numerous recent studies have focused on ion implantation damage in Ge. [118–123]

It has been well established that radiation damage in Ge, particularly above room temperature, is dominated by so-called dynamic annealing (DA) processes. [118–129] These involve migration, recombination, and clustering of mobile point defects *during irradiation*. Such DA is commonly manifested as a dependence of stable lattice disorder on the dose rate and sample temperature (T). Despite previous efforts, [118–127, 129] the current understanding of DA in Ge is very limited, and some very basic questions about defect interaction remain unanswered. For example, after the thermalization of ballistic collision cascades, how long do mobile point defects survive and how far do they diffuse while participating in DA processes? Previous estimates of the defect relaxation time constant (τ) in Ge cover an astonishingly wide range of 12 orders of magnitude ($10^{-11} - 10^{1}$ s). [129, 130] No previous measurements of the effective diffusion length of mobile defects (L_d) in ion-bombarded Ge were found.

In this section the pulsed ion beam method [15–17, 45, 47, 48] is used to study the dynamics of radiation defect interaction in Ge bombarded with 500 keV Ar ions. The τ values of $\sim 10^{-4} - 10^{-2}$ s (monotonically decreasing with T) and an L_d of ~ 38 nm at 110 °C are measured. Furthermore, the $\tau(T)$ dependence reveals a change in

the dominant DA process at ~ 130 °C, and reveals the activation energies of the two dominant DA processes.

7.2 Experimental

Czochralski grown (100) Ge single crystals doped with Ga (with a resistivity of ~ 0.03 Ω cm) were bombarded with 500 keV $^{40}Ar^{+}$ ions at 7° off the [100] direction in the T range of $100 - 160$ °C. Previous studies [124–127] have found pronounced DA in this T range. To improve thermal contact, the samples were attached to the Cu sample holder with Ag paste. All irradiations were performed in a broad beam mode. [45] Ion beam pulsing was achieved by applying high voltage pulses to a pair of parallel plates deflecting the beam off the final beam defining aperture. The 4 MV ion accelerator (National Electrostatics Corporation, model 4UH) at Lawrence Livermore National Laboratory was used for both ion irradiation and ion beam analysis.

Similar to previous work throughout this dissertation, [16, 45, 47, 48] for τ measurements, the total ion fluence was split into a train of equal pulses, each with an instantaneous dose rate (F_{on}) of $\sim 1.5 \times 10^{13}$ cm^{-2} s^{-1} and duration (t_{on}) of 1 ms. Adjacent pulses in such τ measurements were separated by time t_{off}, which was varied between 0.2 and 50 ms. For L_d measurements, [15–17] the total fluence was delivered as a train of pulses with duration (t_{on}) varying between 0.2 and 1 ms, each with an instantaneous dose rate (F_{on}) of $\sim 4.3 \times 10^{13}$ cm^{-2} s^{-1}, separated by a t_{off} of 100 ms, which, as will be shown below, is much greater than the τ values. The inset in Fig. 7.1(a) shows a schematic of the time dependence of the instantaneous dose rate and defines the pulsing parameters (t_{on}, t_{off}, and F_{on}). A more detailed description of the experimental arrangement can be found elsewhere. [16, 45, 47, 48]

The dependence of stable lattice damage on t_{off} and t_{on} was studied *ex-situ* at room T by ion channeling. Depth profiles of lattice disorder were measured with 2

MeV $^4He^+$ ions incident along the [100] direction and backscattered into a detector at 164° relative to the incident beam direction. Spectra were analyzed with one of the conventional algorithms [18] for extracting the effective number of scattering centers (referred to below as "relative disorder"). Values of averaged bulk disorder (n), discussed below, were obtained by averaging depth profiles of relative disorder over 15 channels (corresponding to an $\sim$ 60-nm-wide region) centered on the maximum of the bulk damage peak. Error bars of n are standard deviations. Ion fluences in τ measurements at different Ts were chosen such that, for continuous beam irradiation, n was in the range of $0.5 - 0.8$ (with $n = 1$ corresponding to full amorphization). The nuclear energy loss profile was calculated with the TRIM code (version SRIM-2013.00) [20] with an atomic concentration of Ge of 4.4×10^{22} atoms cm^{-3} and a threshold energy for atomic displacements of 15 eV.

7.3 Results and discussion

Figure 7.1(a) shows representative depth profiles of relative disorder for bombardment with continuous ($t_{off} = 0$ ms) and pulsed ($t_{off} = 5$ and 20 ms) beams at $T = 110$ °C for τ measurements. Figure 7.1(b) shows corresponding profiles for bombardment with pulsed ($t_{on} = 0.2$, 0.3, and 0.5 ms) beams at $T = 110$ °C for L_d measurements. The depth profiles for all irradiations herein have qualitatively similar shapes. They exhibit a major peak in the crystal bulk centered on $\sim$ 270 nm, which corresponds to the maximum of the nuclear energy loss profile for 500 keV Ar ions. These observations are consistent with previous studies of radiation damage in Ge at room T. [119, 121, 123]

7.3.1 Diffusion length

Figure 7.1(b) shows that n increases with increasing t_{on}. These results are more clearly shown in Fig. 7.2, where n is plotted as a function of t_{on}. As discussed pre-

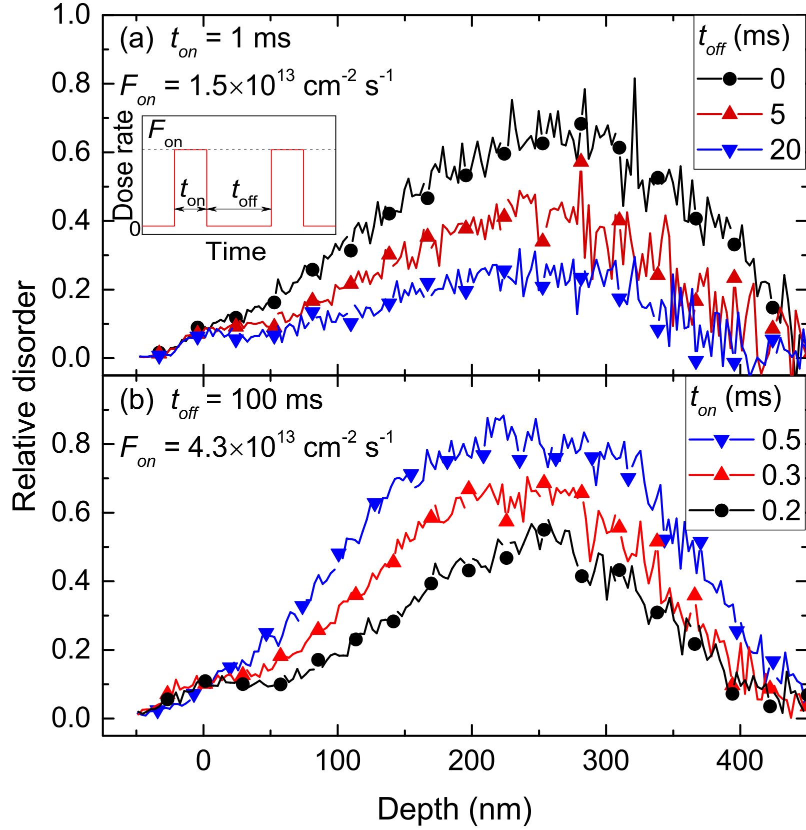

Figure 7.1: (Color online) Selected depth profiles of relative disorder in Ge bombarded at 110 °C with a pulsed beam of 500 keV Ar ions with F_{on}, t_{on}, and t_{off} given in the legends at total fluences of (a) 4.9×10^{13} cm^{-2} and (b) 7.5×10^{13} cm^{-2}. For clarity, only every 10th experimental point is depicted. Panel (a) is a pulsed beam measurement of τ, whereas (b) is a measurement of L_d. The inset in (a) is a schematic of the time dependence of the instantaneous dose rate for pulsed beam irradiation, defining t_{on}, t_{off}, and F_{on}.

viously, [15–17] in such measurements of $n(t_{on})$ dependencies with $t_{off} >> \tau$, the interaction between mobile defects generated in different collision cascades becomes pronounced when the average lateral distance between the centers of adjacent collision cascades *in each pulse* ($L_{overlap} = \frac{1}{\sqrt{F_{on} t_{on}}}$) is comparable to or smaller than the effective diffusion length of mobile defects: $L_{overlap} \lesssim 2L_d$ (with the average lateral dimensions of ballistic sub-cascades being much smaller than L_d). [15–17] Ion impacts obey Poisson statistics with a Poisson coefficient of $4L_d^2 F_{on} t_{on}$, where $4L_d^2$ is the effective area of a cascade after defect out-diffusion. If, for low t_{on} values, the efficiency of stable damage formation scales linearly with the displacement density, $n \propto 1 + 4L_d^2 F_{on} t_{on}$. This equation is used fit the linear portion of $n(t_{on})$ at low t_{on} values (the solid line in Fig. 7.2), revealing an L_d of $\sim 38 \pm 6$ nm. This L_d is larger than the value of ~ 10 nm in Ar-ion-bombarded 3C-SiC reported recently. [17] Interestingly, an L_d of ~ 38 nm is very similar to that found for Si under 500 keV Ar ion irradiation at room T. [16]

7.3.2 Time constant

Figure 7.1(a) also shows that n decreases with increasing t_{off}. This is better illustrated in Fig. 7.3, which summarizes $n(t_{off})$ dependencies for all the Ts studied at total fluences shown in the inset. It is seen from Fig. 7.3 that, for all the cases, n monotonically decreases with increasing t_{off}. Solid lines are fits of $n(t_{off})$ dependencies via the Marquardt-Levenberg algorithm [54] with a second order decay equation ($n(t_{off}) = n_\infty + \frac{n(0)-n_\infty}{1+\frac{t_{off}}{\tau}}$). Here, τ is the characteristic decay time constant, and n_∞ is relative disorder for $t_{off} >> \tau$. The best fits to $n(t_{off})$ dependencies alternate between the first order ($n(t_{off}) = n_\infty + (n(0) - n_\infty)\exp(-t_{off}/\tau_1)$) and second order decay equations across the T range studied. However, both first and second order fits have R-squared values > 0.9. Although it is tempting to associate the best fit-

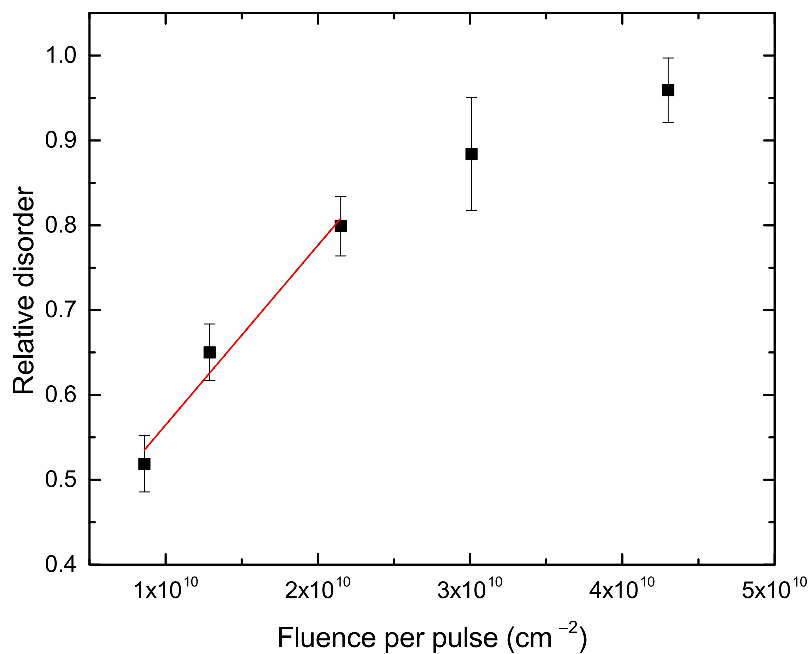

Figure 7.2: (Color online) Relative bulk disorder in Ge bombarded with a pulsed beam of 500 keV Ar ions with $F_{on} = 4.3 \times 10^{13}$ cm^{-2} s^{-1} and $t_{off} = 100$ ms as a function of the fluence per pulse ($F_{on}t_{on}$). Linear fitting, shown by the solid line, gives an effective diffusion length (L_d) of 38 ± 6 nm.

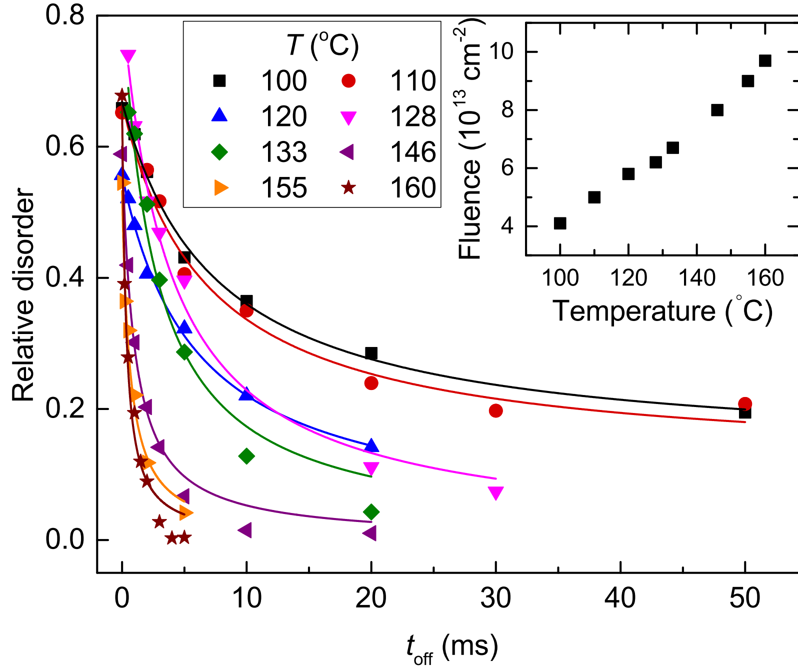

Figure 7.3: (Color online) Relative bulk disorder in Ge bombarded with a pulsed beam of 500 keV Ar ions with $F_{on} = 1.5 \times 10^{13}$ cm^{-2} s^{-1} and $t_{on} = 1$ ms as a function of the passive portion of the beam duty cycle (t_{off}) at different Ts given in the legend (in units of °C). Fitting curves with the second order decay equation are shown by solid lines. The inset shows the temperature dependence of the total ion fluence required to achieve a relative bulk disorder level of $\sim 0.5-0.8$ for continuous beam irradiation.

ting decay curves with some specific defect interaction processes, such assertions will require future detailed modeling work.

The $\tau(T)$ dependence is plotted in Fig. 7.4 (left axis), revealing a monotonic decrease with increasing T. Figure 7.4 (right axis) shows the T dependence of the DA efficiency (ξ), which is defined as follows: [16, 45] $\xi = (n(0) - n_\infty)/n(0)$. For the choice of the pulsing parameters, ξ is the magnitude of the dose rate effect, reflecting the fraction of mobile defects that participate in DA processes during continuous beam irradiation with a dose rate of F_{on}. [16] Figure 7.4 shows a monotonically increasing $\xi(T)$ dependence up to ~ 130 °C and saturation at $\xi \approx 100$ % for higher

Ts.

The fluence per pulse ($F_{on}t_{on}$) should be chosen to minimize intra-pulse defect interaction, while maximizing the inter-pulse interaction. [16] For $F_{on} = 1.5 \times 10^{13}$ cm^{-2} s^{-1} and $L_d = 38$ nm, this condition occurs for $t_{on} \lesssim t_{on}^{L_d} = \frac{1}{4L_d^2 F_{on}} \approx 1.2$ ms. [16] Hence, $t_{on} = 1$ ms is selected for τ measurements in this study. Moreover, for $t_{on} < t_{on}^{L_d}$, the effective time of defect relaxation during the passive portion of each pulse is $t_{off}^{effective} = (t_{on} + t_{off})\frac{t_{on}^{L_d}}{t_{on}}$. [16] The analysis of data from Fig. 7.3 as $n(t_{off}^{effective})$ gives τ values that differ only by $\sim 10\%$ from the τ values shown in Fig. 7.4. In addition, τ is independent of the choice of t_{on} (varied between 0.2 and 2.0 ms) when $F_{on}t_{on}$ is kept constant. All these observations are consistent with a recent detailed discussion of the choice of pulsing parameters. [16]

Figure 7.4 shows that the τ values are in the range of $\sim 10^{-4} - 10^{-2}$ s. These are much larger than a τ of $\sim 10^{-11}$ s predicted by molecular dynamics, [130] which is not unexpected given its computational limits at long time scales. The only experimental estimate of τ for Ge that was found is by Posselt et al. [129] for focused ion beam (channeled 30 keV Ga) irradiation. They [129] estimated a lower limit of 10 s at 20 °C and an upper limit of 10 ms at 250 °C. Extrapolating the measurements herein gives τ values of ~ 0.5 μs and 40 ms at 250 and 20 °C, respectively. This is consistent with the upper limit ($\tau < 10$ ms) but is well below the lower limit ($\tau > 10$ s) given by Posselt et al. [129] This apparent inconsistency could be related to a more complex $\tau(T)$ dependence at lower Ts, different irradiation conditions, or limitations of estimating τ based on the dose rate effect, as recently discussed. [16] Comparing DA in Ge to that in other semiconductors, it should be noted that τ values of $\sim 0.3 - 8$ ms in Ge are similar to those for Si (τ of $\sim 4 - 13$ ms at room T), 3C-SiC ($\tau = 3$ ms at 100 °C), and 4H-SiC (τ of $\sim 1 - 5$ ms at $25 - 250$ °C) recently measured with the pulsed ion beam technique. [16, 45, 47, 48]

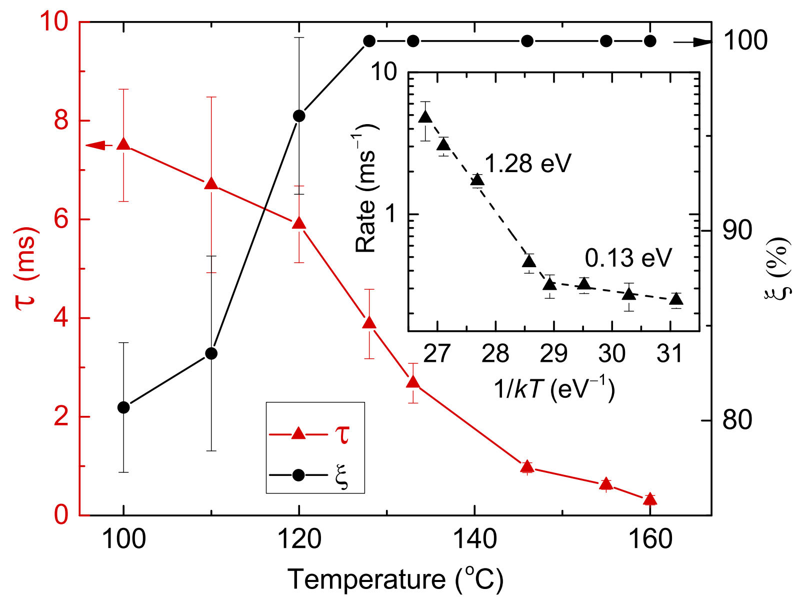

Figure 7.4: (Color online) Temperature dependencies of the effective time constant of DA (τ, left axis) and the DA efficiency (ξ, right axis) for Ge bombarded with 500 keV Ar ions. The inset shows an Arrhenius plot of the dynamic annealing rate. Straight lines are results of linear fitting, revealing activation energies of 1.28 ± 0.07 eV and 0.13 ± 0.03 eV, above and below 130 °C, respectively.

7.3.3 Activation energy

The τ parameter describes the dynamic interaction of mobile point defects produced in different pulses and, hence, in different collision cascades. In other words, τ is a parameter of *inter-cascade* (rather than intra-cascade) defect interaction. To gain insight into such inter-cascade defect dynamics, the $\tau(T)$ dependence is replotted in Arrhenius coordinates as shown in the inset of Fig. 7.4. The second order DA rate is defined as $\frac{1}{\tau(n(0)-n_{\infty})}$, and kT has the usual meaning. Two well defined Arrhenius regions, above and below 130 °C, are clearly revealed in the inset of Fig. 7.4. Linear fitting of the data gives activation energies of 1.28 ± 0.07 eV and 0.13 ± 0.03 eV, above and below 130 °C, respectively. When the $n(t_{off})$ dependencies from Fig. 7.3 are fitted with the first order decay equation (and the DA rate defined as $\frac{1}{\tau_1}$), activation energies of 1.1 and 0.2 eV are measured, above and below 130 °C, respectively.

How are these activation energies related to energy barriers of basic defect migration and interaction processes? It is tempting to associate the activation energies measured here with migration energies of interstitials and vacancies. This is, however, not straightforward. Indeed, previous estimates of point defect migration energies in Ge are limited and, more importantly, vary widely. All the previous experimental estimates of vacancy and interstitial migration energies in Ge have been indirect, with values ranging from 0.2 to 1.3 eV for vacancies [131–133] and 0.16 eV for interstitials. [132] Similarly, theoretical studies predict migration energies of $0.1 - 0.7$ eV for vacancies [134] and $0.3 - 1.4$ eV for interstitials. [134, 135] Hence, the identification of the energetic barriers of different defect migration or interaction processes will need to await further studies as well as a detailed modeling of defect interaction processes.

The transition temperature (T_c) of $\sim$ 130 °C, is consistent with Ts previously

reported ($\sim 114 - 155$ °C) [124–126] above which the disorder depends strongly on the T and dose rate. It also agrees with the T of a post-irradiation defect annealing stage (rather than DA). [136–139] This T_c is much larger than the Ts at which primary defects in Ge become mobile, which appears to occur below ~ 200 K. [137, 138,140,141] These results clearly show that a T_c of 130 °C corresponds to a change in the dominant DA mechanism. What are these two dominant mechanisms? The fact that ξ reaches a saturation of $\sim 100\%$ above T_c could suggest that the defect clusters produced during cascade thermalization and intra-cascade DA are no longer stable, and DA becomes dominated by inter-cascade processes. However, comprehensive theoretical studies, benchmarked against this experimental data, are required to better understand the atomistics of DA in Ge.

7.4 Conclusion

In summary, the pulsed ion beam method was used to study defect interaction dynamics in Ge bombarded with 500 keV Ar ions in the T range of $100 - 160$ °C. Results have revealed that τ decreases monotonically in the range of $\sim 0.3 - 8$ ms with increasing T. An L_d of ~ 38 nm was estimated. There is a major change in the dominant DA process, in which the activation energy changes from ~ 0.1 eV (for T $\lesssim 130$ °C) to ~ 1.3 eV (for T $\gtrsim 130$ °C). These results provide an important step toward the understanding of the mechanisms of radiation damage buildup in Ge.

8. INFLUENCE OF MICROSTRUCTURE ON RADIATION DEFECT DYNAMICS IN SI

Often when an energetic ion enters a crystalline material, a cascade of ballistically generated point defects is created. These defects undergo dynamic annealing (DA) through migration, recombination and clustering. These DA processes are sensitively affected by the microstructure of the material. Indeed, grain boundaries, surfaces, stacking faults, dislocations and, defect clusters are understood to impact a materials ability to efficiently recover from irradiation damage. In some cases a microstructure containing these defect structures can lead to improved damage recovery and increased radiation tolerance. For example, nanocrystalline metals (Pd [142], Au [143], Ni [144], $Cu{-}Al_2O_3$ [144] and, TiNi [145]) have shown an increase in radiation tolerance with grain refinement. In addition, cold working of structural steels, which is known to increase dislocation density, has been used to improve radiation tolerance through increased defect recovery [146, 147]. However, just as often materials show a decrease in radiation tolerance with such microstructural modification. Most inorganic nonmetallics (Si [148], Ge [149] and, SiC [150]) have shown a decrease in radiation tolerance with grain refinement with GaN [151] being one exception. Dislocations are known to preferentially annihilate either vacancies or interstitials, depending on the stress interaction of each species with dislocations, which can lead to an interstitial/vacancy rich microstructure [22, 152].

Despite decades of research into the role of various microstrutures in annealing defects, it is still not clear why some microstructures promote defect recombination while others inhibit such recombination. Molecular dynamics (MD) simualtion has clarfied some of the atomistic processes [153–155]. Bai et al. showed that grain

boundaries exhibit a loading/unloading effect in which interstitial absorption and emission leads to highly efficient defect recovery. [153] However, MD simulation is not capable of capturing the full temporal and spatial scales of dynamic annealing processes, which are known to dominate the defect recovery process. A new set of advanced experimental characterization techniques are required to capture the dynamics involved in defect recovery.

In this article we demonstrate an experimental technique which can measure the time constant of dynamic annealing (τ) as a function of the materials microstructure. Using a recently developed pulsed ion beam method [16,45,47,48,81,156], we measure τ in Si under 500 keV Ar irradiation as a function of microstructural damage (defect clusters and amorphous pockets) and in a microstructure containing a high density of dislocation loops (clamshell defect).

Defect clusters are perhaps the most well known example of a microstructures ability to influence defect recovery. The super linear behavior of damage accumulation observed in many materials is a direct result of the decrease in defect recovery efficiency with increasing disorder. Despite this effect being known for over half a century, it is still not well understood. Our results show the dynamic annealing time constant in Si increases with increasing disorder. Damage accumulation in Si is a balance between the rate of defect accumulation due to irradiation and the rate of dynamic annealing. Thus, the increased lifetime (or decrease in DA rate) with increasing disorder leads to a decrease in defect recovery and a decrease in radiation tolerance. By contrast, the clamshell defect shows a decrease in the dynamic annealing time constant with increasing dislocation density. These results demonstrate a novel method for probing the influence of microstructure on the lifetime of radiation generated defects and will likely have important implications for designing radiation tolerant materials.

8.1 Experimental

Float-zone grown (100) Si single crystals (with a resistivity of $\sim 5\ \Omega$ cm) were bombarded with 500 keV $^{40}Ar^{+}$ ions at 7° off the [100] direction at 100 °C. The 4 MV ion accelerator (National Electrostatics Corporation, model 4UH) at Lawrence Livermore National Laboratory was used for both ion irradiation and ion beam analysis. To improve thermal contact, the samples were attached to the Cu sample holder with conductive Ag paste. All irradiations were performed in a broad beam mode [45] with an instantaneous dose rate $F_{on} \approx 1.9 \times 10^{13}$ cm^{-2} s^{-1}.

The damaged microstructures were created by irradiation with a continuous beam at 100 °C to doses ranging from 1.5×10^{14} to 7×10^{14} cm^{-2}. The primary disorder process under these conditions is the accumulation of simple point defects and their accumulation into more complex structures (e.g. polyvacancy and polyinterstitials). [9, 157] However, above a certain concentration of defects ($\gtrsim$ 14 % [158]) the lattice suffers catastrophic collapse into the amorphous phase. As a result, the damaged microstructures are a combination of defect clusters and amorphous zones. Throughout the remainder of the text this microstructure will be referred to simply as *predamage*.

The clamshell defects were created by first irradiating with a continuous beam to a dose of 1.7×10^{13} cm^{-2} at -196 °C which created a buried amorphous layer. Next, the sample was annealed at 500 or 600 °C for 45 minutes causing recrystallization from both the surface and bulk. Asymmetries in the crystallization fronts resulted in a highly defective region consisting of a dense network of interstitial loop dislocations [22,159]. Throughout the remainder of the text these microstructures will be referred to as *500 °C* and *600 °C clamshell*.

The subsequent pulsed irradiations were done at 100 °C with the dose split into

a train of equal square pulses each with duration $t_{on} = 1$ ms, corresponding to $\sim 4.6 \times 10^{-5}$ displacements per atom (DPA) per pulse. [20] The depth profile of ballistically-generated vacancies was calculated with the TRIM code (version SRIM-2013.00) [20] with an atomic concentration of Si of 4.98×10^{22} atoms cm^{-3} and a threshold energy for atomic displacements of 13 eV. The adjacent pulses were separated by time t_{off}, which was varied between 0.2 and 50 ms. The inset in Fig. 8.1(a) shows a schematic of the time dependence of the instantaneous dose rate and defines pulsing parameters t_{on}, t_{off}, and F_{on}. A more detailed description of the experimental arrangement can be found elsewhere [15, 45, 47].

The dependence of lattice damage on t_{off} was studied *ex-situ* at room temperature by ion channeling. Depth profiles of lattice disorder were measured with 2 MeV $^4He^+$ ions incident along the [100] direction and backscattered into a detector at 164° relative to the incident beam direction. Raw channeling spectra were analyzed with one of the conventional algorithms [18] for extracting depth profiles of relative disorder. Values of averaged bulk relative disorder (n) were obtained by averaging depth profiles of relative disorder over 10 channels (~ 30 nm) centered on the bulk damage peak maximum. Error bars of n are standard deviations. Ion doses at different predamage levels were chosen such that, for continuous beam irradiation, n was in the range of $0.6 - 0.9$ (with $n = 1$ corresponding to full amorphization).

8.2 Results and discussion

Figure 8.1 shows representative depth profiles of relative disorder for bombardment with continuous ($t_{off} = 0$ ms) and pulsed ($t_{off} = 1$, 3 ms) ion beams in (a) pristine Si, (b) Si predamaged by irradiating with Ar to a dose of 4.5×10^{14} cm^{-2} and (c) 500 °C clamshell. Also shown by solid circles is the defect state prior to pulsed irradiation. The predamaged samples were bimodal with the first small peak at the

sample surface and the second major peak in the crystal bulk at $\sim$ 500 nm whereas the clamshell defect showed a skewed-bimodal distribution with a small surface peak and a bulk damage peak at $\sim$ 450 nm. The bulk damage peak is skewed towards the clamshell defect which is located at $\sim$ 410 nm.

Figure 8.1 further shows that the average relative bulk disorder (n) decreases with increasing t_{off} for both microstructures. This finding is consistent across all microstructures studied and is better illustrated in Fig. 8.2, which summarizes $n(t_{off})$ dependencies for all three microstructures; 500 °C clamshell, 4.5×10^{14} cm^{-2} predamage, and pristine. It is seen from Fig. 8.2 that, for all the cases, n monotonically decreases with increasing t_{off}. Solid and dashed lines are fits of $n(t_{off})$ dependencies via the Marquardt-Levenberg algorithm with a first ($n(t_{off}) = n_\infty + (n(0) - n_\infty)\exp(-t_{off}/\tau_1)$) and second ($n(t_{off}) = n_\infty + \frac{n(0)-n_\infty}{1+\frac{t_{off}}{\tau}}$) order decay equation, respectively. Here, τ is the characteristic decay time constant, and n_∞ is relative disorder for $t_{off} >> \tau$. The τ value for the 500 °C clamshell, predamage, and pristine Si was 0.95 (0.47), 3.4 (2.4), and 1.4 (0.7) ms for first (second) order fitting, respectively.

The observed differences in τ between various microstructures is well beyond the experimental error and thus can be explained as a change in the physical process of DA in Si. However, our pulsed beam technique measures a τ value which is averaged across a range of microstructures starting from the predamaged or clamshell defect microstructure and accumulating damage (*during pulsed irradiation*) to the final $n(t_{off})$ disorder level. Despite this, previous studies indicated that τ was independent of the total dose for Si irradiated at RT by 500 keV Ar. [16]

To determine the dependence of τ on the total dose, several sets of pulsed irradiation were performed on pristine Si between which the total dose was varied. Figure 8.3 (bottom axis) shows τ as a function of the bulk relative disorder with

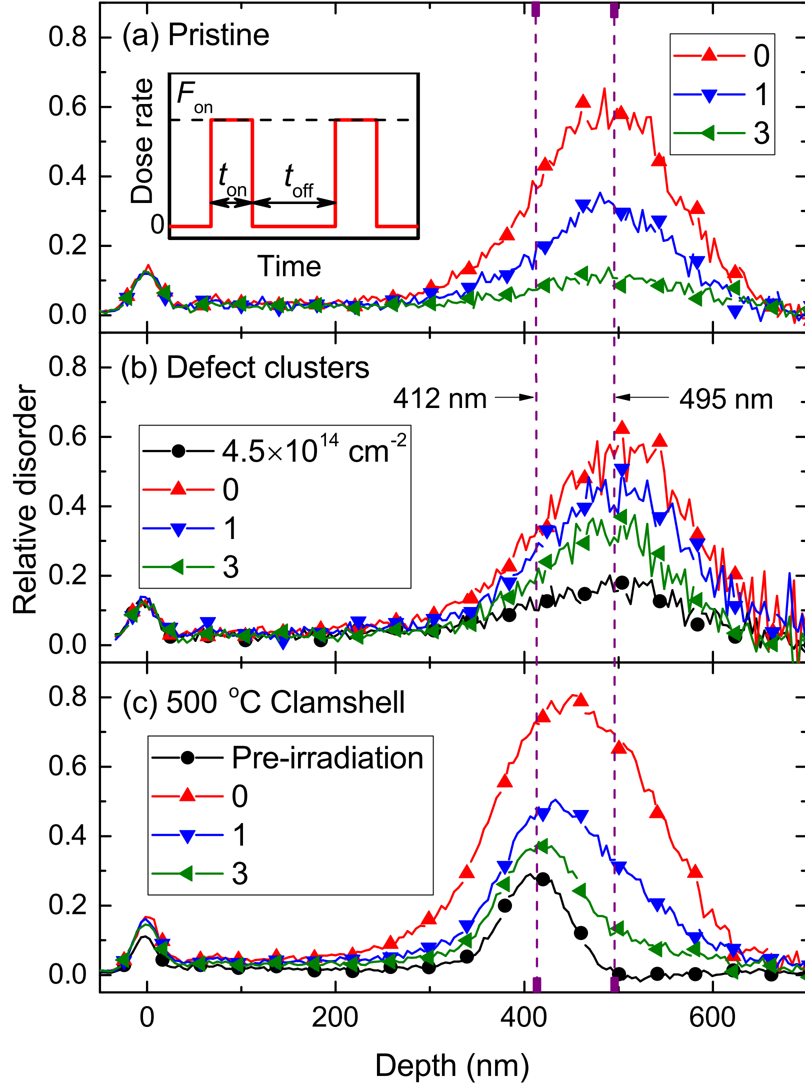

Figure 8.1: (Color online) Selected depth profiles of relative disorder in Si for 500 keV Ar irradiation of (a) pristine, (b) predamaged with defect clusters to a dose of 4.5×10^{14} cm^{-2}, and (c) the 500 °C clamshell defect with a continuous ($t_{off} = 0$) and pulsed ($t_{off} = 1, 3$ ms). The defect state prior to pulsed irradiation is shown by solid circles in (b) and (c). For clarity, only every 10th experimental point is depicted. The inset in (a) is a schematic of the time dependence of the instantaneous dose rate for pulsed beam irradiation, defining t_{on}, t_{off}, and F_{on}.

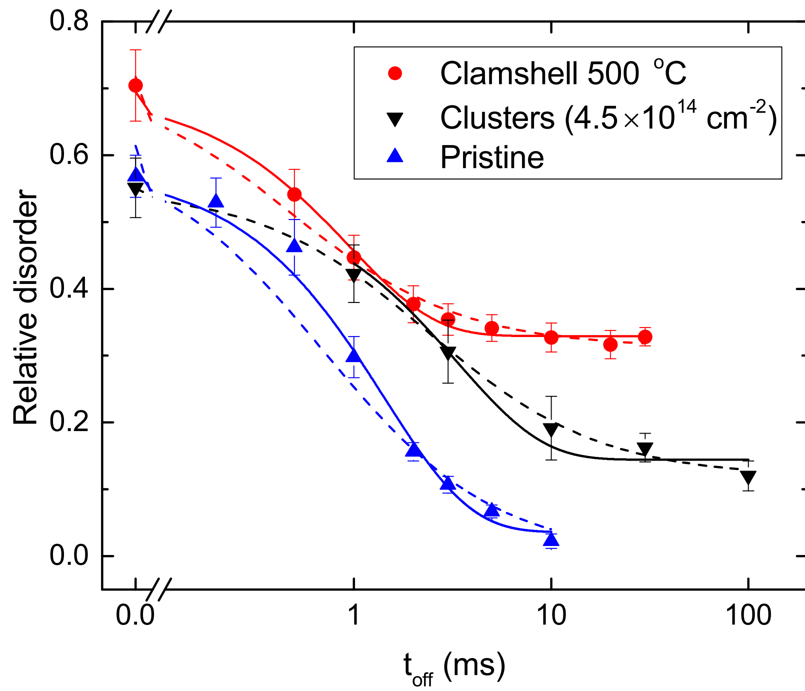

Figure 8.2: (Color online) Relative bulk disorder in Si bombarded with a pulsed beam of 500 keV Ar ions with $F_{on} = 1.9 \times 10^{13}$ cm^{-2} s^{-1} and $t_{on} = 1$ ms as a function of the passive portion of the beam duty cycle (t_{off}) for the 500 °C clamshell defect, a sample preimplanted with 500 keV Ar to a dose of 4.5×10^{14} cm^{-2}, and a pristine sample. Fitting curves with the first (second) order decay equation are shown by solid (dashed) lines.

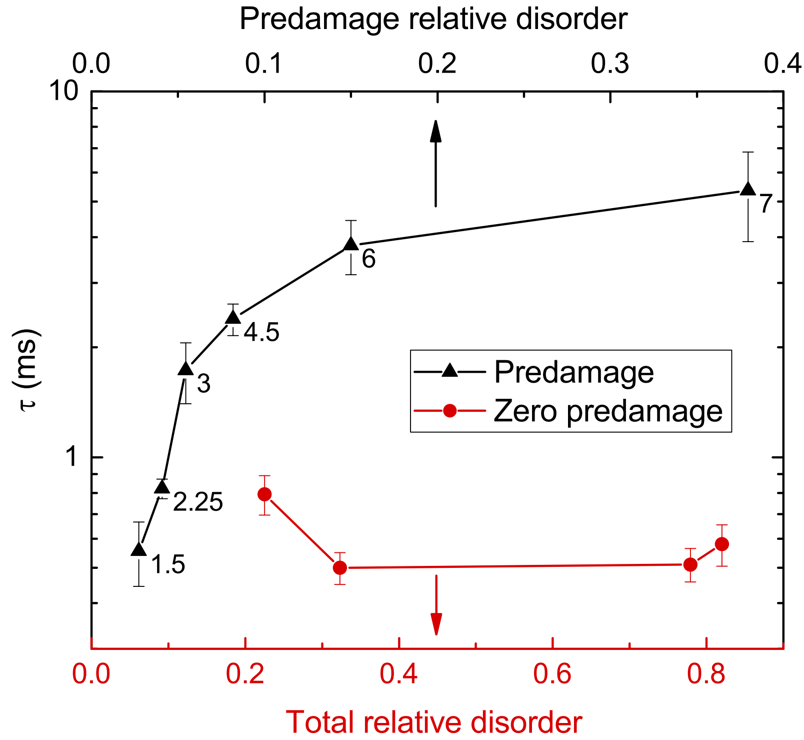

Figure 8.3: (Color online) Dependence of τ on the total relative disorder with zero pre-damage (bottom axis) and as a function of pre-damage relative disorder (top axis).

irradiation doses shown next to data points in units of 10^{14} cm^{-2}. The resulting change in τ with increasing total bulk disorder (total irradiation dose) is negligible, which is in agreement with previous work at RT in Si. [16] These results suggest that τ is dominated by defect processes that occur at relatively low disorder levels (i.e. the initial damage nucleation has a larger influence on the defect dynamics compared to the final disorder level).

The effect of predamage on the defect lifetime was studied by irradiating Si with a continuous beam and then performing the beam pulsing on top of the already damaged microstructure. Figure 8.3 (top axis) shows τ as a function of predamage with irradiation doses shown next to data points in units of 10^{14} cm^{-2}. The defect

lifetime (dynamic annealing rate) is shown to monotonically increase (decrease) with increasing predamage. This behavior could be due to migrating defects trapping in shallow energy wells of defect clusters and then subsequently de-trapping. Alternatively, the increase could be the result of a complex interaction between ion beam induced amorphization and recrystallization at the amorphous-crystalline interface of amorphous pockets. Linnros et al. showed a significantly longer defect relaxation time for ion beam induced epitaxial recrystallization ($\sim$ 300 ms) compared to the defect relaxation time found for amorphization in Si ($\sim$ 6 ms). [43] Further investigation is required to understand the complex interaction of mobile defects within a damaged microstructure.

Figure 8.4 shows the dynamic annealing efficiency, defined as $\xi = (n(0) - n_{\infty})/(n(0) - n_{pre})$ where n_{pre} is the predamage, as a function of total relative disorder (zero predamage, bottom axis) and as a function of predamage (top axis). The change in ξ with changing total relative disorder (total dose) is negligible. Taking the partial derivative of ξ with respect to Φ, the total dose, shows that ξ increases with increasing total dose given $\partial n(0)/\partial\Phi > \partial n_{\infty}/\partial\Phi$. A number of dose rate studies on Si have shown this condition to be satisfied. See, for example, Ref. [9] and references therein. In contrast, ξ shows a clear decrease with increasing predamage from $\sim$ 105% to 40%. For small predamage ($\lesssim$ 6%), ξ is greater than 100% due to ion beam induce crystallization effects (IBIC) in which, for $t_{off} >> \tau$, the predamage anneals. As the predamage increases above $\sim$6% damage accumulation begins to out weigh the effects of IBIC leading to a decrease in ξ. This decrease in ξ with increasing lattice disorder, points to a decrease in the total fraction of defects which participate in DA effects or an increase in the fraction of defects which form stable damage. The defect clusters and amorphous zones created in the predamage irradiations provide nucleation sites for the formation of stable damage.

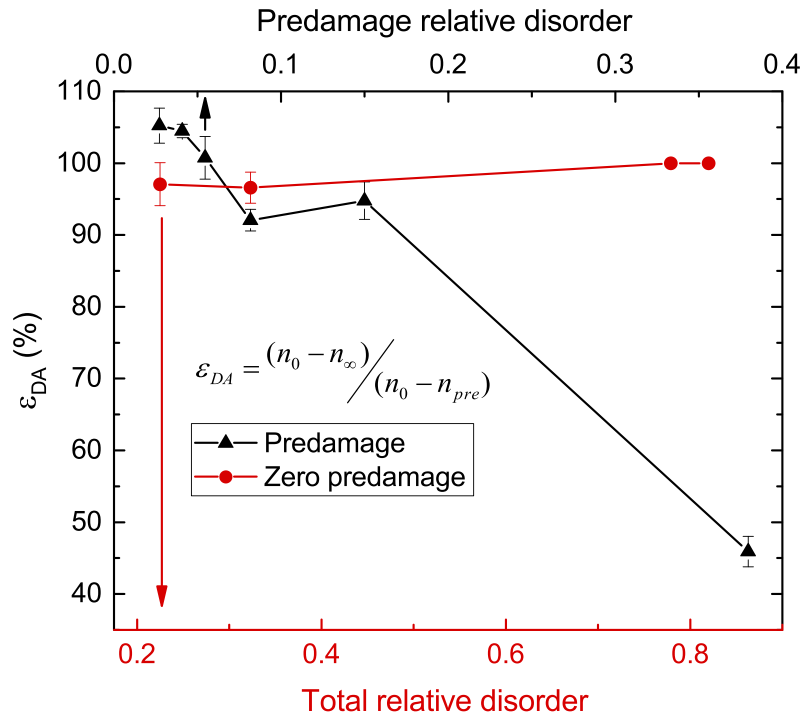

Figure 8.4: (Color online) Plot of the dynamic annealing efficiency as a function of the total relative disorder with zero pre-damage (bottom axis) and as a function of the pre-damage relative disorder (top axis).

Although τ was shown to increase in a microstructure containing defect clusters and amorphous zones, this is not the case for every type of defect. The microstructure containing a high density of dislocations in the form of a clamshell defect provides one such example. Figure 8.2 showed that τ decreased in the clamshell microstructure compared to either a pristine or predamaged microstructure. To better understand the role of the clamshell defect, we have plotted τ for pristine Si and the 500 and 600 °C clamshell microstructures as a function of depth. The τ for pristine Si was approximately constant with depth until $\sim$ 320 nm at which point the error bars grew to large due to the decreasing DA range. Interestingly, the τ for the pristine and the 500 °C clamshell defect are identical beyond a depth of 480 nm. Thus, beyond this depth the influence of the clamshell defect is negligible. However, as you approach the clamshell defect, the τ begins to decrease rapidly, reaching a maximum near the peak of the clamshell defect. The decrease in τ or increase in the DA rate is likely the result of mobile defects interacting with the clamshell defect by annihilating or trapping in the structure. The 600 °C showed a defect peak prior to pulsed irradiation which almost undetectable by RBS-C. Increasing the anneal temperature by 100 °C likely caused dislocations to combine forming a lower density of long range dislocations. Despite the much lower concentration of dislocations, the 600 °C clamshell showed qualitatively similar behavior to the 500 °C clamshell. Goldberg et al. showed that a clamshell defect was capable of preferentially nucleating damage and lowering the damage level of the surrounding lattice. The shift in the bulk damage peak suggest a similar defect nucleation around the clamshell defect. However, the total irradiation dose to reach amorphization was similar in the pristine and clamshell defect microstructures suggesting that the total irradiation induced disorder is conserved.

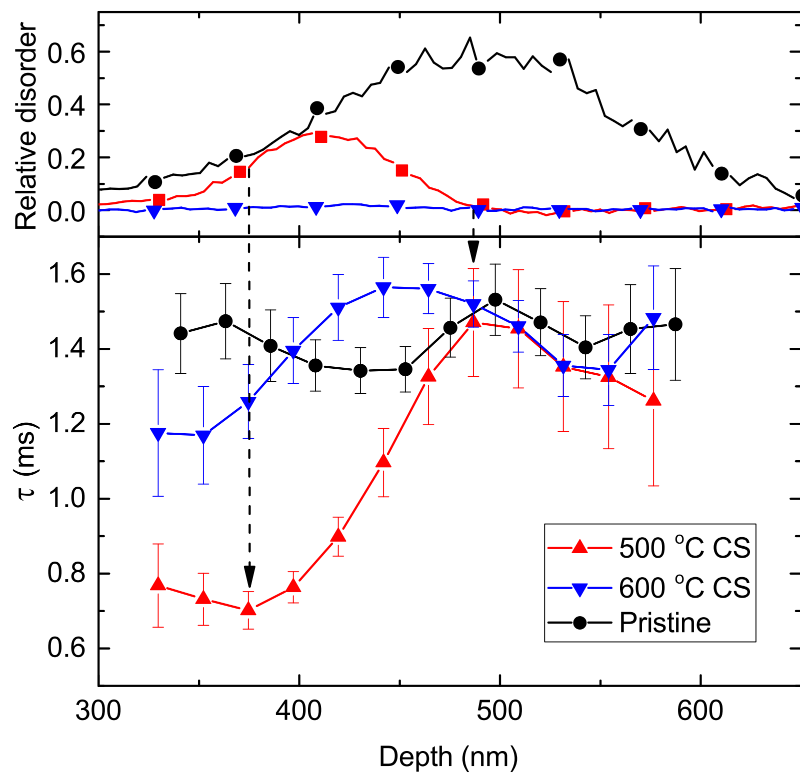

Figure 8.5: (Color online) Selected RBS channeling depth profiles of relative disorder of the pristine Si 0 ms irradiation and the 500 and 600 °C clamshell defects prior to pulsed irradiation by 500 keV Ar (top pane) and τ as a function of depth for the pristine and 500 and 600 °C clamshell defect.

8.3 Conclusion

In summary, we have demonstrated a novel method to characterize the dynamic interaction of mobile defects created *during irradiation* with the materials microstructure. Using a novel pulsed ion beam technique, we studied the dynamic annealing lifetime for microstructures containing predamage (defect clusters and amorphous zones) and containing a high density of dislocations (clamshell defect). The dynamic annealing time constant for Si at 100 °C under 500 keV Ar irradiation was found to increase with increasing predamage. In contrast, the clamshell defect caused a significant decrease in the dynamic annealing lifetime. The increase of defect lifetime in the predamaged microstructure could be attributed to defects trapping in shallow energy wells of defect clusters and amorphous pockets and then subsequently detrapping. Similarly, the decreased lifetime of defects in the clamshell microstructure could be due to defects permanently trapping at dislocation. These results demonstrate a novel method which can measure the influence of a materials microstructure on the lifetime of mobile radiation defects. Such a technique provides a critical new pathway for studying and designing radiation tolerant materials.

9. SUMMARY

In this dissertation, a novel pulsed ion beam method is developed to measure the defect lifetime, diffusion length, and dominant processes of dynamic annealing in ion irradiated solids. With this pulsed beam method, a defect lifetime of $\sim 0.1 - 100$ ms and a characteristic diffusion length of $\sim 5 - 50$ nm is measured in Si for 500 keV Ne, Ar, Kr, and Xe ion bombardment. Both the lifetime and diffusion length increase with increasing ion mass in Si at room temperature. For all ions, the defect lifetime is observed to decrease with increasing temperature. For Ne, Ar, and Kr ion irradiation, two well-defined activation energies of ~ 0.1 and ~ 0.4 eV are measured above and below the critical temperature, respectively. Rate theory modeling, benchmarked against this data, suggests a crucial role of both vacancy and interstitial diffusion, with the dynamic annealing rate limited by the migration and interaction of vacancies. For Xe irradiations, the activation energies were ~ 0.8 and ~ 0.1 eV above and below the critical temperature, respectively. The critical temperature increases with increasing ion mass from room temperature for Ne to ~ 160 °C for Xe.

A fractal model of collision cascades is developed to describe the dependence of dynamic annealing on ion mass. With increasing ion or target mass, the cross section for elastic collision increases, hence, leading to higher density collision cascades. For all ion masses, the cascade density scales according to the fractal geometry with a well-defined fractal dimension. Pulsed beam data, fit to a model assuming a linear relation between defect density and stable disorder, revealed a diffusion length of $\sim 20 - 40$ nm.

The critical temperature of dynamic annealing in Si is shown to increase linearly

with increasing cascade density, not only within a single cascade, but within the *super-cascade* network created within every pulse. In addition, the change in the high temperature activation energy of dynamic annealing from Kr to Xe ion irradiation is the result of increasing cascade density. Analyzing the depth dependence of cascade density in Kr and Xe, reveals a Xe activation energy of 0.8 eV in the bulk, where the cascade density is highest, and 0.4 eV near the surface where the cascade density is comparable to the maximum cascade density in Kr irradiations. In contrast, the activation energy in Kr is $\sim$ 0.4 eV, independent of depth.

The pulsed beam method is also demonstrated to work in Ge and SiC. In Ge, the defect lifetime rapidly decreases from $\sim$ 8 to 0.3 ms with increasing temperature and the diffusion length was $\sim$ 38 nm. The Arrhenius behavior of the dynamic annealing rate is qualitatively similar to that observed in Si, but quantitatively different. The two dominant dynamic annealing processes reveal activation energies of 1.28 eV and 0.13 eV, above and below the critical temperature of 130 °C, respectively.

Although SiC shows a similar defect lifetime in the range from 1 to 5 ms under 500 keV Ar ion irradiation, the behavior is very different from either Si or Ge. Despite the defect recombination efficiency showing an expected monotonic increase with increasing temperature, the defect lifetime has a non-monotonic temperature dependence with a maximum at $\sim$ 100 °C. This finding indicates a change in the dominant defect interaction mechanism at $\sim$ 100 °C.

Radiation defect processes also depend strongly on the state of the surrounding crystalline lattice. The pulsed beam method is used in Section 8 to measure the dynamics of radiation generated defects in the following: (1) defect clusters and amorphous zones and (2) clamshell defects containing a high density of dislocations. Results show that the defect lifetime depends strongly on the microstructure. In a damaged microstructure containing amorphous zones and defect clusters, the lifetime

of mobile defects increases with increasing damage. In contrast, in a microstructure containing a high density of dislocations, the defect lifetime decreases.

Understanding radiation defect dynamics is one of the grand challenges in the radiation damage community. Although many aspects still remain unknown, the results shown in this dissertation represent a major advancement. The author hopes that future systematic studies will build upon the novel pulsed ion beam method developed in this dissertation, ultimately leading to the development of radiation tolerant materials.

REFERENCES

[1] G. W. Kinchin and R. S. Pease, Rep. Prog. Phys. **18**, 1 (1955).

[2] J. W. Corbett, J. P. Karins, and T. Y. Tan, Nucl. Instrum. Meth. **182/183**, 457 (1981).

[3] S. T. Picraux and F. L. Vook, Radiat. Eff. **11**, 179 (1971).

[4] N. A. G. Ahmed, C. E. Christodoulides, G. Carter, M. J. Nobes, and A. I. Titov, Nucl. Instrum. Meth. **168**, 283 (1980).

[5] O. W. Holland and C. W. White, Nucl. Instrum. Meth. Phys. Res. Sect. B **59-60**, 353 (1991).

[6] P. J. Schultz, C. Jagadish, M. C. Ridgway, and R. G. Elliman, Phys. Rev. B **44**, 9118 (1991).

[7] B. G. Svensson, C. Jagadish, and J. S. Williams, Phys. Rev. Lett. **71**, 1860 (1993).

[8] R. D. Goldberg, J. S. Williams, and R. G. Elliman, Nucl. Instrum. Meth. Phys. Res. Sect. B **106**, 242 (1995).

[9] A. I. Titov and G. Carter, Nucl. Instrum. Meth. Phys. Res. Sect. B **119**, 491 (1996).

[10] A. I. Titov, A. Yu. Azarov, L. M. Nikulina, and S. O. Kucheyev, Phys. Rev. B **73**, 064111 (2006).

[11] G. Carter, J. Appl. Phys. **79**, 8285 (1996).

[12] M. T. Myers, S. Charnvanichborikarn, L. Shao, and S. O. Kucheyev, Phys. Rev. Lett. **109**, 095502 (2012).

[13] S. Charnvanichborikarn, M. T. Myers, L. Shao, and S. O. Kucheyev, J. Phys.: Condens. Matter **25**, 162203 (2013).

[14] J. B. Wallace, L. B. Bayu Aji, L. Shao, and S.O. Kucheyev, Appl. Phys. Lett. **106**, 202102 (2015).

[15] S. Charnvanichborikarn, M. T. Myers, L. Shao, and S. O. Kucheyev, J. Phys. Condens. Matter **25**, 162203 (2013).

[16] J. B. Wallace, S. Charnvanichborikarn, L. B. Bayu Aji, M. T. Myers, L. Shao, and S. O. Kucheyev, J. Appl. Phys. **118**, 135709 (2015).

[17] L. B. Bayu Aji, J. B. Wallace, L. Shao, and S. O. Kucheyev, J. Phys. D. Appl. Phys. **49**, 19LT01 (2016).

[18] K. Schmid, Radiat. Eff. **17**, 201 (1973).

[19] J. W. Bittner and R. D. Moffat, Phys. Rev. **96**, 374 (1954).

[20] J. F. Ziegler, M. D. Ziegler, and J. P. Biersack, Nucl. Instr. and Meth. B **268**, 1818 (2010).

[21] D. J. Mazey, R. S. Nelson, and R. S. Barnes, Philos. Mag. **17**, 1145 (1968).

[22] R. Goldberg, J. Williams, and R. Elliman, Phys. Rev. Lett. **82**, 771 (1999).

[23] E. Oliviero, S. Peripolli, L. Amaral, P. F. P. Fichtner, M. F. Beaufort, J. F. Barbot, and S. E. Donnelly, J. Appl. Phys. **100**, 043505 (2006).

[24] I. Jencic, M. W. Bench, I. M. Robertson, and M. A. Kirk, J. Appl. Phys. **78**, 974 (1995).

[25] See, for example, a review by D. A. Thompson, Radiat. Effects **56**, 105 (1981).

[26] A. Kinomura, J. S. Williams, and K. Fujii, Phys. Rev. B **59**, 15214 (1999).

[27] A. I. Titov, S. O. Kucheyev, V. S. Belyakov, and A. Y. Azarov, J. Appl. Phys. 90, 3867 (2001).

[28] S. O. Kucheyev, J. S. Williams, A. I. Titov, G. Li, and C. Jagadish, Appl. Phys. Lett. **78**, 2694 (2001).

[29] S. Charnvanichborikarn, M. T. Myers, L. Shao, and S. O. Kucheyev, Scr. Mater. **67**, 205 (2012).

[30] M. T. Myers, S. Charnvanichborikarn, L. Shao, and S. O. Kucheyev, Scr. Mater. **67**, 65 (2012).

[31] G. Lulli, P. G. Merli, and M. V. Antisari, Phys. Rev. B **36**, 8038 (1987).

[32] M. O. Ruault, J. Chaumont, and H. Bernas, Nucl. Instrum. Methods **209/210**, 351 (1983).

[33] T. Matsukawa, K. Yokoyama, S. Sawara, and I. Ohdomari, Appl. Phys. Lett. **74**, 2663 (1999).

[34] A. I. Titov, V. S. Belyakov, and A. Yu. Azarov, Nucl. Instrum. Methods Phys. Res. B **212**, 169 (2003).

[35] P. N. K. Deenapanray, Appl. Phys. Lett. **80**, 1577 (2002).

[36] J. L. Benton, J. Vac. Sci. Technol. B Microelectron. Nanom. Struct. **10**, 540 (1992).

[37] K. K. Larsen, V. Privitera, S. Coffa, F. Priolo, S. U. Campisano, and A. Carnera, Phys. Rev. Lett. **76**, 1493 (1996).

[38] V. Privitera, S. Coffa, F. Priolo, K. Kyllesbech Larsen, and G. Mannino, Appl. Phys. Lett. **68**, 3422 (1996).

[39] J. F. Gibbons, Proc. IEEE **60**, 1062 (1972).

[40] G. S. Was, J. Nucl. Mater. **30**, 1158 (2015).

[41] J. G. Gigax, E. Aydogan, T. Chen, D. Chen, L. Shao, Y. Wu, W. Y. Lo, Y. Yang, and F. A. Garner, J. Nucl. Mater. **465**, 343 (2015).

[42] E. Chason, S. T. Picraux, J. M. Poate, J. O. Borland, M. I. Current, T. D. de la Rubia, D. J. Eaglesham, O. W. Holland, M. E. Law, C. W. Magee, J. W. Mayer, J. Melngailis, and A. F. Tasch, J. Appl. Phys. **81**, 6513 (1997).

[43] J. Linnros and G. Holmén, J. Appl. Phys. **62**, 4737 (1987).

[44] J. Linnros, B. Svennson, and G. Holmen, Phys. Rev. B **30**, 3629 (1984).

[45] M. T. Myers, S. Charnvanichborikarn, L. Shao, and S. O. Kucheyev, Phys. Rev. Lett. **109**, 095502 (2012).

[46] J. B. Wallace, L. B. Bayu Aji, L. Shao, and S. O. Kucheyev, J. Appl. Phys. **118**, 135709 (2015).

[47] J. B. Wallace, L. B. Bayu Aji, L. Shao, and S. O. Kucheyev, Appl. Phys. Lett. **106**, 202102 (2015).

[48] L. B. Bayu Aji, J. B. Wallace, L. Shao, and S. O. Kucheyev, Sci. Rep. **6**, 30931 (2016).

[49] G. D. Watkins, Mater. Sci. Semicond. Process. **3**, 227 (2000).

[50] P. G. Coleman and C. P. Burrows, Phys. Rev. Lett. **98**, 265502 (2007).

[51] Y. Shimizu, M. Uematsu, and K. M. Itoh, Phys. Rev. Lett. **98**, 7 (2007).

[52] L. Shao, J. Liu, Q. Y. Chen, and W.-K. Chu, Mater. Sci. Eng. R Reports **42**, 65 (2003).

[53] A. Hallén, N. Keskitalo, L. Josyula, and B. G. Svensson, J. Appl. Phys. **86**, 214 (1999).

[54] K. Levenberg, Q. Appl. Math **2**, 164 (1944).

[55] D. Maroudas and R. A. Brown, Phys. Rev. B **47**, 15562 (1993).

[56] G. H. Gilmer, T. Diaz de la Rubia, D. M. Stock, and M. Jaraiz, Nucl. Instr. Meth. B **102**, 247 (1995).

[57] F. El-Mellouhi, N. Mousseau, and P. Ordejón, Phys. Rev. B **70**, 205202 (2004).

[58] M. Posselt, F. Gao, and H. Bracht, Phys. Rev. B **78**, 035208 (2008).

[59] P. Śpiewak and K. J. Kurzydłowski, Phys. Rev. B **88**, 195204 (2013).

[60] W. H. McCrea and F. J. W. Whipple, P. Roy. Soc. Edinb. **60**, 281 (1940).

[61] G. S. Oehrlein, I. Krafcsik, J. L. Lindstrom, A. E. Jaworowski, and J. W. Corbett, J. Appl. Phys. **54**, 179 (1983).

[62] B. G. Svensson, C. Jagadish, and J. S. Williams, Phys. Rev. Lett. **71**, 1860 (1993).

[63] B. G. Svensson, C. Jagadish, A. Hallén, and J. Lalita, Phys. Rev. B **55**, 10498 (1997).

[64] A. I. Titov and S. O. Kucheyev, Nucl. Instr. and Meth. B **168** 375 (2000).

[65] D. A. Thompson, R. S. Walker, and J. A. Davies, Radiat. Eff. **32**, 135 (1977).

[66] Y. T. Cheng, M. A. Nicolet, and W. L. Johnson, Phys. Rev. Lett. **58**, 2083 (1987).

[67] K. B. Winterbon, H. M. Urbassek, P. Sigmund, and A. Gras-Marti, Phys. Scripta **36**, 689 (1987).

[68] B. B. Mandelbrot and R. Pignoni. *The fractal geometry of nature* (W.H. FReeman, New York, 1983).

[69] F. Rossi, D. M. Parkin, and M. Nastasi, J. Mat. Res. **4.01**, 137 (1989).

[70] L. B. Bayu Aji, J. B. Wallace, L. Shao, and S.O. Kucheyev, J. Phys. D. Appl. Phys. **49**, 19LT01 (2016).

[71] L. L. Snead, T. Nozawa, Y. Katoh, T. S. Byun, S. Kondo, and D. A. Petti, J. Nucl. Mater. **371**, 329 (2007).

[72] A. Fissel, Phys. Rep. **379**, 149 (2003).

[73] R. Devanathan, W. J. Weber, and F. Gao, J. Appl. Phys. **90**, 2303 (2001).

[74] H. L. Heinisch, and B. N. Singh, Phil. Mag. A **67**, 407 (1993).

[75] L. B. Bayu Aji, J. B. Wallace, L. Shao, and S. O. Kucheyev, J. Phys. D Appl. Phys. **49**, 19LT01 (2016).

[76] J. B. Wallace, L. B. Bayu Aji, T. T. Li, L. Shao, and S. O. Kucheyev, J. Appl. Phys. **118**, (2015).

[77] A. I. Titov, A. Y. Azarov, L. M. Nikulina, and S. O. Kucheyev, Nucl. Instrum. Meth. Phys. B **256**, 207 (2007).

[78] A. I. Titov, P. A. Karaseov, A. Y. Azarov, and S. O. Kucheyev, Nucl. Instrum. Meth. Phys. B **267**, 2701 (2009).

[79] A. Y. Azarov, A. I. Titov, P. A. Karaseov, and A. Hallén, Nucl. Instrum. Meth. Phys. B **267**, 1247 (2009).

[80] J. B. Wallace, L. B. Bayu Aji, L. Shao, and S. O. Kucheyev, Nucl. Instr. Meth. B, article in press, 2017.

[81] J. B. Wallace, L. B. Bayu Aji, A. A. Martin, S. J. Shin, L. Shao, and S. O. Kucheyev, Sci. Rep. **7**, 39754 (2017).

[82] L. B. Bayu Aji, J. B. Wallace, L. Shao, and S.O. Kucheyev, Unreleased LLNL manuscript, LLNL-JRNL-730937-DRAFT.

[83] J. B. Wallace, L. B. Bayu Aji, L. Shao, and S.O. Kucheyev, Unreleased LLNL manuscript.

[84] A. Lohrmann, N. Iwamoto, Z. Bodrog, S. Castelletto, T. Ohshima, T. J. Karle, A. Gali, S. Prawer, J. C. McCallum, and B. C. Johnson Nat. Commun. **6**, 7783 (2015).

[85] Y. Zhang, R. Sachan, O. H. Pakarinen, M. F. Chisholm, P. Liu, H. Xue, and W. J. Weber Nat. Commun. **6**, 8049 (2015).

[86] H. Inui, H. Mori, H. Fujita, Philos. Mag. B **61**, 107 (1990).

[87] A. Matsunaga, C. Kinoshita, K. Nakai, and Y. Tomokiyo, J. Nucl. Mater. **179-181**, 457 (1991).

[88] H. Inui, H. Mori, A. Suzuki, and H. Fujita, Philos. Mag. B **65**, 1 (1992).

[89] S. J. Zinkle and L. L. Snead, Nucl. Instr. and Meth. B **116**, 92 (1996).

[90] W. J. Weber, L. M. Wang, N. Yu, N. J. Hess, Mater. Sci. Eng. A **253**, 62 (1998).

[91] A. Y. Kuznetsov, J. Wong-Leung, A. HalleÌĄn, C. Jagadish, and B. G. Svensson, J. Appl. Phys. **94**, 7112 (2003).

[92] Y. Zhang, W. J. Weber, W. Jiang, C. M. Wang, V. Shutthanandan, and A. Hallen, J. Appl. Phys. **93**, 1954 (2003).

[93] J. Slotte, K. Saarinen, M. S. Janson, A. HalleÌĄn, A. Y. Kuznetsov, B. G. Svensson, J. Wong-Leung, and C. Jagadish, J. Appl. Phys. **97**, 033513 (2005).

[94] E. Wendler, T. Bierschenk, W. Wesch, E. Friedland, and J. B. Malherbe, Nucl. Instr. and Meth. B **268**, 2996 (2010).

[95] J. B. Wallace, L. B. Bayu Aji, L. Shao, and S. O. Kucheyev, Appl. Phys. Lett. **106**, 202102 (2015).

[96] J. B. Wallace, L. B. Bayu Aji, T. T. Li, L. Shao, and S. O. Kucheyev, J. Appl. Phys. **118**, 105705 (2015).

[97] N. Swaminathan, D. Morgan, and I. Szlufarska, J. Nucl. Mater. **414**, 431 (2011).

[98] W. J. Weber and L. M. Wang, Nucl. Instr. and Meth. B **106**, 298 (1995).

[99] W. J. Weber, Nucl. Instr. and Meth. B **166-167**, 98 (2000).

[100] Y. Zhang, W. J. Weber, W. Jiang, C. M. Wang, V. Shutthanandan, and A. Hallen, J. Appl. Phys. **93**, 1954 (2003).

[101] C. Jiang, M. J. Zheng, D. Morgan, and I. Szlufarska, Phys. Rev. Lett. **111**, 155501 (2013).

[102] W. Jiang, W. J. Weber, S. Thevuthasan, and V. Shutthanandan, J. Nucl. Mater. **289**, 96 (2001).

[103] W. J. Weber, W. Jiang, and S. Thevuthasan, Nucl. Instr. and Meth. B **175-177**, 26 (2001).

[104] Y. Zhang, W. J. Weber, W. Jiang, A. HalleÌĄn, and G. Possnert, J. Appl. Phys. **91**, 6388 (2002).

[105] Z. Rong, F. Gao, W. J. Weber, and G. Hobler, J. Appl. Phys. **102**, 103508 (2007).

[106] M. Posselt, L. Bischoff, J. Teichert, and A. Ster, J. Appl. Phys. **93**, 1004 (2003).

[107] W. Jiang, Y. Zhang, and W. J. Weber, Phys. Rev. B **70**, 165208 (2004).

[108] A. A. Rempel, H. -E. Schaefer, Appl. Phys. A **61**, 51 (1995).

[109] R.C. Barklie, M. Collins, B. Holm, Y. Pacaud, and W. Skorupa, J. Electron. Mater. **26**, 137 (1997).

[110] S. Dannefaer, and D. Kerr, Diam. Relat. Mater. **13**, 157 (2004).

[111] H. Itoh, N. Hayakawa, I. Nashiyama, and E. Sakuma, J. Appl. Phys. **66**, 4529 (1989).

[112] H. Itoh, M. Yoshikawa, I. Nashiyama, H. Okumura, S. Misawa, and S. Yoshida, J. Appl. Phys. **77**, 837 (1995).

[113] A. Hallen, M. S Janson, A. Yu Kuznetsov, D. Aberg, M. K Linnarsson, B. G Svensson, P. O Persson, F. H. C Carlsson, L. Storasta, J. P Bergman, S. G Sridhara, Y. Zhang, Nucl. Instr. and Meth. B **186**, 186 (2002).

[114] L. Jamison, K. Sridharan, S. Shannon, and I. Szlufarska, J. Mater. Res. **29**, 2871 (2014).

[115] W. J. Weber, W. Jiang, S. Thevuthasan, Nucl. Instr. and Meth. B **166**, 410 (2000).

[116] F. F. Morehead, and B. L. Crowder, Radiat. Eff. **6**, 27 (1970).

[117] R. Pillarisetty, Nature **479**, 324 (2011).

[118] S. O. Kucheyev, J. E. Bradby, S. Ruffell, C. P. Li, T. E. Felter, and A. V. Hamza, Appl. Phys. Lett. **90**, 221901 (2007).

[119] J. L. Gomez-Selles, A. Claverie, B. Sklenard, F. Benistant, and I. Martin-Bragado, J. Appl. Phys. **117**, 055703 (2015).

[120] S. Decoster, S. Cottenier, B. De Vries, H. Emmerich, U. Wahl, J.G. Correia, and A. Vantomme, Phys. Rev. Lett. **102**, 065502 (2009).

[121] S. Decoster, and A. Vantomme, J. Phys. D. Appl. Phys. **42**, 165404 (2009).

[122] S. Koffel, P. Scheiblin, A. Claverie, and G. Benassayag, J. Appl. Phys. **105**, 013528 (2009).

[123] G. Impellizzeri, S. Mirabella, and M. G. Grimaldi, Appl. Phys. A **103**, 323 (2010).

[124] G. Holmén and P. Högberg, Radiat. Eff. **12**, 77 (1972).

[125] T. E. Haynes and O. W. Holland, Appl. Phys. Lett. **59**, 452 (1991).

[126] O. W. Holland and T. E. Haynes, Appl. Phys. Lett. **61**, 3148 (1992).

[127] V. S. Belyakov and A. I. Titov, Radiat. Eff. Defects Solids **138**, 231 (1996).

[128] R. C. Birtcher, Philos. Mag. B **73**, 677 (1996).

[129] M. Posselt, L. Bischoff, D. Grambole, and F. Herrmann, Appl. Phys. Lett. **89**, 151918 (2006).

[130] K. Nordlund, M. Ghaly, R. Averback, M. Caturla, T. Diaz de la Rubia, and J. Tarus, Phys. Rev. B **57**, 7556 (1998).

[131] R. E. Whan, Phys. Rev. **140**, A690 (1965).

[132] S. N. Ershov, V. A. Panteleev, S. N. Nagornkh, V. V. Chernyakhovskii, Sov. Phys. Solid State **19**, 11 (1977).

[133] A. Hiraki, J. Phys. Soc. Japan **21**, 34 (1966).

[134] J. Vanhellemont, P. Śpiewak, and K. Sueoka, J. Appl. Phys. **101**, 036103 (2007).

[135] A. Carvalho, R. Jones, C. Janke, J. P. Goss, P. R. Briddon, J. Coutinho, and S. Öberg, Phys. Rev. Lett. **99**, 175502 (2007).

[136] G. Den Ouden, J. Appl. Phys. **39**, 4509 (1968).

[137] P. M. Mooney, F. Poulin, and J. C. Bourgoin, Phys. Rev. B **28**, 3372 (1983).

[138] M. Christian Petersen, A. Nylandsted Larsen, and A. Mesli, Phys. Rev. B **82**, 075203 (2010).

[139] M. Elsayed, N. Yu. Arutyunov, R. Krause-Rehberg, G. A. Oganesyan, and V. V. Kozlovski, Acta Mater. **100**, 1 (2015).

[140] W. L. Brown and W. M. Augustyniak, J. Appl. Phys. **30**, 1300 (1959).

[141] J. Slotte, S. Kilpeläinen, F. Tuomisto, J. Räisänen, and A. N. Larsen, Phys. Rev. B **83**, 235212 (2011).

[142] M. Rose, A.G. Balogh, and H. Hahn, Nucl. Instr. and Meth. B **127/128**, 119 (1997).

[143] Y. Chimi, a. Iwase, N. Ishikawa, M. Kobiyama, T. Inami, and S. Okuda, J. Nucl. Mater. **297**, 355 (2001).

[144] N. Nita, R. Schaeublin, M. Victoria, and R. Z. Valiev, Philos. Mag. **85**, 723 (2005).

[145] H. Wang, R. Araujo, J. G. Swadener, Y. Q. Wang, X. Zhang, E.G. Fu, and T. Cagin, Nucl. Instru. Meth. B **261**, 1162 (2007).

[146] G. S. Was, *Fundamentals of Radiation Materials Science*, Springer, Berlin, 2007.

[147] L. K. Mansur, J. Nucl. Mater. **216**, 97 (1994).

[148] G. A. Kachurin, M. -O. Ruault, A. K. Gutakovsky, O. Kaïtasov, S. G. Yanovskaya, K. S. Zhuravlev, and H. Bernas, Nucl. Instru. Meth. B **147**, 356 (1999).

[149] M. C. Ridgway, G. D. Azevedo, R. G. Elliman, C. J. Glover, D. J. Llewellyn, R. Miller, W. Wesch, G. J. Foran, J. Hansen, and A. Nylandsted-Larsen, Phys. Rev. B - Condens. Matter Mater. Phys. 71, 1 (2005).

[150] W. Jiang, H. Wang, I. Kim, I. -T. Bae, G. Li, P. Nachimuthu, Z. Zhu, Y. Zhang, and W. Weber, Phys. Rev. B **80**, 161301 (2009).

[151] S. Charnvanichborikarn, M. T. Myers, L. Shao, and S. O. Kucheyev, Scr. Mater. **67**, 205 (2012).

[152] R. Bullough and R. C. Newman, Reports Prog. Phys. 33, 101 (1970).

[153] X. M. Bai, A. F. Voter, R. G. Hoagland, M. Nastasi, and B. P. Uberuaga, Science **327**, 1631 (2010).

[154] X. M. Bai, L. J. Vernon, R. G. Hoagland, A. F. Voter, M. Nastasi, and B. P. Uberuaga, Phys. Rev. B **85**, 214103 (2012).

[155] I. J. Beyerlein, A. Caro, M. J. Demkowicz, N. A. Mara, A. Misra, and B. P. Uberuaga, Mater. Today **16**, 443 (2013).

[156] J. B. Wallace, L. B. Bayu Aji, L. Shao, and S. O. Kucheyev, Unreleased LLNL manuscript, LLNL-JRNL-694340-DRAFT.

[157] J. S. Williams, K. T. Short, R. G. Elliman, M. C. Ridgway, and R. Goldberg, Nucl. Instru. Meth. B **48**, 431 (1990).

[158] L. A. Christel, J. F. Gibbons, and T. W. Sigmon, J. Appl. Phys. **52**, 7143 (1981).

[159] K. S. Jones, S. Prussin, and E. R. Weber, Appl. Phys. A Solids Surfaces **45**, 1 (1988).